

AD-751 989

AN EXPERIMENTAL AND CALCULATIONAL STUDY
OF DECOUPLING BEHAVIOR

C. Young, et al

Physics International Company

Prepared for:

Defense Nuclear Agency
Advanced Research Projects Agency

September 1972

DISTRIBUTED BY:

NTIS

National Technical Information Service
U. S. DEPARTMENT OF COMMERCE
5285 Port Royal Road, Springfield Va. 22151

AD751989

DNA-2819F
SEPTEMBER 1972

PIFR-240/241

AN EXPERIMENTAL AND CALCULATIONAL
STUDY OF DECOUPLING BEHAVIOR

FINAL REPORT

by
C. Young and J. D. Watson

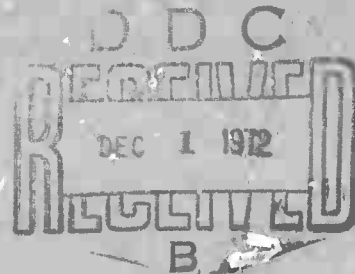
Prepared for
Headquarters
Defense Nuclear Agency
Washington, D.C. 20305

Reproduced by
NATIONAL TECHNICAL
INFORMATION SERVICE
U S Department of Commerce
Springfield VA 22151

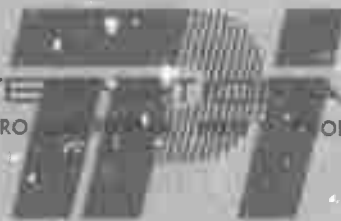
Under Contract
DASA 01-70-C-0094

DISTRIBUTION STATEMENT A

Approved for public release;
Distribution Unlimited



PHYSICS INTERNATIONAL COMPANY
2700 MERCED STREET • SAN LEANDRO ONE 357-4610 (415) • TWX 891-9689 (415)



ACCESSION for	
NTIS	White Section <input checked="" type="checkbox"/>
OPC	Buff Section <input type="checkbox"/>
UNANNOUNCED	<input type="checkbox"/>
JUSTIFICATION.....	
BY	
DISTRIBUTION/AVAILABILITY CODES	
WHOL	AS ACQ. ADV/CF SPECIAL
A	

Approved for public release;
distribution unlimited

Destroy this report when no longer needed;
do not return to sender.

DOCUMENT CONTROL DATA - R&D

(Security classification of title, body of abstract and indexing annotation must be entered when the overall report is classified)

1 ORIGINATING ACTIVITY (Corporate author) Physics International Company 2700 Merced Street San Leandro, California 94577		2a REPORT SECURITY CLASSIFICATION Unclassified	
		2b GROUP N/A	
3 REPORT TITLE An Experimental and Calculational Study of Decoupling Behavior			
4 DESCRIPTIVE NOTES (Type of report and inclusive dates) Final Report, September 1972			
5 AUTHOR(S) (Last name, first name, initial) Young, C. and Watson, J. D.			
6 REPORT DATE	7a. TOTAL NO. OF PAGES 163	7b. NO. OF REFS 18	
8a CONTRACT OR GRANT NO. Contract DASA 01-70-C-0094	9a ORIGINATOR'S REPORT NUMBER(S) PIFR-240/241		
b. PROJECT NO. c. ARPA Order: 1188	9b. OTHER REPORT NO(S) (Any other numbers that may be assigned this report) DNA 2918F		
10 AVAILABILITY/LIMITATION NOTICES Approved for public release; distribution unlimited			
11 SUPPLEMENTARY NOTES Details of illustrations in this document may be better studied on microfiche.		12. SPONSORING MILITARY ACTIVITY Director Advanced Research Projects Agency 1400 Wilson Boulevard Arlington, Virginia 22209	
13 ABSTRACT This report presents the results of a calculational and small scale experimental program to study decoupling phenomena. The small scale experiments have the option of testing various chemical explosive sources and earth media, with the effects of overburden. The results reported herein are for spherical detonations of methane-oxygen in both naturally and artificially pressed salt. Nine experiments, all with overburdens corresponding to a depth of 2,600 feet are described and the resulting strain gage data are subjected to a response spectra analysis. The results of the small scale study are in general agreement with large cavity decoupling theory. The calculational technique described in this report is based upon traditional finite difference codes for the close-in decoupling behavior and couples this to an extensive linear elastic region for computing the intermediate range response of the earth media. This method offers inexpensive decoupling calculations with both high frequency resolution for close-in phenomena controlling decoupling and seismologically significant calculational times. The results of several one dimensional calculations in the STERLING/MIRACLE PLAY cavity geometry, with various explosive sources, yield models, equation-of-state models and overburden are presented. Partial results of a two dimensional pill box cavity calculation are also discussed. A -1a (continued)			

ABSTRACT (continued)

response and Fourier spectral analyses of all calculations are given. The effect of yield model, equation-of-state model (especially compaction) and overburden are found to be critically important for controlling seismological response.

KEY WORDS

[illegible]

-1C-

DNA-2819F
SEPTEMBER 1972

PIFR-240/241

AN EXPERIMENTAL AND CALCULATIONAL
STUDY OF DECOUPLING BEHAVIOR

FINAL REPORT

This work was supported by the
Advanced Research Projects Agency under ARPA Order No. 1188

by

C. Young and J. D. Watson

Prepared for
Headquarters
Defense Nuclear Agency
Washington, D.C. 20305

Under Contract
DASA 01-70-C-0094

- ii -

Physics International Company
2700 Merced Street
San Leandro, California 94577

ACKNOWLEDGEMENTS

The authors would like to express their sincere thanks to the Tracy Test Site Crew and Mr. Fran Allen, for assisting in the experimental program and to Mr. Kerry Seifert, for reducing and analyzing the experimental data. We would also like to thank Miss Mary Fowler and Miss Francis Foster for their suggestions and assistance in carrying out the calculations. Special thanks are accorded to Mr. Stephen Hancock for managing the spectral analysis of both the experimental and calculational programs and for conceiving and programming the LEEK code.

CONTENTS

	<u>Page</u>
SECTION 1 INTRODUCTION	1
SECTION 2 BACKGROUND	5
SECTION 3 SMALL SCALE EXPERIMENTS	11
3.1 Experimental Technique	11
3.2 Results	27
3.3 Data Analysis	51
3.4 Summary	69
SECTION 4 CALCULATIONS	73
4.1 Computational Technique	73
4.2 Results	85
4.3 Data Analysis	111
4.4 Partial Results of the 2-D Calculation	127
4.5 Summary	130
SECTION 5 CONCLUSIONS	139
REFERENCES	143
APPENDIX A - THE LEEK CODE	145
APPENDIX B - DESCRIPTION OF THE VARIOUS MATERIAL MODELS	153

ILLUSTRATIONS

<u>Figure</u>		<u>Page</u>
1	Cross Section of Spherical Pressure Chamber Containing Test Sample with a 2-Inch-Diameter Cavity for Decoupling Detonations	14
2	Open Pressure Chamber Showing an Encapsulated Salt Block in Position in Lower Hemisphere Prior to Placement of Upper Hemisphere to Close Chamber	17
3	Closed and Bolted Pressure Chamber Ready for Pressurization by High-Pressure Nitrogen and Execution of a Small-Scale Experiment	18
4	Geometry for Measurement of Radial Displacements with Tangential Strain Gages	21
5	PETN - Bridgewire Detonator used to Initiate Detonator in a 2-Inch-Diameter Cavity Filled with Methane and Oxygen	23
6	Typical Oscilloscope Record of Strain-Gage Response Showing Difference Between Low-Frequency and High-Frequency Amplifier Output	26
7	Reduced Displacement Versus Time Profiles Obtained from Two Strain Gages in Small-Scale Experiments Nos. 240-1 and 240-2	32
8	Central Parting Plane and the Scaled Decoupling Cavity Following Shot 240-1	34
9	Reduced Displacement Versus Time Profiles for Strain Gages 1 and 2 as Monitored by a Low-Frequency Amplifier in Shots 240-3c, 240-4, and 240-5	38

Preceding page blank

ILLUSTRATIONS (cont.)

<u>Figure</u>		<u>Page</u>
10	Reduced Displacement Versus Time Profiles for Strain Gages 2 and 3 as Monitored by High Frequency Amplifiers in Shots 240-3c, 240-4, and 240-5	39
11	Schematic of Salt Block used for Shots 240-1 and 240-2, Showing the Location of Strain Gages around Cavity	41
12	Schematic of Salt Block used for Shots 240-3c, 240-4, and 240-5, Showing Location of Strain Gages	42
13	Schematic of Salt Block used for Shots 240-6 through 240-9, Showing Location of Strain gages with Respect to Tapered Aluminum Plug	45
14	Reduced Displacement Versus Time Profiles Obtained by Strain Gages in Shots 240-6 and 240-9	47
15	Reduced Displacement Versus Time Profiles Obtained by Strain Gages at Three Radii in Shots 240-7 and 240-8	49
16	Displacement Response Spectra Obtained from Records of Strain Gage 2L for Shots 240-3c, 240-4, and 240-5	58
17	Displacement Response Spectra Obtained from Records of Strain Gage 2H for Shots 240-3c, 240-4, and 240-5	59
18	Displacement Response Spectra Obtained from Records of Strain Gage 1H for Shots 240-6, 240-7, and 240-8	60
19	Displacement Response Spectra Obtained from Records of Strain Gage 2L for Shots 240-6, 240-7, and 240-8	61
20	Displacement Response Spectra Obtained from Records of Strain Gage 2H for Shots 240-6 to 240-9	62
21	Displacement Response Spectra Obtained from Large-Scale Calculations Involving Various Energy Sources and Rock Yield Models	63

ILLUSTRATIONS (cont.)

<u>Figure</u>		<u>Page</u>
22	Comparison of Experimental and Computational Results for 180 bar Overburden, Approximately 360 bar Cavity Equilibrium Pressure at 4 Cavity Radii	67
23	Computational Procedure for the One-Dimensional POD Problems	77
24	Cavity Wall Pressure History for Cavity Equilibrium Pressure of 180 bars	86
25	Cavity Wall Pressure History for Cavity Equilibrium Pressure of 360 bars	87
26	Cavity Wall Pressure History for Cavity Equilibrium Pressure of 720 bars	88
27	Selected Pressure Profiles for Gas Source Calculations	89
28	Selected Pressure Profiles for the Gas Source Calculations	90
29	Cavity Wall Pressure History for Cavity Equilibrium Pressure of 360 bars	91
30	Selected Pressure Profiles for the Nuclear Source Calculation	92
31	Cavity Wall Pressure History for Cavity Equilibrium Pressure of 360 bars	93
32	Typical Calculated Stress Histories in the Salt from a Gaseous Detonation in a Spherical Cavity	95
33	Typical Radial Stress Histories Showing the Effects of Overburden and Compaction	96
34	Typical Radial Stress Histories for Gas and Nuclear Sources	97
35	Velocity Histories Showing the Effect of Compaction	98
36	Velocity Histories Showing the Effect of Compaction	99
37	Velocity Histories Showing the Effect of Overburden and Yield Model	100

ILLUSTRATIONS (cont.)

<u>Figure</u>		<u>Page</u>
38	Peak Particle Velocity as a Function of Radius Showing the Effect of Compaction and Overburden	101
39	Peak Particle Velocity as a Function of Radius Showing the Effect of Yield Model and Overburden	102
40	Peak Particle Velocity as a Function of Radius Showing the Effect of Cavity Equilibrium Pressure	103
41	Peak Particle Velocity as a Function of Radius for Nuclear and Gas Explosions	104
42	Displacement Histories Showing the Effect of Yield Model and Overburden	105
43	Displacement Histories Showing the Effects of Compaction	106
44	Displacement Histories for Gas and Nuclear Source	107
45	Mass-Spring System used to Determine the Fourier and Response Spectra	112
46	Structure of the Displacement Response Spectra	113
47	Response Spectra for the First Five and One-Half Pulses Calculated for an Equilibrium Cavity Pressure of 360 bars, Overburden of 180 bars, Mohr-Coulomb Yield at 4 Cavity Radii	115
48	Displacement Response Spectra Showing the Effect of Source Frequency	116
49	Displacement Response Spectra Showing the Effect of Distance from the Source	117
50	Displacement Response Spectra Showing the Effect of Overburden	118
51	Displacement Response Spectra Showing the Effects of Overburden and Yield Model	120
52	Displacement Response Spectra Showing the Effects of Compaction and Yield Model	121

ILLUSTRATIONS (cont.)

<u>Figure</u>		<u>Page</u>
53	Displacement Response Spectra Showing the Effects of Equilibrium Cavity Pressure and Overburden	123
54	Peak Displacement ($\omega = 0$) as a Function of Radius for Selected Runs	124
55	Displacement Response Spectra Showing the Effect of Zoning and the Current Stability Condition Safety Factor	125
56	Comparison of Response and Fourier Spectra for Linear Media with Yielding and Gas Source	126
57	Comparison of Response and Fourier Spectra for Compactible Media with Yielding and Gas Source	128
58	Lagrange Grid at $t = 7500 \mu\text{sec}$	129
59	Velocity Vector Plot of the Lagrange Grid at $t = 7500 \mu\text{sec}$	131
60	Velocity (\dot{X}) History Parallel to the Axis of Symmetry of the Cavity at $X = 2412 \text{ cm}$ and $Y = 0 \text{ cm}$	132
61	Velocity (\dot{Y}) History Perpendicular to the Axis of Symmetry of the Cavity at $X = 0 \text{ cm}$ and $Y = 3580 \text{ cm}$	133
62	Stress (τ_{xx}) History Parallel to the Axis of Symmetry of the Cavity at $X = 1998 \text{ cm}$ and $Y = 1839 \text{ cm}$	134
63	Stress (τ_{yy}) History Perpendicular to the Axis of Symmetry of the Cavity at $X = 1998 \text{ cm}$ and $Y = 1839 \text{ cm}$	135
64	Shear Stress ($\tau \times Y$) History at $X = 1998 \text{ cm}$ and $Y = 1839 \text{ cm}$	136
A-1	Zoning for Crater Formation Problem	147

SECTION 1

INTRODUCTION

Since the conception in 1959 of using a large underground cavity to decouple (and thus disguise or conceal) a nuclear test (Reference 1), several experimental and theoretical programs have been directed toward improving and extending this concept. The results of several theoretical studies of large-cavity decoupling phenomena (Reference 2) and the data obtained from both large and small field experiments (References 3 and 4) have all served to confirm the validity of the initial decoupling theory. The results of some small-scale laboratory experiments conducted on cavities in plaster of paris (Reference 5) indicate however that the theory of large-cavity decoupling may not be entirely valid.

Although the basic theory for large-cavity decoupling is now well established, there are several aspects of the problem that still need clarification. In particular, the full effects of overburden pressure, non-linear material properties, and cavity shape upon decoupling phenomena are not now well known. Before a complete evaluation of the potential applications and limitations of large-cavity decoupling may be made, the effects of these parameters must be better understood.

Since June of 1968, Physics International Company has been conducting both computational and experimental studies of decoupling phenomena. These efforts at Physics International,

supported by the Advanced Research Projects Agency through the Defense Atomic Support Agency, were initially directed toward using finite-difference calculations to model various shots within the COWBOY series, the SALMON and STERLING nuclear events, and various tests to be conducted in the MIRACLE PLAY series. In support of these calculational efforts, a study of the feasibility of conducting small-scale experiments was initiated in 1969. The results and conclusions of these calculations and initial experimental studies are discussed in detail in Reference 6.

Beginning in March of 1970, Physics International undertook a program for the Advanced Research Projects Agency (under Contract No. DASA-01-70-C-0094) to conduct several small-scale experiments and to perform further calculations in support of the MIRACLE PLAY series and in decoupling concepts in general.

This report discusses the results of the small-scale experiments carried out on this program. Despite several initial experimental difficulties, a reliable and reproducible means of conducting small-scale experiments was developed. Nine small-scale tests were successfully conducted using a variety of salt types, initial detonable gas mixtures (CH_4 and O_2), and equilibrium cavity pressures after detonation. All nine shots were fired with a confining pressure of 2,500 psi to simulate overburden effects. Dynamic strain gages, used to measure radial displacement as a function of time, gave consistent high-quality data on decoupling behavior. The experimental results confirmed the theory of large diameter cavity decoupling and demonstrated the importance of rock strength independent of overburden pressure.

The calculational technique described in this report is applicable to one and two-dimensional calculations. Fifteen one-dimensional calculations with detonable gas (CH_4 and O_2) and nuclear sources were performed. Yield models, equation of state models, overburden and cavity equilibrium pressures were varied, zoning schemes and stability criteria were examined and response and Fourier spectral analyses were carried out for each case. A two-dimensional calculation with a pill box cavity was partially completed, but was terminated early because of lack of funds. All calculations made use of the LEEK boundary condition which is a linear elastic region coupled to the full elastic-plastic description of the earth media, to extend the calculational grid to large distances from the cavity without loss of resolution. This calculational technique in conjunction with advanced computer facilities provides a very useful and potentially inexpensive method for studying decoupling, earthquake and other ground motion phenomena, at near teleseismic distances (several kilometers) while retaining a detailed description of the source mechanism and the non-linear earth properties near the cavity can affect the character of the teleseismic signals.

Section 2 of this report gives the background of decoupling work pertinent to this investigation. The method results and analysis of the small scale decoupling experiments are presented in Section 3. The method results and analysis of the calculational phase of the program are given in Section 4. Finally, the conclusions of this work are detailed in Section 5.

SECTION 2

BACKGROUND

The theory for large-cavity decoupling as initially presented by Latter, et al., in 1959 (Reference 1), was restricted in its application to purely elastic media and could not be applied to media in which plastic deformation occurred. Except for very low stress level loadings, all earth materials in which a decoupled nuclear test might be conducted will invariably undergo some plastic or brittle deformation of a permanent nature. Consequently, it would not be possible to predict the decoupling factors for cavities in earth media subject to such nonelastic behavior. Some of the effects and implications of brittle and plastic rock deformation were considered by Latter, et al., in 1961 (Reference 7). They concluded that for decoupled shots for a low overburden pressure, such as existed for the shallow COWBOY experiments, tensile radial cracking would be the failure mechanism which would most likely reduce the decoupling effectiveness of the cavity. On the other hand, it was concluded that, in a medium such as salt with overburden pressures resulting from depths of burial on the order of one kilometer, plastic flow would be the failure mechanism reducing decoupling effectiveness. They noted, as might be expected, that plastic yielding occurring during construction of a deep cavity would not affect the decoupling effectiveness of that cavity so long as the loading by an explosion in the cavity was purely elastic. It was also concluded that a material displaying extreme work-hardening

effects, such as salt does under appropriate conditions, would tend to provide better decoupling behavior than a non-work-hardening material. The purely analytic nature of the results presented by these investigators makes it practically impossible to derive the decoupling effectiveness of materials displaying complex yielding or compaction phenomena. Generally, the implications of such phenomena can only be fully evaluated with the use of finite-difference calculations or appropriate experiments.

The first experimental work to study and evaluate the theory of large cavity decoupling was carried out on project COWBOY (Reference 3). The 17 high-explosive test shots conducted in the COWBOY series were designed to yield fully tamped, fully decoupled, and partially decoupled conditions. Decoupling factors in general agreement with those predicted from the theories of Latter, et al. (References 1, 7, and 8) were obtained. As has already been noted, the biggest limitation of these experiments was the shallow depth of burial and the concomitant low overburden pressure to which the cavities were subjected. Because the results were probably influenced by the low tensile strength of salt, these experiments do not provide good information on either the effects of compressive rock strength or varying overburden pressures.

In an effort to obtain data on the decoupling theory where larger overburden pressures would be involved and where loading could be accomplished by a nuclear detonation, the SALMON and STERLING experiments were conducted in the Tatum Salt Dome, Mississippi. The SALMON experiment involved the detonation of a fully tamped 5.3-kiloton nuclear device at a depth of 2,600 feet (Reference 9). The cavity formed by the SALMON event was very closely spherical in shape with a radius of 17 meters (55 feet).

The SALMON cavity was used as the decoupling cavity for the STERLING event, which involved detonation of a 0.380-kiloton nuclear device. The greatest limitation in deriving good decoupling data from the SALMON and STERLING events resulted from scaling down the field measurements of the high-yield SALMON detonation to be representative of the ground motions which would be observed for a fully tamped lower-yield device comparable to that used in the STERLING event.

A third program designed to obtain field data on decoupling phenomena is represented by the MIRACLE PLAY series. The principal objective of the MIRACLE PLAY series was to use a detonable gas as the energy source in the SALMON-STERLING cavity and to fire the shots at differing initial pressures corresponding to differing energy levels. The gas pressure and energy content of the first two shots fired in this series, DIODE TUBE and HUMID WATER, were designed to match the yield of the STERLING device and to provide a fully decoupled loading condition. A third shot in the series, DINAR COIN, was to be fired with some three times the energy content of the first two shots and thus to provide a partially decoupled loading condition. Unfortunately, technical difficulties leading to misfires and loss of data on both the DIODE TUBE and HUMID WATER shots resulted in the cancellation of this series.

In addition to the field experiments discussed above, at least two small-scale experimental programs to study decoupling phenomena have been conducted. One of these involved the detonation of small explosive charges in spherical cavities formed in plaster of paris (Reference 5). Unfortunately, overburden

pressures were not applied in conducting these experiments; consequently, the results are probably dominated by tensile radial cracking and have the same limited application as do the results of the COWBOY series. In addition, the diagnostic technique used in these experiments (electrical capacitance probes) do not provide good time-resolved data on a fundamental property, such as stress or particle velocity, of the generated shock wave.

A second small-scale experimental program has been conducted at Physics International under ARPA support (Contract No. DASA-01-70-C-0094) and has resulted in the successful development of experimental capabilities and techniques to study decoupling phenomena on a small scale. This experimental program involved the successful execution of several small-scale decoupling experiments under conditions of high confining (overburden) pressure.

This report discusses in detail the experimental apparatus, the problems which had to be overcome, the experimental results, and the comparison of these results with calculated results. The calculations described in this report were carried out to evaluate the effects of yield model, equation of state model, overburden, source amplitude and source frequency on decoupling behavior.

In addition to the experimental results reported herein, a series of decoupling calculations was performed using traditional finite difference techniques. A unique aspect of these calculations was the coupling of purely elastic code, LEEK, to the outside of the elastic-plastic Lagrange grid. Because the LEEK code is very efficient, the calculations could be carried out to seismologically significant times while retaining good resolution of

higher frequency phenomena. In these calculations the effects of yield model, equation of state model, overburden, source amplitude and frequency on decoupling behavior were studied. Response spectra analysis of the results illustrates how, in a highly yielding and compactible media, energy in the higher frequency modes is shifted into the lower frequency modes resulting in a net amplification of energy in the seismically important frequencies.

SECTION 3

SMALL SCALE EXPERIMENTS

3.1 EXPERIMENTAL TECHNIQUE

As discussed in the preceding section, there have been few systematic experimental programs to study decoupling phenomena. A reasonably broad experimental study of decoupling behavior incorporating a significant number of variables is probably represented only by the COWBOY series conducted for the AEC in 1960 (Reference 3). Although some excellent data on decoupling behavior were obtained in SALMON and STERLING nuclear tests, the high cost of such nuclear experiments precludes the systematic study of decoupling phenomena.

If a small-scale experimental capability could be developed, tests to evaluate various parameters of interest could be economically conducted in a laboratory environment. Efforts in this program were directed towards refining experimental techniques which were partially developed for ARPA on Contract No. DASA-01-68-C-0147 during the period August, 1968 through September, 1969 (Reference 6). The successful application of small-scale experimental techniques to the study of decoupling phenomena would provide data which could be used to critically evaluate theoretical and calculational predictions at a cost significantly less than that required for large-scale field experiments.

In designing the experimental scale and geometry to be used in carrying out small-scale decoupling experiments, consideration was given both to the types of large scale shots that might be meaningfully modeled and to the cost effectiveness of various experimental designs. At the time this experimental work was initiated, the greatest amount of interest and effort in decoupling was directed towards the MIRACLE PLAY Series being planned for the SALMON/STERLING cavity in the Tatum Salt Dome. Consequently, it was decided to design the small-scale experiments to model the SALMON/STERLING cavity in salt and to use a detonable gas (methane-oxygen) as the explosive energy source. After careful review, it was concluded that a 2-inch-diameter spherical cavity in rock salt would be small enough to be experimentally cost-effective and yet large enough to yield valid results.

In laying out a small-scale experimental study of decoupling phenomena, careful consideration must be given to any scaling factors that might influence the results. If the peak and equilibrium pressures developed by an energy source are not dependent upon the size and the total energy of the source and if the response of the material around the source is time independent, then times and displacements will scale directly as lengths are scaled. Thus a 2-inch diameter spherical cavity would correspond to a scale reduction of 650 from the 108-foot-diameter cavity created in the Tatum Salt Dome by the SALMON experiment, and times and displacements at relative radii should scale by a factor of 650. At any given relative radius, the stresses and particle velocities would be equivalent to those observed in a full-scale experiment.

Although linear scaling laws stipulate that experimental results will not be a function of size, it is still desirable to conduct small-scale experiments on as large a scale as practical. If time dependent effects should perturb experimental scaling, the larger experiments would be the more valid and informative.

One of the most desirable and most difficult parameters to simulate is overburden pressure. The only way in which overburden pressure could be simulated in small-scale decoupling experiments would be by applying an appropriate fluid pressure to the exterior surface of the test block containing the scaled decoupling cavity. Either a liquid or a gas may be used to provide this pressure, but in either case an appropriate pressure vessel to contain the fluid must be designed and the test sample must be properly encapsulated so that the fluid does not penetrate the interstices of the sample and the decoupling cavity within it. Since it is desirable to protect the pressure vessel from large shocks and overpressures that might be generated by detonations within the test decoupling cavity, confining pressures are most logically provided by a highly compressible inert gas rather than a fluid such as kerosene or hydraulic oil. Dry nitrogen, which is commercially available in prepressurized bottles at pressures up to 6,000 psi, was selected as the ideal confining medium.

A pressure vessel that had been designed and built in the portion of this program carried out on Contract No. DASA 01-68-C-0147 was quite adequate for continuing the experimental studies. This pressure vessel, shown schematically in Figure 1, is constructed of two pressed steel hemispheres held together by 30 high-strength bolts through flanges welded to the hemispheres.

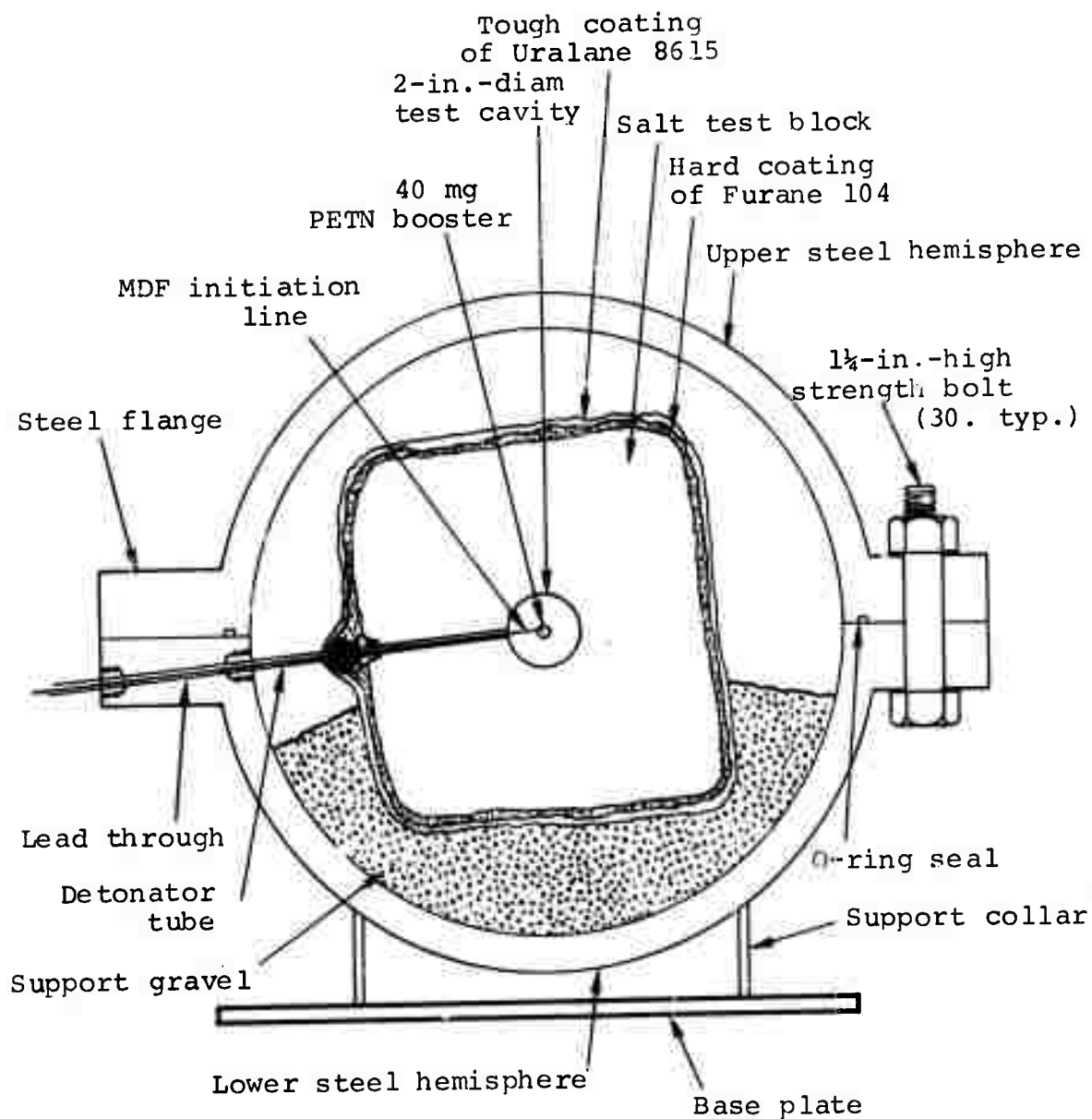


Figure 1 Cross section of spherical pressure chamber
 containing test sample with a 2-inch-diameter
 cavity for decoupling detonations.

The most attractive feature of this design is its large internal volume of spherical geometry with a diameter of 22 inches. This internal geometry would contain a reasonably large equi-dimensional test block, which would provide the optimum in recording times for any instrumentation used in the small-scale decoupling experiments.

An undesirable feature of the pressure vessel is the 30 high-strength bolts used to attach the two hemispheres together. Even when optimum bolt spacing, diameter, and strength are used, this closure method greatly limits the maximum pressures within a chamber of this design. The 3000 psi maximum pressure for which this vessel was designed can be obtained only by allowing for a very small (1.1) safety factor in the failure of the bolts. This pressure vessel could be used at these high pressures only by employing remote operating procedures with the chamber on the firing table at Physics International's Tracy Test Site. In addition, the time to install and torque up the 30 bolts adds considerably to the time required to conduct a small-scale decoupling experiment. A cylindrical pressure vessel with threaded plug closures at each end would be a preferable design for use in any future experiments.

Through a series of trial and error experiments, it was determined that the high pressure nitrogen used to provide confining pressures could be excluded from the interstices of the test sample and from the small scale decoupling cavity by employing concentric layers of two encapsulating materials on the surface of the test block. To provide strength and integrity to the test block, which was composed of several carefully mated pieces of salt, a hard high-strength epoxy, Furane Epibond 104 with 946 hardener, was used for the first encapsulating layer. To ensure

that the high pressure nitrogen could not penetrate through the somewhat brittle Epibond 104 layer, a second layer of Uralane 8615 was applied after the Epibond layer had fully cured. Only a few minor problems with leaks were encountered in utilizing this two-layer encapsulating technique.

A photograph of the lower hemisphere of the high pressure chamber containing a completely encapsulated test block of salt is shown in Figure 2. The tube coming out of the top of the salt block is the detonable gas fill line. The three white wires on the left side of the salt block are coaxial strain gage leads, which connect to the three high-pressure electrical lead-throughs seen passing through the flange of the lower hemisphere on the left hand side. The steel tube seen exiting from the flange of the lower hemisphere closest to the camera is for the emplacement of appropriate detonators into the center of the test decoupling cavity. Details of the detonable gas, strain gage diagnostic, and detonator systems are given below. After the test block has been completely connected for the purposes of conducting a small-scale decoupling experiment, the upper hemisphere is lowered into place and bolted down with the 30 high-strength bolts placed through the holes shown on the upper surface of the flange in Figure 2.

A photograph of the assembled chamber ready for the application of high confining pressure nitrogen and the execution of the small-scale decoupling experiment is shown in Figure 3. The smaller diameter steel tubing seen running between the pressure chamber and the remote valve system is for the high pressure nitrogen, while the larger diameter tubing is for filling the test cavity with a detonable gas mixture. The box on the ground under the pressure tubes contains the strain gage power supplies and amplifiers used in measuring radial displacements during an experiment.



Figure 2 Open pressure chamber showing an encapsulated salt block in position in lower hemisphere prior to placement of upper hemisphere to close chamber.

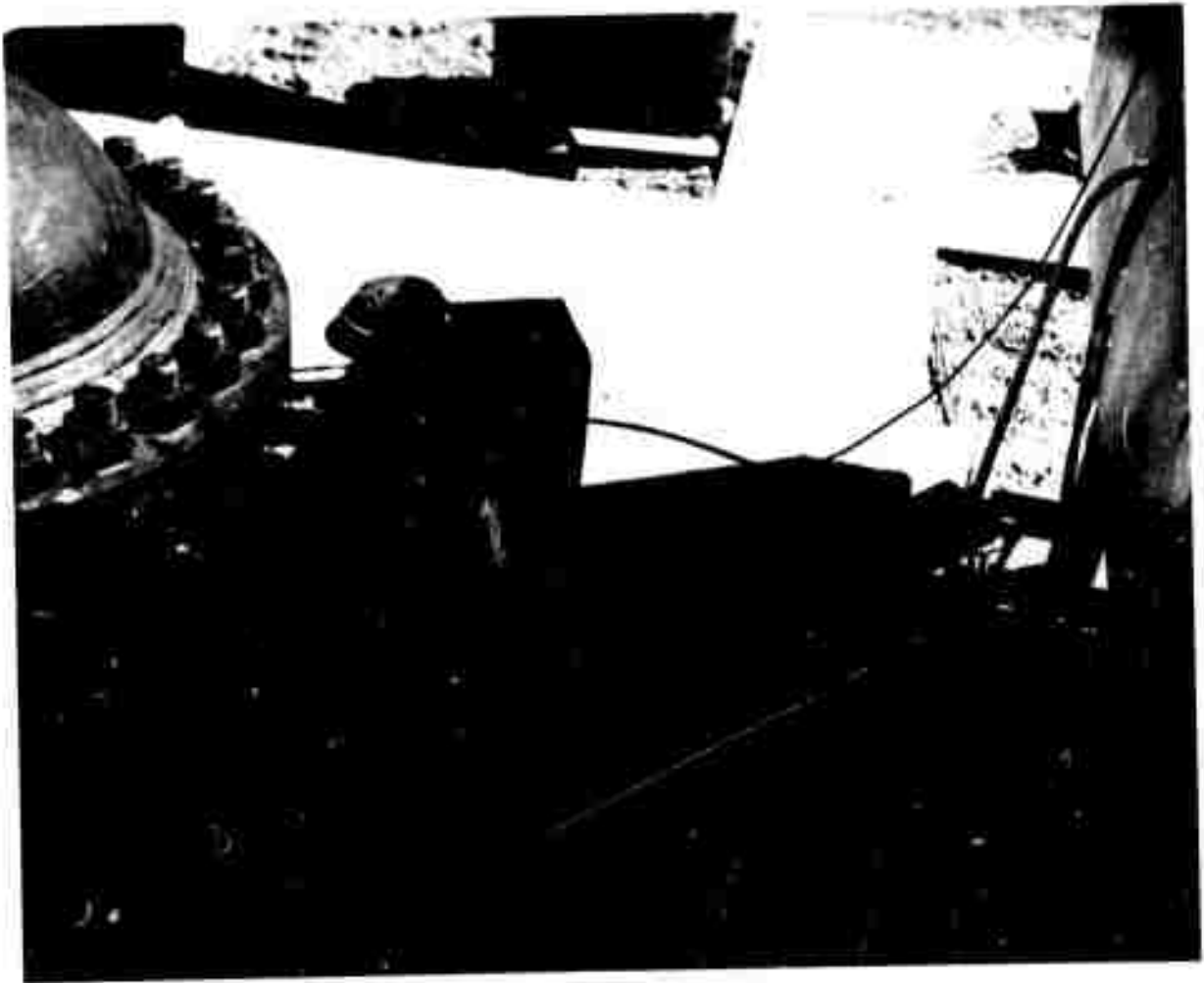


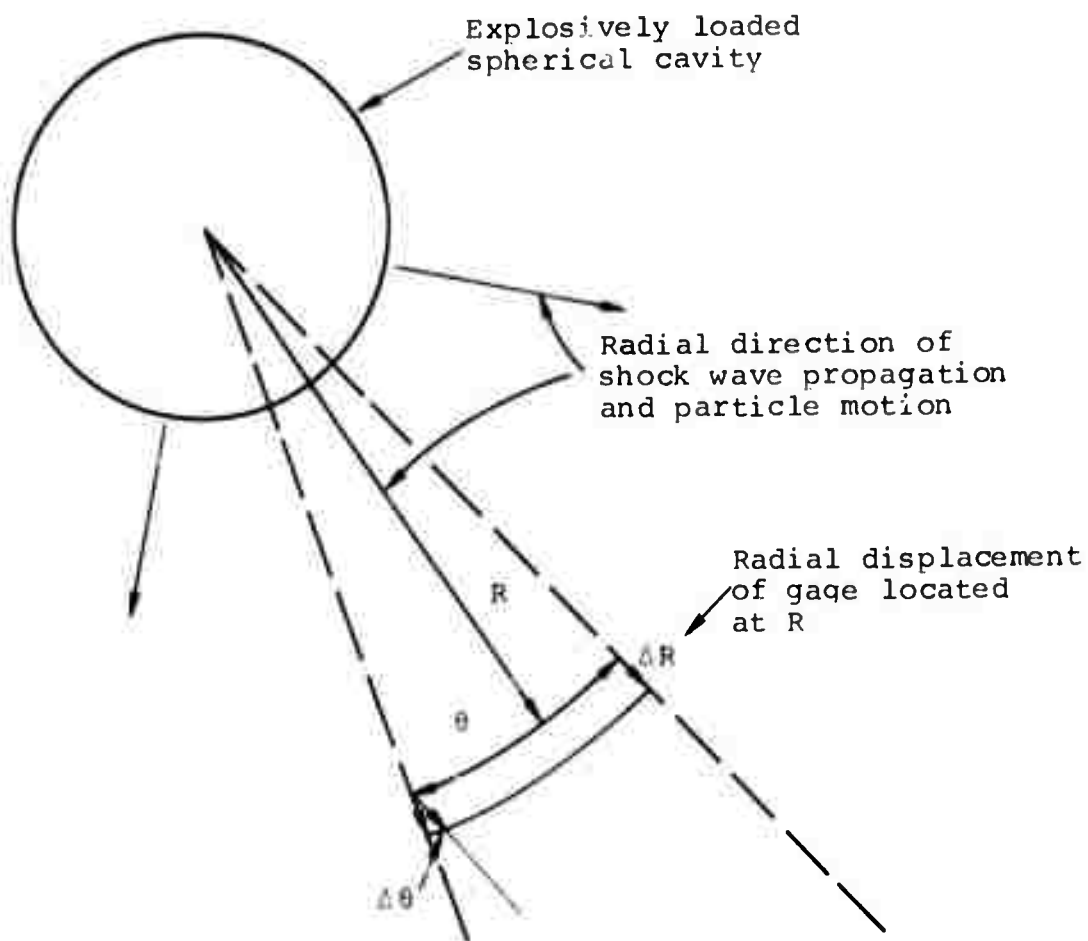
Figure 3 Closed and bolted pressure chamber ready for
pressurization by high-pressure nitrogen and
execution of a small-scale experiment.

The design of small-scale experiments to model the DIODE TUBE, HUMID WATER and DINAR COIN experiments of the MIRACLE PLAY series required that a system for providing a methane-oxygen mix to the scaled decoupling cavity be designed and built. Since this system had to function only at relatively low pressures (less than 1000 psi maximum), the design and fabrication of the detonable gas fill system was relatively simple and straightforward. To ensure that the system could be operated with a high degree of safety, it was necessary to use specially designed explosion-proof valves. to construct a remote fill, bleed and abort system to operate on the firing table at the Tracy Test Site, and to provide valving to ensure that a detonation or deflagration initiated in the test cavity could not propagate back down the lines of the gas-fill system. The remotely operated fill, bleed, and abort valves and an 80,000-psi-rated Autoclave isolation valve to preclude detonations from propagating back into the gas-fill system are contained in the steel box seen partially on the right of Figure 3. With the exception of some leakage past the explosion proof valves at the higher firing pressures, no difficulties were encountered with the detonable gas-fill system.

At the initiation of this research program it was anticipated that the transition from a deflagration to a detonation in the detonable gas would not naturally occur within the 1-inch radius of the scaled cavity. It was initially thought, however, that a detonation could be readily initiated with a high energy spark gap placed at the center of the cavity. The evaluation of this initiation system conducted on Contract DASA 01-68-C-0147 definitely indicated that detonations were not achieved (Reference 6) and that the energy of the detonable gas mix was released through a slowly propagating deflagration. Consequently, efforts

to design a high explosive detonator were begun on Contract DASA-01-68-C-0147. The design and testing of a suitable detonator for these small-scale experiments were continued into the current contract. A detonator that was designed and successfully tested is shown in Figure 4. This detonator, containing approximately 40 mg of PETN pressed around a centrally located bridgewire and encased in a gelatine capsule, is an improved modification of the detonator originally developed on Contract DASA 01-68-C-0147. This newer detonator geometry would assure the generation of a spherically divergent detonation wave, while the original detonator with an asymmetrically located bridgewire would not. The 2.32×10^9 ergs energy contained in 40 mg of PETN is less than 4 percent of the energy of 1.06 gm of a detonable methane/oxygen mix at 220 psi in a 2-inch-diameter cavity.

Although the PETN bridgewire detonators were found to provide very reliable detonations in methane-oxygen gas mixtures ranging in pressure from 110 to 660 psi, it was found that they could not be used inside the large spherical pressure vessel. The electrical noise from this detonator had been tolerable in all tests conducted outside the pressure vessel, but very severe noise problems were encountered when the detonator was fired within the vessel. Large amplitude electrical transients associated with the capacitor discharge system used to fire the detonator lasted for periods of over 100 μ sec when the detonator was fired inside the pressure vessel. Since the shock wave generated by the detonated gas will arrive at the various gage locations in the salt block, some 20 μ sec after the detonator is fired the electrical noise would completely override any gage signal. This problem was readily resolved by placing the bridgewire portion of the detonation system outside the pressure vessel



$$\frac{\Delta R}{R} = \frac{\Delta \theta}{\theta} = \epsilon_t = \text{Strain measured by a tangential strain gage.}$$

Figure 4 Geometry for measurement of radial displacements with tangential strain gages.

and using one grain mild detonating fuse (MDF) to carry the detonation into the test cavity inside the salt block. In order to protect the MDF where it passes through the high confining pressure nitrogen and to reduce the mechanical signal imparted to the salt block by the MDF, the MDF was encased in adiprene inside a 1/8-inch o.d. by 1/16-inch i.d. stainless steel tube. A 40-mg PETN capsule identical to the one used with the bridge-wire illustrated in Figure 5 was placed on the end of the MDF at the center of the test cavity.

The MDF-initiated detonators were also found to provide very reliable initiation of detonations in methane-oxygen mixtures with ratios of 1:1.6 and 1:2 at pressures of 110, 220, 330, 440, and 660 psi. This pressure range completely covers the initial gas pressures that would be required for conducting both underdriven and overdriven small-scale decoupling experiments. In utilizing the MDF-initiated detonator in carrying out the small-scale decoupling experiments, the only problems encountered were associated with electrical noise generated, as a result of ground loops created by the inadvertent grounding of the steel tube containing the MDF.

Several diagnostic systems were considered and carefully evaluated for possible use in measuring and evaluating decoupling effectiveness of spherical cavities in salt. Physics International has had considerable experience in piezoresistive and piezoelectric pressure gages, electromagnetic velocity gages, and strain gages in making dynamic measurements of material response. Because they cannot be utilized as an in-material gage, the piezoelectric type gages were not considered. Piezoresistive gages such as manganin and ytterbium can be very effectively used for making pressure measurements at high stress

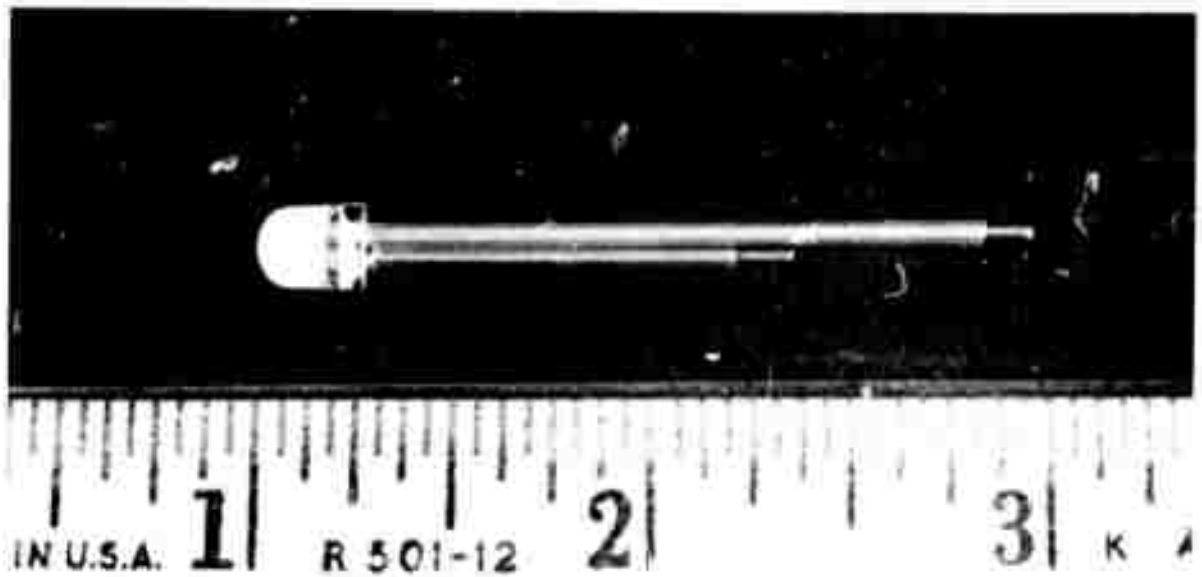


Figure 5 PETN-bridgewire detonator used to initiate detonations in a 2-inch-diameter cavity filled with methane and oxygen.

levels (typically greater than 1 kbar). Because the stress levels anticipated in the small-scale decoupling experiments would, in many cases, be much less than 1 kbar, it was not felt that this type of gage could be satisfactorily used. At the time that a diagnostics system had to be selected for these experiments, Physics International's experience with the electromagnetic velocity gage had not been sufficient to enable us to completely evaluate its potential application to this program. Consequently, dynamic strain gages were selected as the most promising diagnostic system for the experiments.

In conducting the small-scale decoupling experiments, radial displacement versus time histories could be obtained by placing conventional dynamic strain gages on planes in the material to be studied at appropriate radii from the explosive cavity. As illustrated in Figure 4, the planes on which the strain gages are placed are normal to a radial direction from the cavity and the strain gages will in effect measure the tangential or hoop strains at that radius. If a strain gage can make a good measurement of the dynamic hoop strains, then this may be readily reduced to a radial displacement history given the appropriate geometrical considerations. The equation for reducing the tangential or hoop strains, ϵ_t , as measured by a strain gage, to the radial displacement, ΔR , occurring at that radius, R , is:

$$\Delta R = R \times \epsilon_t$$

Inclusion of the strain gage factor, G , and the voltage, V , placed across the gage yields:

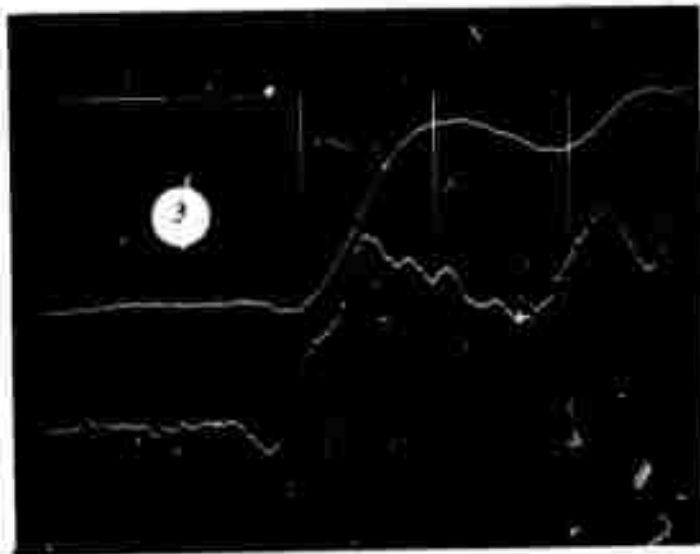
$$\Delta R = \frac{R \times \Delta V}{G \times V}$$

where ΔV is the change in voltage across the gage caused by strain induced changes in resistance. This equation was used to reduce

the strain gage voltage output obtained during an experiment to radial displacements. Note that, as a strain gage is at a greater radial distance from a test cavity, the strain seen by that gage will go down while the corresponding amplification factor, R , will increase. Consequently, strain gages at large relative radii to the cavity would be expected to have unfavorable signal-to-noise ratios.

Strain gage amplifiers with both low and high frequency responses were developed and used to monitor strain gage output on the experiments conducted in this program. An oscilloscope record showing the response of a single strain gage as seen by both a high frequency and a low frequency amplifier is shown in Figure 6. The high frequency amplifier does not seem to be affected by normal levels of electrical noise and does show much more diagnostic wave structure than does the low frequency amplifier. The high frequency amplifier has a maximum frequency response of approximately 3 megacycles while the low frequency amplifier has a maximum frequency response of approximately 100 kilocycles. A simple computer program was developed to reduce the voltage output signal of the strain gage amplifiers, as recorded on an oscilloscope (Figure 6), to the displacement time histories at that strain gage locations.

Since the inception of this experimental program, Physics International has gained considerably more experience with electromagnetic velocity gages (References 10 and 11) and has carefully evaluated the possible applicability of this type of gage to making measurements of small-scale decoupling experiments. Although the strain gage diagnostic system did provide good measurements of radial displacement, it would now be recommended that the electromagnetic velocity gages be used in any future small-scale decoupling experiments.



Upper trace, low
frequency amplitude
.2 volts/division
5 μ sec/division

Lower trace, high
frequency amplitude
.2 volts/division
5 μ sec/division

Shot 240--3C Strain Gauge 2

Figure 6 Typical oscilloscope record of strain-gauge response showing difference between low-frequency and high-frequency amplifier output.

3.2 RESULTS

There are numerous parameters that might be beneficially studied within the scope of an experimental program such as conducted on contract DASA 01-70-C-0094. Such parameters could include size and shape of the decoupling cavity, the explosive energy released in that cavity, the strength and compaction characteristics of the material forming the cavity, and the overburden pressure acting at the time a decoupling test was conducted. Since it was not possible to incorporate all these parameters within the scope of the funded program, it was necessary to decide which parameters could be most meaningfully investigated. Since the small-scale experiments were primarily designed to model shots of the MIRACLE PLAY series, it was felt that the initial experiments should be directed towards studying the effects of increasing the explosive energy in a fixed-size spherical cavity in rock salt. Once the decoupling effectiveness of the spherical cavities modeling the MIRACLE PLAY series had been established, it would then be most desirable to study the possible effects of variations in material properties. Because work hardening of the salt around the SALMON/STERLING cavity in the Tatum salt dome could affect the results of a decoupling experiment, it was felt that a highly work-hardened salt might be a very desirable medium in which to conduct subsequent shots.

Nine small-scale decoupling experiments were successfully conducted on the program during the period September 28, 1970 to December 22, 1970. All of these experiments were carried out

using a detonable methane-oxygen gas mixture in a 2-inch-diameter spherical cavity in salt. The initial partial pressures of methane and oxygen, their ratio, and the total detonable gas pressure utilized in each of the nine experiments are given in Table 1. The first five experiments were conducted in a coarse-grained natural rock salt from Texas while the last four experiments were carried out in a cavity formed in an artificially pressed salt. All of the experiments were conducted with a confining pressure of 2500 psi designed to simulate the 2720-foot depth of the SALMON/STERLING cavity.

Except for the first and last experiments, excellent strain-gage records were obtained for all strain gages (2 or 3) and all amplifiers (3 or 4) used in each experiment. In both the first and last experiments, very high level electrical noise, probably caused by current ground loops formed when the steel tube, containing the MDF used to fire the PETN capsule inside the cavity, was inadvertently grounded to the steel pressure chamber. When this grounding occurred, current from the capacitor discharge unit used to fire the shot could travel down the steel tube, through the steel pressure vessel and back to ground through the steel tubes of the detonable and high-pressure-gas systems.

Basic information obtained from the strain gage diagnostic system used in the nine experiments conducted on this program is summarized in Table 2. In this table the numerical portion (1, 2 or 3) of the strain gage designation refers to an actual strain gage while the letter portion (L or H) of the designation pertains to the type of amplifier used to monitor that strain

TABLE 1
SUMMARY OF EXPERIMENTAL CONDITIONS FOR SMALL-SCALE
DECOUPLING EXPERIMENTS

<u>Shot</u>	<u>Material</u>	<u>Firing Pressure</u> (psi) (bars)		<u>Gas Mixture</u>		<u>Ratio</u>	<u>Confining Pressure</u> (psi)
				<u>O₂</u> (psi)	<u>CH₄</u> (psi)		
240-1	Natural Rock Salt	220	15.2	135	85	1:1.6	2500
240-2	"	440	30.3	270	170	1:1.6	2500
240-3C	"	220	15.2	135	85	1:1.6	2500
240-4	"	440	30.3	270	170	1:1.6	2500
240-5	"	660	45.4	405	255	1:1.6	2500
240-6	Artificially Pressed Salt	220	15.2	135	85	1:1.6	2500
240-7	"	220	15.2	147	73	1:2.0	2500
240-8	"	440	30.3	293	147	1:2.0	2500
240-9	"	440	30.3	270	170	1:1.6	2500

TABLE 2
SUMMARY OF STRAIN GAGE RESULTS
FOR SMALL-SCALE DECOUPLING EXPERIMENTS

Shot	Strain Gage	Radius (inch)	Peak Displacement (cm)	Arrival Time From Zero Time (μ sec)	Peak Arrival Time (μ sec)	
					From Arrival Time	From Zero Time
240-1	1L	2.960	0.60×10^{-4}	104	3.2	107.2
	2L	2.913	0.71×10^{-4}	104	3.3	107.3
240-2	1L	2.960	2.61×10^{-4}	105	6.2	111.2
	2L	2.913	2.55×10^{-4}	104	3.3	107.3
240-3C	1L	3.05	5.51×10^{-4}	108	18.7	126.7
	2L	3.12	5.49×10^{-4}	111	12.5	123.5
	2H	3.12	7.16×10^{-4}	108	7.6	115.6
	3H	4.60	3.07×10^{-4}	114	5.3	119.3
240-4	1L	3.05	11.76×10^{-4}	116	18.9	134.9
	2L	3.12	14.07×10^{-4}	118	14.4	132.4
	2H	3.12	15.93×10^{-4}	115	8.8	123.8
	3H	4.60	5.31×10^{-4}	124	5.5	129.5
240-5	1L	3.05	16.23×10^{-4}	120	12.0	126.0
	2L	3.12	16.89×10^{-4}	120	14.8	132.9
	2H	3.12	17.98×10^{-4}	119	12.6	131.0
	3H	4.60	5.87×10^{-4}	126	7.0	133.0
240-6	1H	3.008	5.33×10^{-4}	100	8.0	108.0
	2H	4.041	6.24×10^{-4}	107	8.5	115.5
	2L	4.041	3.81×10^{-4}	108	14.5	122.5
	3H	6.075	4.15×10^{-4}	120	8.5	128.5
240-7	1H	3.008	7.36×10^{-4}	105	8.1	113.1
	2H	4.041	7.58×10^{-4}	112	7.7	119.7
	2L	4.041	4.12×10^{-4}	112	12.0	124.0
	3H	6.075	5.75×10^{-4}	129	8.5	137.5
240-8	1H	3.008	14.10×10^{-4}	102	9.2	111.2
	2H	4.041	12.46×10^{-4}	108	8.3	116.3
	2L	4.041	8.00×10^{-4}	109	14.5	123.5
	3H	6.075	9.20×10^{-4}	120	8.6	128.6
240-9	1H	3.008	12.30×10^{-4}	120	8.0	128.0
	2H	4.041	12.83×10^{-4}	128	12.0	140.0
	3H	6.075	9.50×10^{-4}	134	7.0	141.0

gage. The letter "L" indicates that a low-frequency, 100-kHz-peak-response strain gage amplifier was used whereas the letter "H" indicates a high-frequency, 3-MHz strain gage amplifier. Note that in nearly all shots one strain gage was monitored with both a low- and a high-frequency amplifier so that relative response data for these two amplifying systems could be obtained. The time of arrival of the initial shock wave, the peak displacement observed by each strain gage, and the arrival time of that peak displacement are indicated in Table 2 also. A difference in amplitude and arrival times of the peaks for the low- and high-frequency amplifier records of a single strain gage is due to the differences in responses of these amplifiers (see, for example, Figure 6). The arrival time for the initial shock at each strain gage includes time for the detonation of the MDF, detonation of the detonable gas across the cavity, and the propagation of the shock wave from the cavity wall to the referenced strain gage. The differences in arrival times for strain gages at different radii did provide data which could be used to calculate the shock velocity in the salt material being studied.

The first small-scale decoupling experiment (240-1) was conducted on September 28, 1970. A 220-psi mixture of methane and oxygen in a ratio of 1 to 1.6 was used as the detonable gas energy source in this experiment. With the exception of some adverse electrical noise associated with ground loops formed via a shorted MDF tube, every aspect of the system appeared to work quite reliably during the execution of this first test shot. Despite this noise, interpretable records were obtained from both of the strain gages used in this shot. In this experiment only the low-frequency amplifiers were utilized. The reduced displacement time histories recorded by the two strain gages are shown in Figure 7. A sharp increase in displacement shown at the

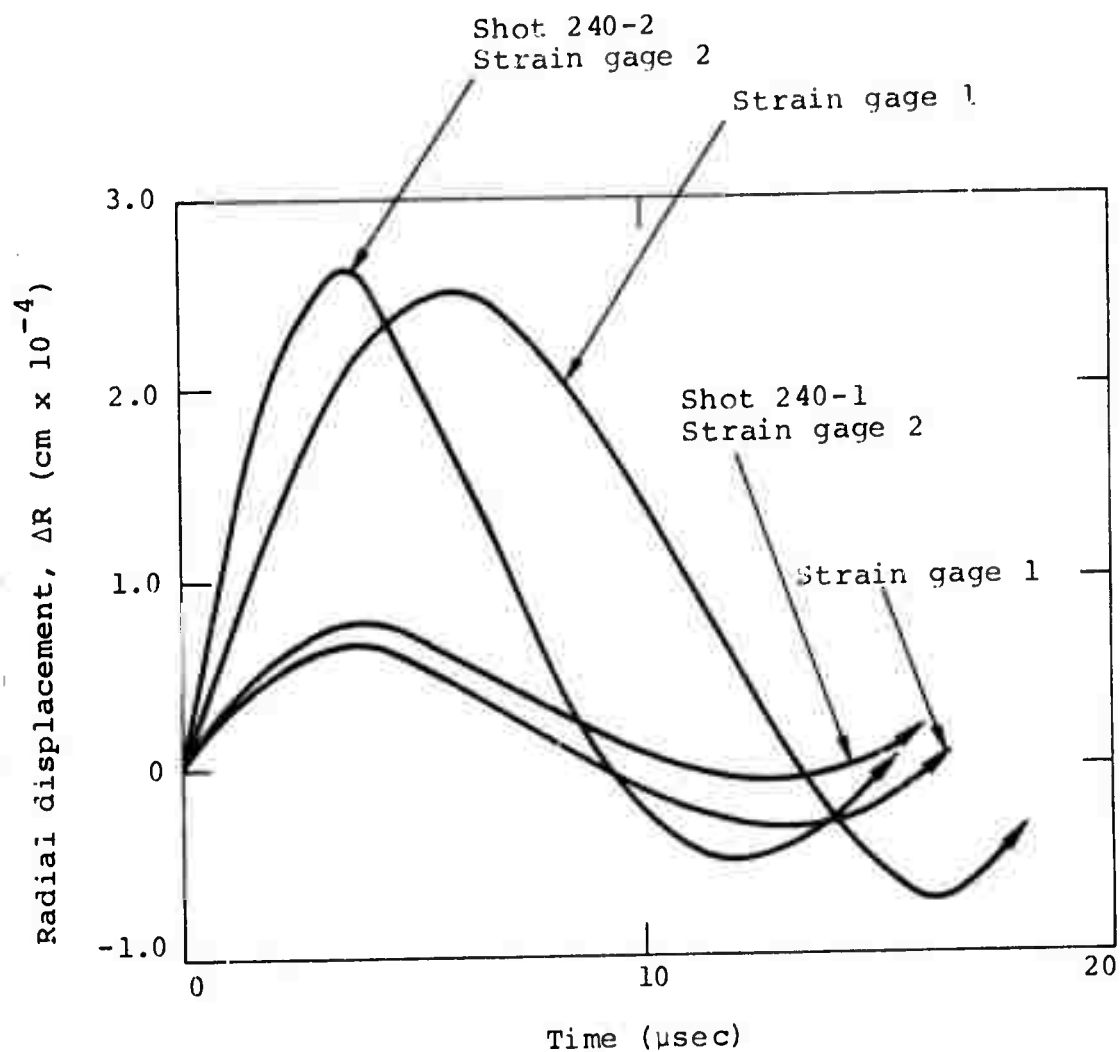
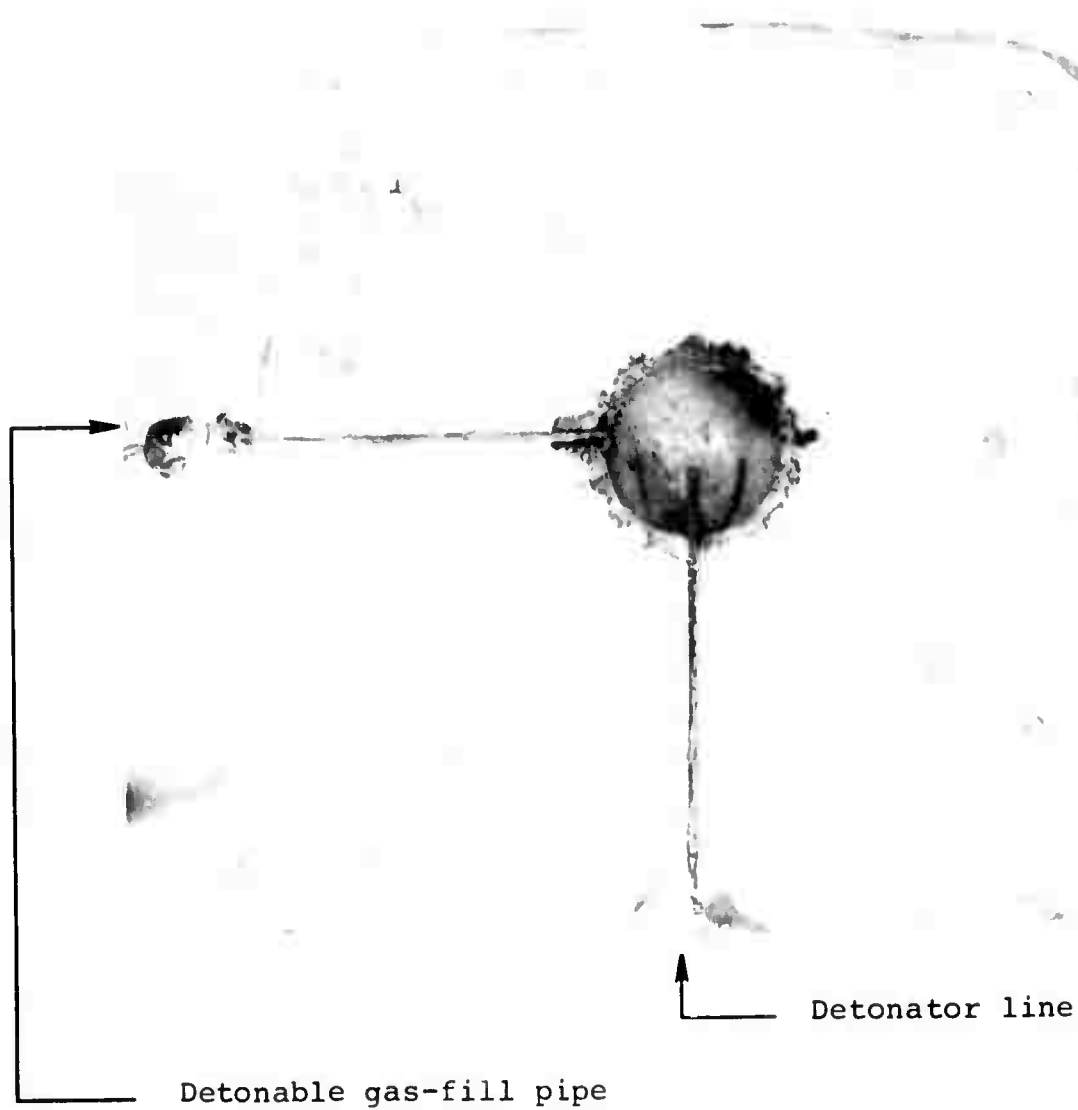


Figure 7 Reduced displacement versus time profiles obtained from two strain gages in small-scale experiments Nos. 240-1 and 240-2.

end of each record is due to the arrival of reflected waves at the gage and marks the end of valid gage recording. The significance of these records will be discussed in more detail below along with a discussion of the records obtained in Shot 240-2, which are also shown in Figure 7.

One of the most rewarding results of Shot 240-1 was the post-shot condition of the shot block cavity and jacketing material. After the shot was fired, the detonable-gas fill line was vented and the pressure in the cavity monitored. There was no evidence of any leakage of the high pressure confining gas through the jacketing materials into the salt cavity, indicating that damage, if any, to the salt block was minor. After the salt block was removed from the high-pressure chamber, it was disassembled along the central parting plane so that the cavity and the gas fill and detonator lines could be inspected. A photograph of the post shot cavity after Shot 240-1 is shown in Figure 8. A lack of damage to the salt immediately adjacent to the cavity and the small extent to which the detonation products escaped along the parting plane both attest to the fact that the cavity was underdriven by the detonation.

The excellent condition of the post-shot salt block and the long time response of the strain gages (including the recording of reflected waves) indicated that the salt block could be re-assembled for a second shot. This reuse of the salt block for sequential shots is especially valuable in terms of gaining high quality data. As discussed above, large grain size of the salt and the strain-gage coupling to the salt can have an effect upon actual strain-gage response. The difference in the response between two strain gages with essentially identical locations in the salt block used for Shot 240-1 indicated that these effects could



Reproduced from
best available copy.

Figure 8 Central parting plane and the scaled decoupling cavity following Shot 240-1.

be fairly serious. If a single strain gage installation could be used for several shots, however, then the effects of large grain size and strain-gage coupling would be eliminated as far as the relative response of that strain gage was concerned. Because it was not necessary to change or modify the strain gages used in Shot 240-1 in refabricating the salt block for Shot 240-2, a very valid comparison of the strain-gage records obtained in the two shots may be made.

The displacement-time histories measured by the two strain-gages in Shot 240-2 are shown in Figure 7 with the records for Shot 240-1.

Shot 240-2 was fired using a 440-psi mixture of CH_4 and O_2 in the ratio of 1 to 1.6. Since this pressure is exactly twice that used for Shot 240-1, this shot had essentially twice the explosive energy of the earlier shot. Displacement profiles from these two shots, as illustrated in Figure 7, indicate that displacements increased by more than a factor of three between the two shots. This effect, of course, is exactly what one would expect in going from a fully decoupled shot to a partially decoupled shot, as was the case for Shot 240-2.

The excellent condition of the salt block after Shots 240-1 and 240-2 lead us to positively conclude that a single salt block could be used quite successfully for several shots. Consequently, we redesigned our experimental arrangement so that, once a salt block was fitted with strain gages and sealed to withstand the high confining pressures, it could be refitted with the necessary detonator without having to be removed from the large hemispherical pressure chamber. The modified configuration involved using a large-diameter (3/8-inch o.d. x 1/4-inch i.d.) steel tube to go from the outside pressure chamber

to inside the salt cavity. The salt blocks used for the second and third series of shots employed this new configuration. The salt block used for the second series of experiments was also manufactured of the same coarse-grained Texas salt dome material as was used for the first two shots. As in the configuration for the first salt block shots, two strain gages were located at approximately three cavity radii from the center of the shot. A third strain gage was located at approximately 4.6 cavity radii from the center of the cavity. Other aspects of the configuration of this salt block will be discussed in greater detail later.

In firing Shots 240-3, 240-4, and 240-5, efforts were made to obtain three distinctly different preshot cavity pressures. It was decided that preshot pressures of 220 psi, 440 psi, and 660 psi would yield the most valuable data. Excellent strain-gage records were obtained from all three strain gages for all three of these shots. Difficulties with electrical noise required that Shot 240-3 (at 220 psi) be refired several times, until good records were obtained.

The first successful data shot at this pressure has been designated as 240-3C. A second shot in this series, 240-4, was successfully fired without any difficulties at 440 psi. Some difficulty was encountered with the detonatable-gas, mixed pressurization system in attempting to fire the third shot in the series (Shot 240-5). A serious leak developed in the pressurization system at this higher pressure. We had difficulty maintaining the 660-psi pressure and could not be sure that the gas mix was exactly 1.6 O_2 to 1.0 CH_4 . All of the shots in this series were fired with methane-oxygen in the ratio of 1 to 1.6, and all the shots had an overburden pressure of 2500 psi.

Strain-gage amplifiers with both low-frequency and high-frequency response were used in this shot. Strain gage 1 was at a radius relative to the cavity of 3.05 and was monitored with a low-frequency amplifier; strain gage 2 at a relative radius of 3.12 was monitored with both low- and high frequency amplifiers; and strain gage 3 at a relative radius of 4.60 cavity radii was monitored with only a high-frequency-response amplifier. The relative response of strain gage 2, as seen by both a low- and high-frequency amplifier in Shot 240-3C, is illustrated in Figure 6.

The displacement-time profiles, as monitored by strain gages 1 and 2 for the three successful data shots in this series, are shown in Figure 9. All six of these profiles were reduced from low-frequency amplifier records. displacement-time profiles obtained from strain gages 2 and 3 using high-frequency strain-gage amplifiers are illustrated in Figure 10. Note that the high-frequency amplifiers generally show the same response as the low-frequency amplifiers but with greater wave detail. As was the case for the first shots fired in this program (240-1 and 240-2), the peak displacement measured by the strain gages increases by a factor greater than two when the explosive energy in the cavity is doubled (by increasing initial gas pressures from 220 psi to 440 psi). The very slight increase in maximum displacement obtained in Shot 240-5 is probably a result of having a poor detonatable gas mix and less than the anticipated 660-psi preshot cavity pressure.

Comparison of the strain-gage records obtained in the first series of shots (240-1 and 240-2, Figure 7) with the strain-gage records obtained in the second series of shots (240-3, 240-4, and 240-5, Figure 9) at an approximate radius of 3 inches from

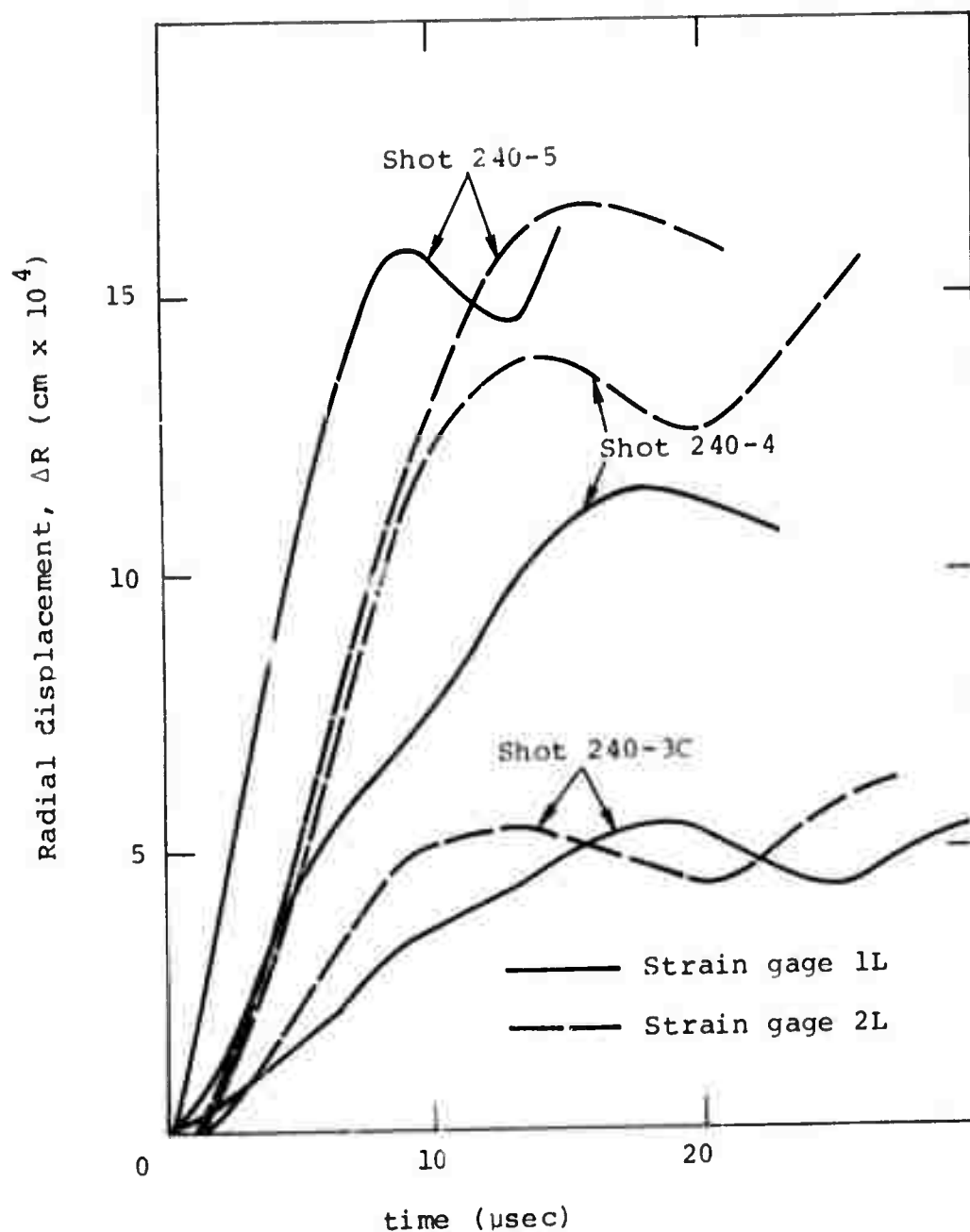


Figure 9 Reduced displacement versus time profiles for strain gages 1 and 2 as monitored by a low frequency amplifier in Shots 240-3c, 240-4, and 240-5.

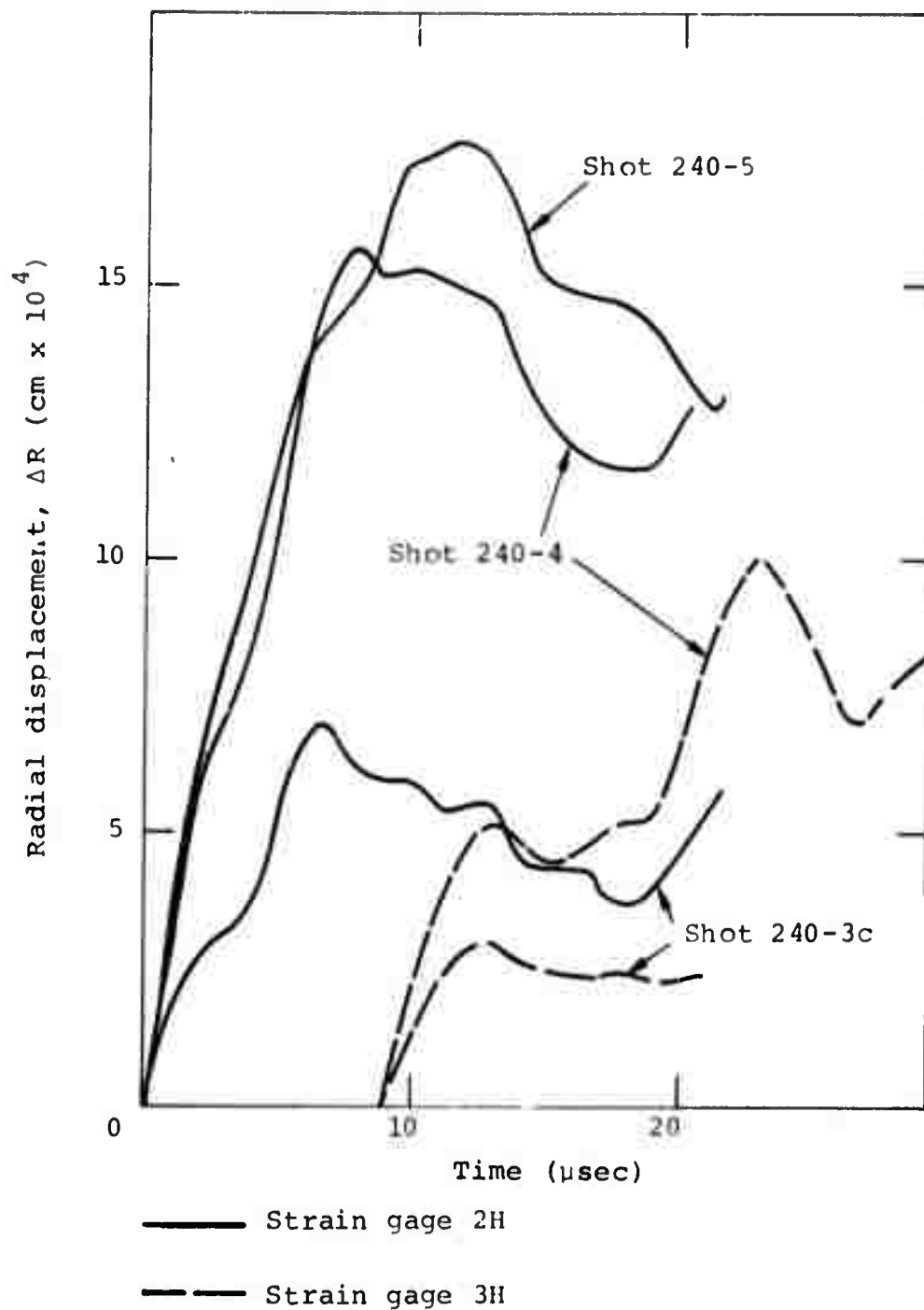


Figure 10 Reduced displacement versus time profiles for strain gages 2 and 3 as monitored by high frequency amplifiers in Shots 240-3c, 240-4, and 240-5.

the center of the cavity indicates some possibly large discrepancies between the data obtained in the two series. The displacement-time histories obtained in the first series of shots are both lower in amplitude and much narrower in time than in the second series of shots. These discrepancies can be most readily attributed to the way in which the salt blocks were fabricated for each of the series. The geometry of the salt block configuration used in the first series is illustrated in Figure 11. In this block the parting plane used to provide access to the cavity and the necessary gas-filling and detonating equipment was uncemented when the salt block was finally assembled. In addition, the planes on which the strain gage was located were oriented at 45 degrees to this uncemented parting plane. If the pressure of the detonated gas in the cavity were high enough to create tensile hoop stresses around the cavity, the uncemented parting plane would separate with a simultaneous injection of high-pressure detonated-gas products into the parting plane. As may be seen in Figure 11, the signal generated by the injection of hot gases along the parting plane would arrive at the strain-gage location very soon after the signal traveling along the shortest radial direction. Since the anomalous signal originating at the uncemented parting plane would destroy the spherical geometry of an outgoing shock wave, it could cause both the low amplitude and narrow time width of the strain gage profiles obtained in the first series of shots.

In contrast, the salt block assembled for the second series of shots had a geometry less amenable to such anomalous effects. The overall geometry of the salt block for this series is shown in Figure 12. Because the large-diameter detonator pipe allowed for the replacement of the detonator at the center of the cavity without disassembling the salt block, we were able to permanently cement the central parting plane with a high-strength epoxy.

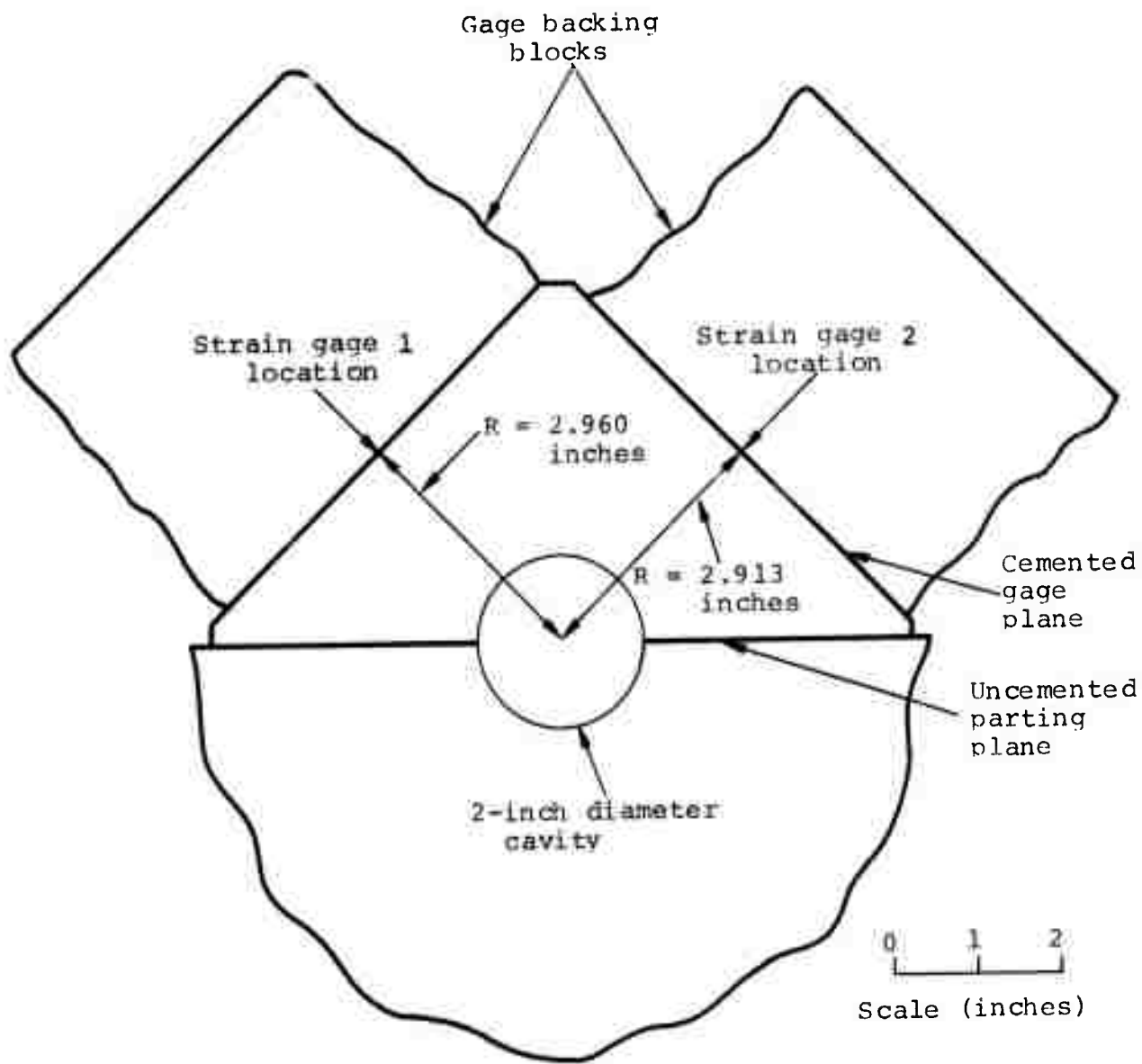


Figure 11 Schematic of salt block used for Shots 240-1 and 240-2, showing the location of strain gages around cavity.

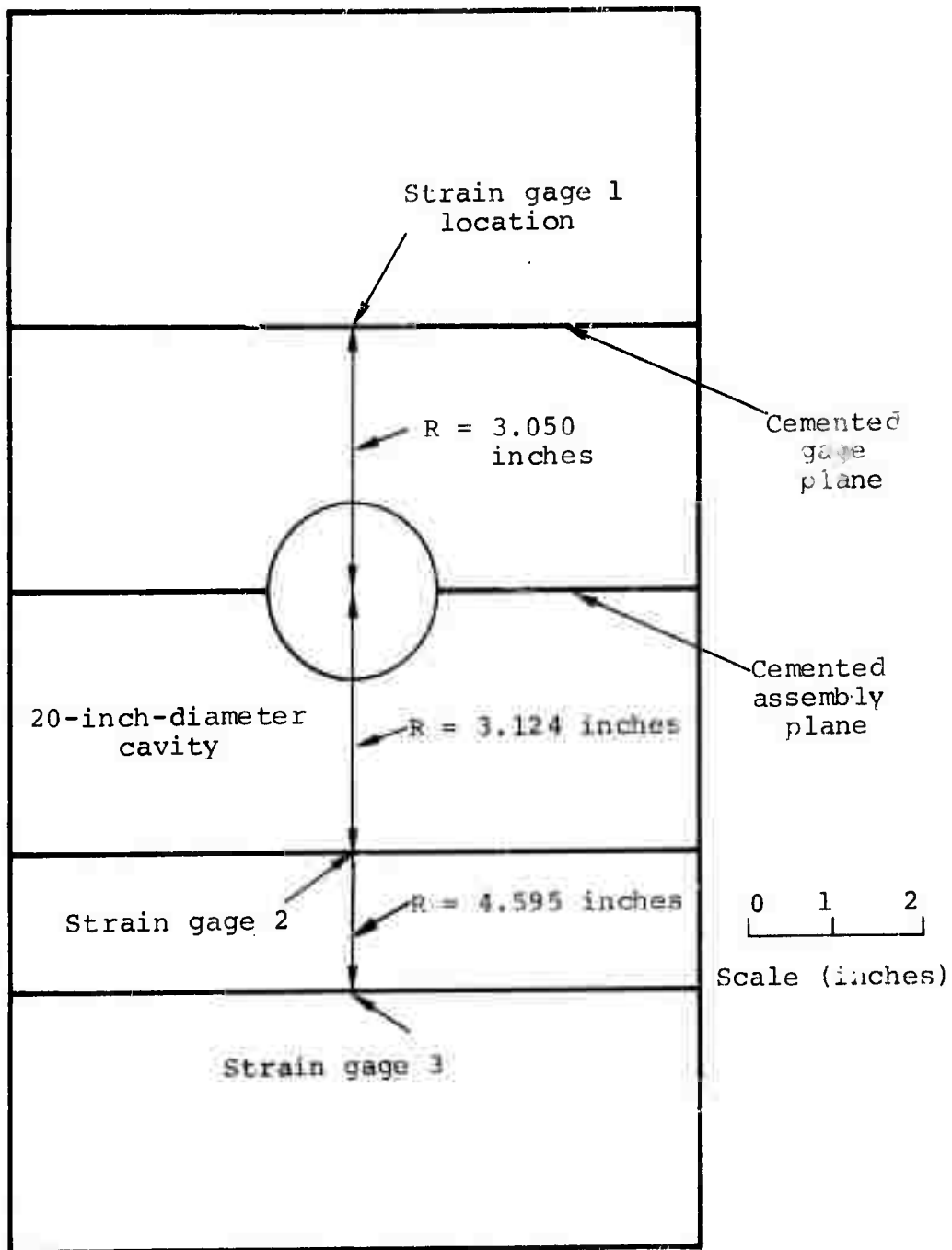


Figure 12 Schematic of salt block used for Shots 240-3c, 240-4, and 240-5, showing location of strain gages.

Post-shot evaluation of the salt block after firing shots 240-3, 240-4, and 240-5 indicated that this cemented assembly plane had maintained its integrity during the shots. There was very little evidence of injection of hot gaseous detonation products along this plane as compared to the salt block used in the first series. In addition, the location of strain gages in this salt block is preferable to those used in the salt block of the first series. As shown in Figure 12, the strain gages are all located on planes parallel to the central parting plane. If there was any failure of the cemented parting plane and associated injection of high-pressure gas into this plane, then the anomolous signal so generated would have less tendency to perturb the spherically divergent shock wave seen by the strain gages. Consequently, it is believed that the larger-amplitude and broader-wave profiles observed in the second series of shots are more representative of true behavior.

Because of some questions about the effects of the large grain size of the Texas salt dome material upon strain gage coupling and response and in order to investigate the effects of work hardening upon decoupling, it was decided that artificially pressed fine-grain salt should be used for the third series of small-scale decoupling experiments. Two large blocks of artificially pressed fine-grain salt were prepared by Autoclave Engineers of Erie, Pennsylvania. Each of these blocks was cylindrical in shape with an outside diameter of approximately 9 inches and a length of approximately 18 inches. One of these blocks had a conical opening with a 2-inch-diameter hemisphere at its bottom and pressed into the salt block. To eliminate machining of a test cavity, this block was used for the third series of experiments.

The overall geometry and the strain gage locations for the artificially pressed salt block used in the third series of small-scale decoupling experiments is shown schematically in Figure 13. In this block all three strain gages were located along a single radial direction at radial distances from the center of the cavity of approximately 3, 4, and 6 inches. A spherical decoupling cavity was created in this block by machining a tapered plug of aluminum to fit the tapered hole pressed into the block. As indicated in Figure 13, a hemispherical cavity was machined in the end of the tapered aluminum plug and the 1/4-inch-i.d. tube used to provide detonator access to the center of the cavity was placed in the center of this plug. The detonable-gas fill line was inserted into the test block through a hole drilled into the cavity from a cylindrical outside surface of the test block.

The excellent data obtained with the high-frequency strain gage amplifiers in earlier shots indicated that this type of amplifier should be used on all strain gages in this third series of small-scale decoupling experiments. Consequently, the strain gage amplifier box was modified to contain three high-frequency amplifiers and just one low-frequency amplifier. Strain gage 2 was monitored with both a high-frequency and a low-frequency amplifier in experiments 240-5 through 240-9.

In order to evaluate the effect of various gas mixtures upon the characteristics of detonation and the possible quality of data in both small and large scale experiments, tests utilizing different gas mixtures were included in the third series of experiments. Test Shots 240-6 and 240-9 used methane and oxygen in the ratio of 1:1.6, as in earlier experiments. In Shots 240-7 and 240-8, however, a methane-oxygen ratio of 1:2 was used. All of these experiments were conducted with a confining pressure of 2500 psi, as were all preceding experiments.

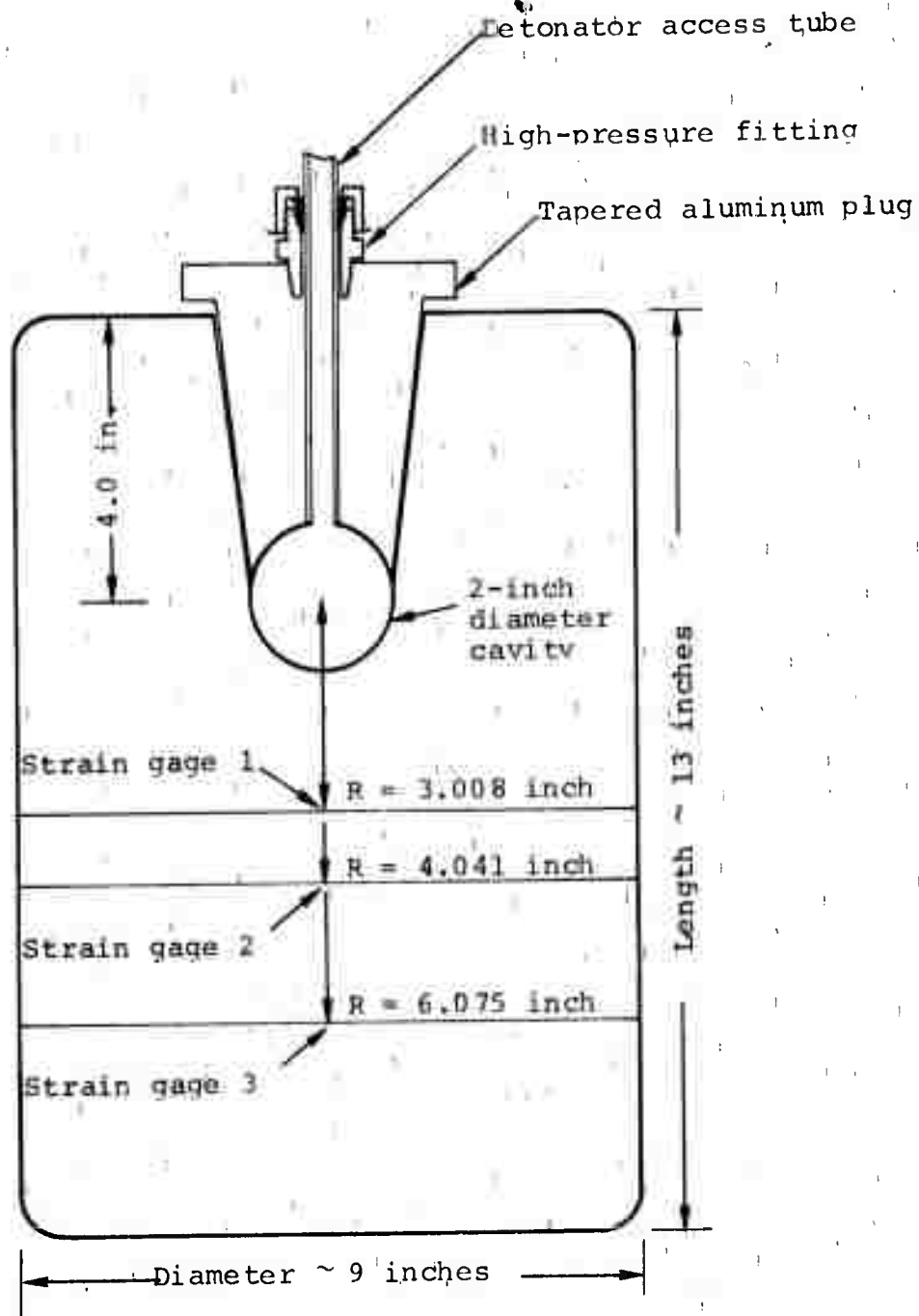


Figure 13 Schematic of salt block used for Shots 240-6 through 240-9, showing location of strain gages with respect to tapered aluminum plug.

Displacement-time histories obtained from the three strain gages in Shots 240-6 and 240-9 are illustrated in Figure 14. The strain gage records obtained in Shot 240-6 were generally of high quality and had a character in general agreement with the displacement-time histories observed in earlier experiments. The peak radial displacement monitored by the strain gages in Shot 240-6 fired with an initial detonable gas pressure of 220 psi, was in very close agreement with that obtained in a comparable shot fired a coarse-grained natural rock salt (Shot 240-3c). Because of its large radial distance from the cavity (approximately 6.0 inches) strain gage 3 exhibited a low signal-to-noise ratio as discussed earlier, and the record for this strain gage should not be considered as valid as those for strain gage 1 and 2. In Shot 240-9, which was fired with an initial gas pressure of 440 psi, significant amounts of electrical noise were observed on the strain gage oscilloscope records. This noise was again believed to be due to the generation of ground loops caused by shorting of the steel MDF tube to the steel high-pressure chamber. This electrical noise was such that the strain gage records for gages 1 and 3 are of minimal value. As shown in Figure 14, however, a good record was obtained for strain gage 2. The peak radial displacement observed by strain gage 2 in Shot 240-9 does not show the marked increase in decoupling which had been observed for shots fired at this pressure in the coarse-grained salt. The significance of this result will be discussed in more detail later.

Two experiments, 240-7 and 240-8, were conducted using methane and oxygen in the ratio of 1:2. Excellent strain gage records were obtained from all strain gages in both of these experiments. Displacement-time histories obtained from the three strain gages for the two shots conducted with initial

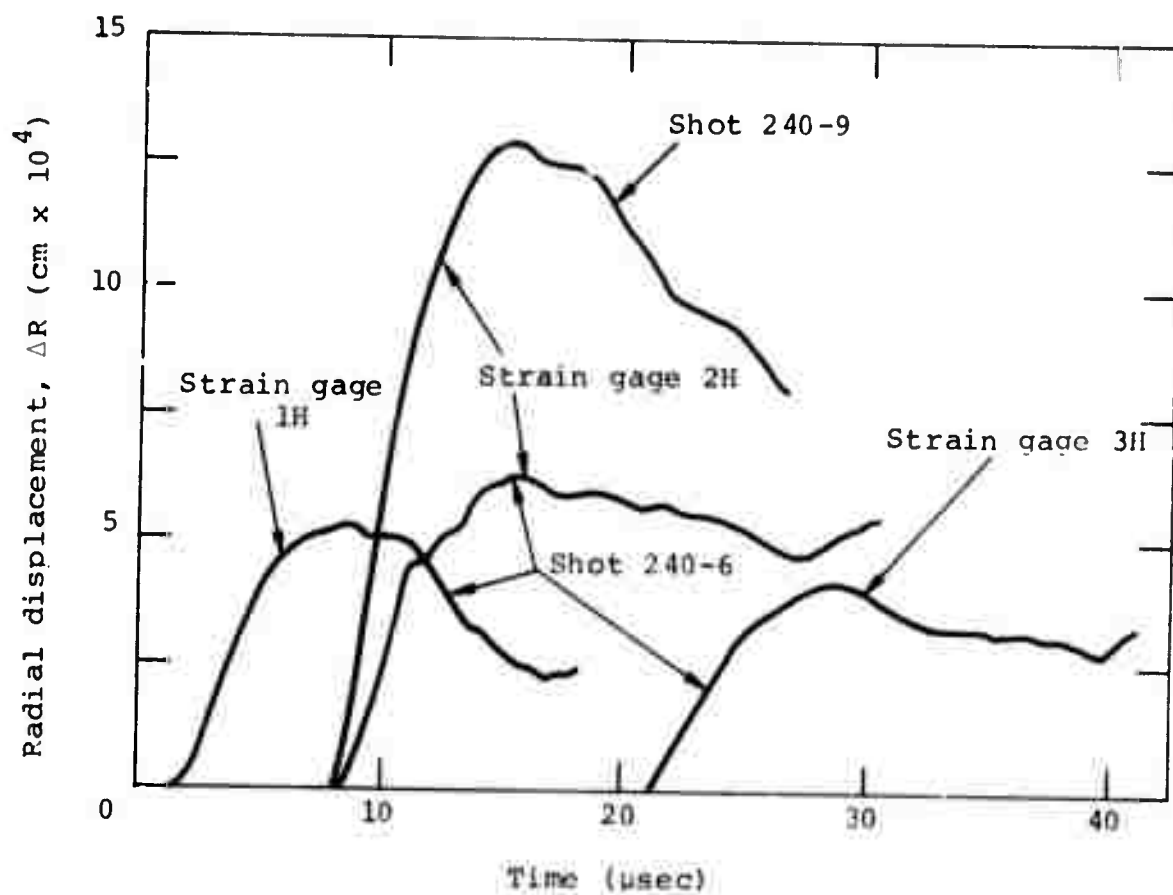


Figure 14 Reduced displacement versus time profiles obtained by strain gages in Shots 240-6 and 240-9.

detonable gas pressures of 220 and 440 psi are illustrated in Figure 15. The displacement-time records obtained from the shot fired at 220 psi (shot 240-7) show peak displacements appreciably greater than had been observed in earlier experiments conducted at this initial firing pressure. The greater peak displacement amplitude observed for a shot fired with a 1:2 detonable gas ratio may indicate that this mix is more nearly stoichiometric than the 1:1.6 ratio for detonation under these initial conditions.

The most interesting result obtained from the two experiments, 240-7 and 240-8, is the apparent lack of increased coupling associated with an increase in the initial detonable gas pressure to a level which had caused significant increases in coupling in earlier experiments. As indicated in Figure 15, the peak radial displacements observed in Shot 240-8 are not even double those observed in Shot 240-7, although the initial gas pressure is doubled. It is hypothesized that this lack of increased coupling is related to the work-hardened nature of the salt media in which the tests were fired.

Increased coupling can occur only if the cavity begins to respond non-elastically as the energy released by detonations within it is increased. Generally such non-elastic deformations can be effected either by tensile radial cracking associated with large hoop strains as occurred in the COWBOY experiments or by extensive plastic deformation of the material forming the cavity as occurred in the SALMON shot and as probably occurred in the earlier high-pressure shots utilizing a coarse-grained salt in this experimental program. The high confining pressure (2500 psi) used in these experiments could serve to preclude tensile radial cracking, especially at the stress levels generated by the

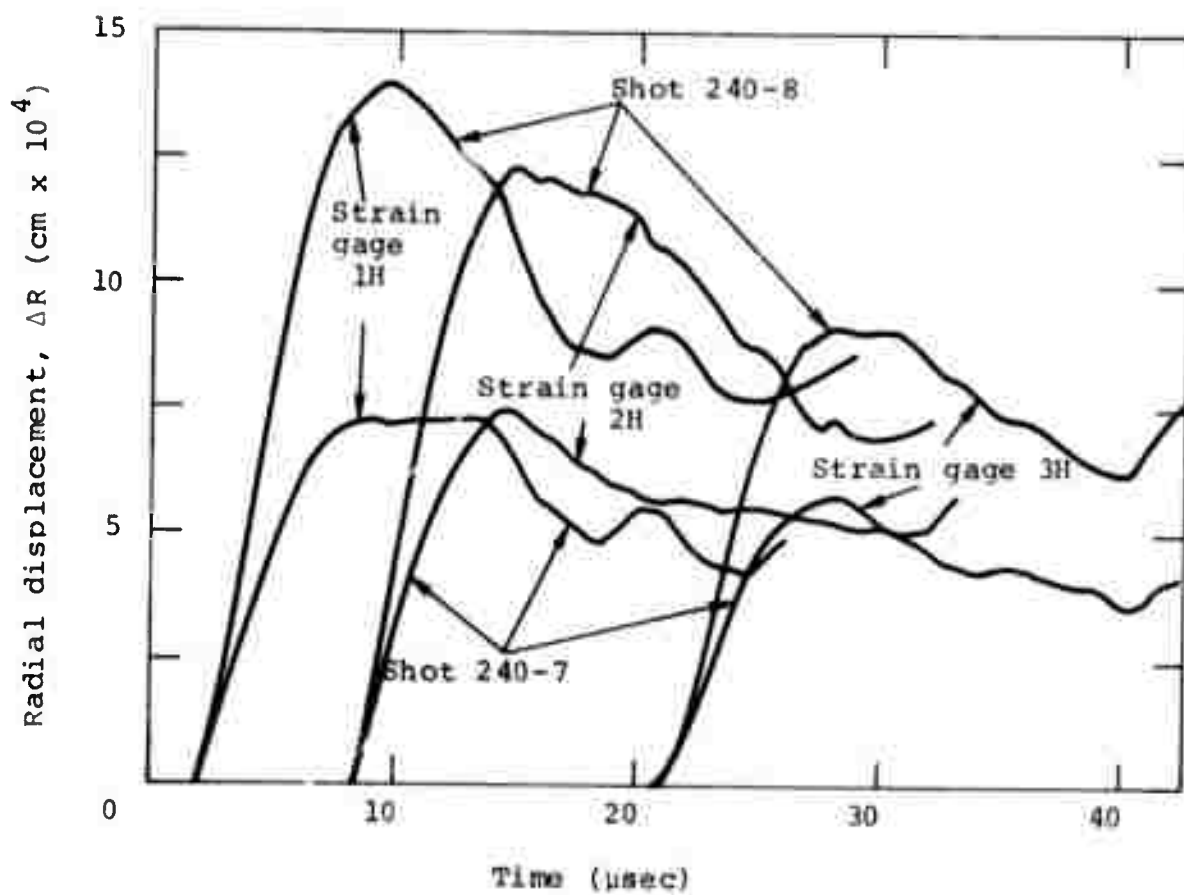


Figure 15 Reduced displacement versus time profiles obtained by strain gages at three radii in Shots 240-7 and 240-8.

detonable mixtures used. Because the artificially pressed salt was subjected to extensive deformation and work-hardening during the pressing operation, it would be expected that the stress levels to initiate plastic flow in this material would be significantly higher than for the naturally annealed coarse-grained salt.

3.3 DATA ANALYSIS

Analysis and evaluation of the experimental data were conducted using three different approaches. As indicated in the preceding section, the peak radial displacements as measured by strain gages at various locations in the test salt blocks were compared to an correlated with the explosive energy in the cavity and the material in which the test was conducted. In an effort to more quantitatively define the displacement response at the various strain gage locations, all high-quality displacement-time profiles were subjected to a spectral analysis. Finally, the displacement-time data and the associated response curves obtained from the small-scale decoupling experiments were appropriately scaled and compared with the results of one-dimensional finite-difference calculations made for a broad-base parameter study of large-scale decoupling phenomena.

Variations in peak radial displacement, as observed by strain gage measurements at several different radii in the nine decoupling experiments carried out, are generally in good agreement with anticipated results. Any significant deviations from expected behavior can be attributed to experimental difficulties, such as the poor detonable gas mix that probably existed in Shot 240-5. Increases in peak radial displacement by a factor of 3.5 in the doubling of explosive energy of Shot 240-2 as compared to 240-1, and a factor of 2.5 in Shot 240-4 as compared to 240-3c, provide experimental verification of the large scale cavity decoupling theory. In both of these higher-energy experiments

(240-2 and 240-4), the naturally annealed coarse grained salt would be expected to yield plastically at the higher stress levels generated at the cavity wall. According to the theory of large-cavity decoupling, such yielding at the cavity wall would increase the radius at which all deformation became elastic and would accordingly increase radial displacement seen at any radius over that which would be seen if the wall of the cavity were to respond elastically. It is unfortunate that the pressure and mix of the detonable gas used in Shot 240-5 are not better known and that more experiments in the coarse-grained salt could not be conducted at higher firing pressures.

Peak radial displacement measurements obtained in the third series of shots (240-6 through 240-9) indicate that a stronger material can provide a better decoupling behavior independent of the effects of overburden pressure. Comparison of peak radial displacements obtained in Shot 240-8 with those from 240-7 indicates that no increased coupling occurred with a doubling of the explosive energy content within the cavity. This effect may be readily attributed to the higher strength resulting from work-hardening of the salt associated with the artificial pressing of the test blocks. The one good strain gage record obtained in Shot 240-9 does indicate some increase in coupling associated with a doubling of the explosive energy as compared to Shot 240-6. This increased coupling by the small factor of 2.2 might be attributable to a weakening of the salt either by damage associated with the firing of the three previous shots (240-6 through 240-8) or the thermal annealing of the salt by the hot detonation products of these earlier experiments.

In carrying out this third series of experiments, it was hoped that at least one experiment could be conducted with an even higher energy source, such as would be obtained with a 660-psi detonable-gas mix in the test cavity. Unfortunately, a severe fracture in the salt block was formed during the execution of Shot 240-9. Besides damaging the salt block for possible use in further experiments, this fracture also served to rupture the impermeable coatings around the salt block, thus allowing the high-pressure nitrogen confining media to penetrate the experimental cavity. An experiment with a higher energy source would serve to further confirm and possibly extend the effects of high-strength material properties upon improved decoupling performance.

Observation of the peak radial displacements observed by various strain gages is not necessarily the most valid way of analyzing decoupling phenomena. The peak displacements observed at any strain gage location will be the result of the additive effect of displacements occurring over a broad range of frequencies. Since the very high frequency portions of the displacement waves will not be propagated for large seismic distances, they are not particularly pertinent to the decoupling problem. Only lower-frequency components of the displacement history are of particular interest.

In order to critically evaluate the frequency content of the displacement-time profiles obtained at various gage locations, a spectral-analysis computer program was modified and used to obtain response spectra. Peak displacement and acceleration response spectra and Fourier amplitude spectra were obtained for all strain gage records possessing enough quality to be amenable to the analysis. The response spectra represent the

actual peak values of displacement, and acceleration obtained during the analysis of a displacement-time profile. Because of the special interest in the peak radial displacement as a function of frequency in the decoupling problem, and because the displacement response spectra were most indicative of differences between various displacement in time profiles, nearly all the analysis was directed towards the study and evaluation of displacement response spectra. A discussion of the spectral analysis method is given in Section 4.1.3 and in Figure 45.

In order that the response spectra obtained from the small-scale data could be more meaningfully compared with the results of large-scale parametric calculations and actual field measurements, the experimental displacement-time records were appropriately scaled. As has been noted, the small-scale experiments were reduced by a factor of 650 from the MIRACLE PLAY field experiments. Both displacement and time would have to be multiplied by 650 to scale the small-scale results for comparison with full-scale calculations or field data. All displacement-versus-time data from the small-scale experiments were scaled by a factor of 650 before spectral analyses were performed. Consequently, the peak displacement amplitudes and the frequencies indicated in Figures 16 through 20 are comparable to the large-scale calculational results of Figure 21.

Due to the large-amplitude electrical noise observed on the strain-gage records for Shot 240-1, these records were not suitable for a meaningful spectral analysis. Consequently, no efforts were made to conduct spectral analyses of the reduced displacement-versus-time profiles obtained in this experiment. Spectral

analyses were conducted on the scaled displacement profiles from Shot 240-2. These response spectra were in general agreement with those obtained on profiles from other shots, but since there are no spectra with which they may be directly compared, they are not shown here.

The displacement response spectra obtained by applying the analysis to the displacement profiles obtained from strain gage 2L in Shots 240-3c, 240-4, and 240-5 are illustrated in Figure 16. As noted in Section 4, the strain gage displacement profiles were believed to be valid for some 25 microseconds of recording time. When scaled by a factor of 650 to correspond to the dimensions of the SALMON/STERLING cavity, these recording times would correspond to a record of some 17 milliseconds duration. Since wavelengths with periods more than twice as long as the maximum recording time would not be adequately resolved, the values of peak spectral displacement for frequencies below 30 Hz could be higher than calculated. The most significant feature of the response spectra illustrated in Figure 16 is the factor of 2.57 difference at 10 to 70 Hz between the spectra obtained from strain gage 2L in Shots 240-3c and 240-4. Since the detonable gas energy in the cavity was only twice as high in 240-4 as it was in 240-3c, these response spectra confirm the increased coupling associated with the higher-energy source used in Shot 240-4. The response spectra for strain gage 2L in Shot 240-5, also illustrated in Figure 16, further substantiates that the anticipated displacements were not observed in this experiment. This indicates further that a poor detonable gas mix probably existed in the cavity at the time the shot was fired.

The displacement response spectra obtained from the displacement history reduced from strain gage 2H in Shots 240-3c, 240-4, and 240-5 are illustrated in Figure 17. In the lower frequency range where these response spectra are most valid, the displacement response is in good agreement with a general displacement waveform observed in these experiments and the displacement response spectra obtained from the low-frequency amplifier records of the same strain gage. Comparison of the spectra obtained for Shot 240-4 with that from 240-3c indicates that their amplitudes in the 10- to 70-Hz range differ only by a factor of approximately 2.3 as opposed to the factor of 2.57 observed for the low-frequency strain gage records. This discrepancy may be due to an error in the calibration of one of the strain gage amplifiers used in the experiments or to some other unknown cause.

The displacement response spectra obtained from the reduced records of strain gage 1H in Shots 240-6, 240-7 and 240-8 are shown in Figure 18. Since Shots 240-6 and 240-7 were fired at identical initial pressures (220 psi), but with different gas ratios, these spectra should provide a good basis for evaluating the importance of gas mixtures.

Shot 240-6 with an initial methane-to-oxygen ratio of 1:1.0 shows a significantly lower displacement response at nearly all frequencies. In the 10- to 70-Hz frequency range, the displacement response for Shot 240-7, with a methane-to-oxygen ratio of 1:2, is typically 1.5 times greater than the response observed in

Shot 240-6. The theoretical ratio in energy content (per unit volume) for a 1:1.5 mixture compared to a 1:2 mixture is 1:0.93 (Reference 10). The data of strain gage 1H thus appears to be quite anomalous. Careful review of the data indicates that electrical noise during Shot 240-6 made the strain gage baselines difficult to establish, especially for the close-in, early recording gage locations. Consequently, an error in baseline position giving smaller late-time (low-frequency) displacements is probably responsible for the difference in the spectra of strain gage 1H for Shots 240-6 and 240-7. However, as will be discussed later with reference to other strain-gages, displacement spectra for these two tests generally show larger displacements for Shot 240-7 than for Shot 240-6.

Shots 240-8 and 240-7 were fired with the same methane/oxygen ratios but with different initial pressures. As illustrated in Figure 18 there is a very consistent factor-of-two difference between the displacement response for these two shots for all scaled frequencies below 150 Hz. Since Shot 240-8 was fired with twice the initial pressure and energy as Shot 240-7, the doubling of displacements indicates a fully elastic and, therefore, completely decoupled behavior. This lack of increased coupling, even when the equilibrium cavity pressure exceeds the overburden pressure by a factor of two, is significant. If the salt were to deform plastically as was observed to be the case for the natural rock salt blocks used for Shots 240-1 through 240-5, then larger displacements would have definitely been observed at the higher equilibrium cavity pressure of Shot 240-8.

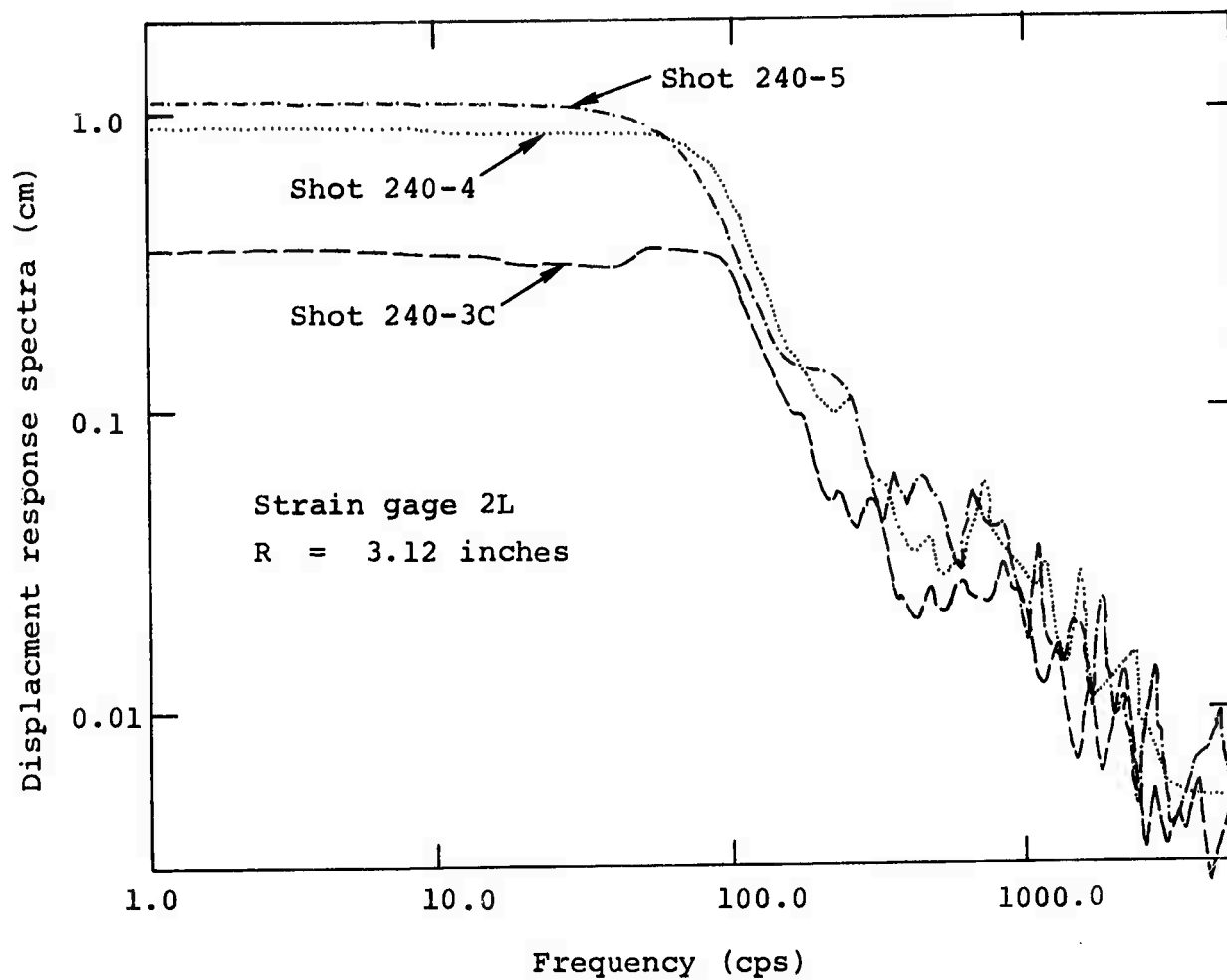


Figure 16 Displacement response spectra obtained from records of strain gage 2L for shots 240-3c, 240-4 and 240-5.

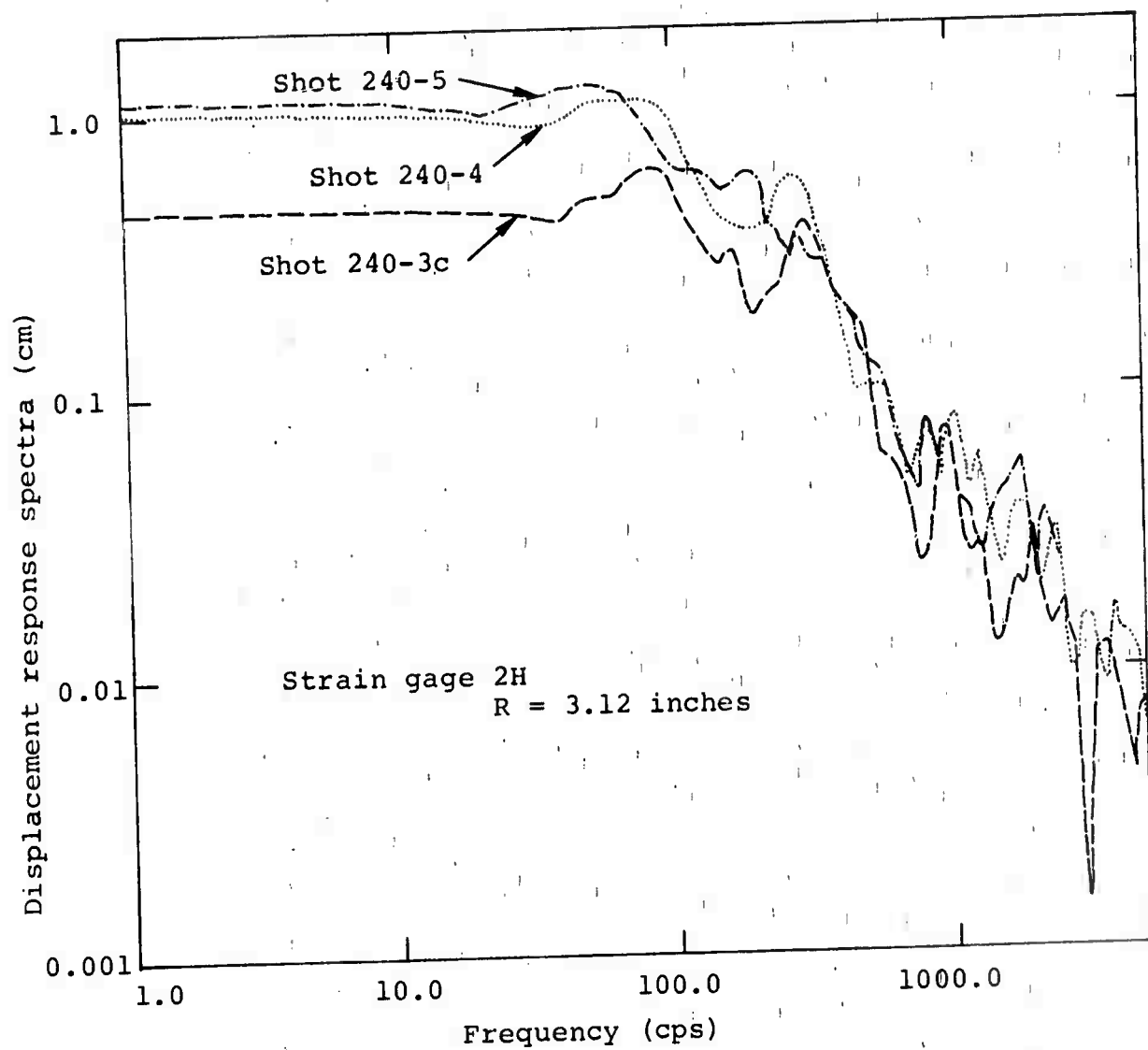


Figure 17 Displacement response spectra obtained from records of strain gage 2H for shots 240-3c, 240-4, and 240-5.

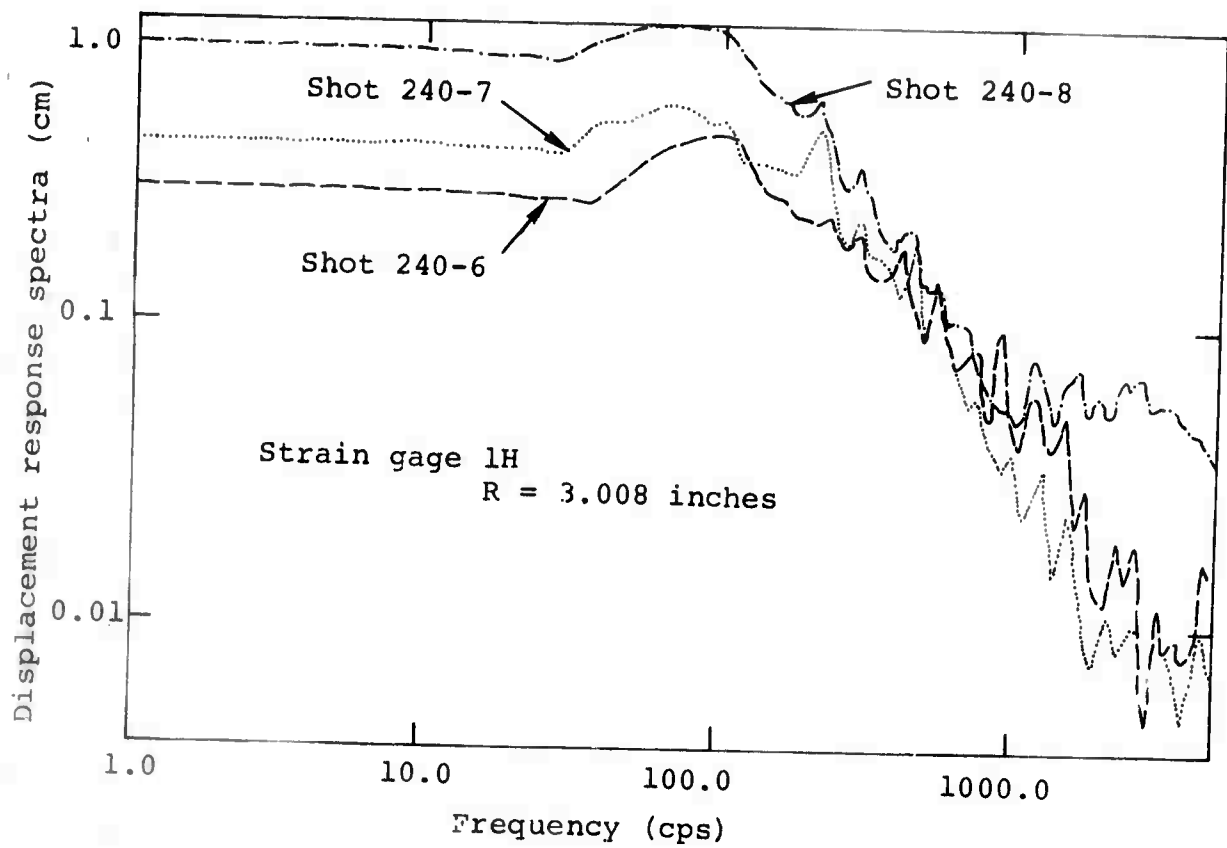


Figure 18 Displacement response spectra obtained from records of strain gage 1H for shots 240-6, 240-7, and 240-8.

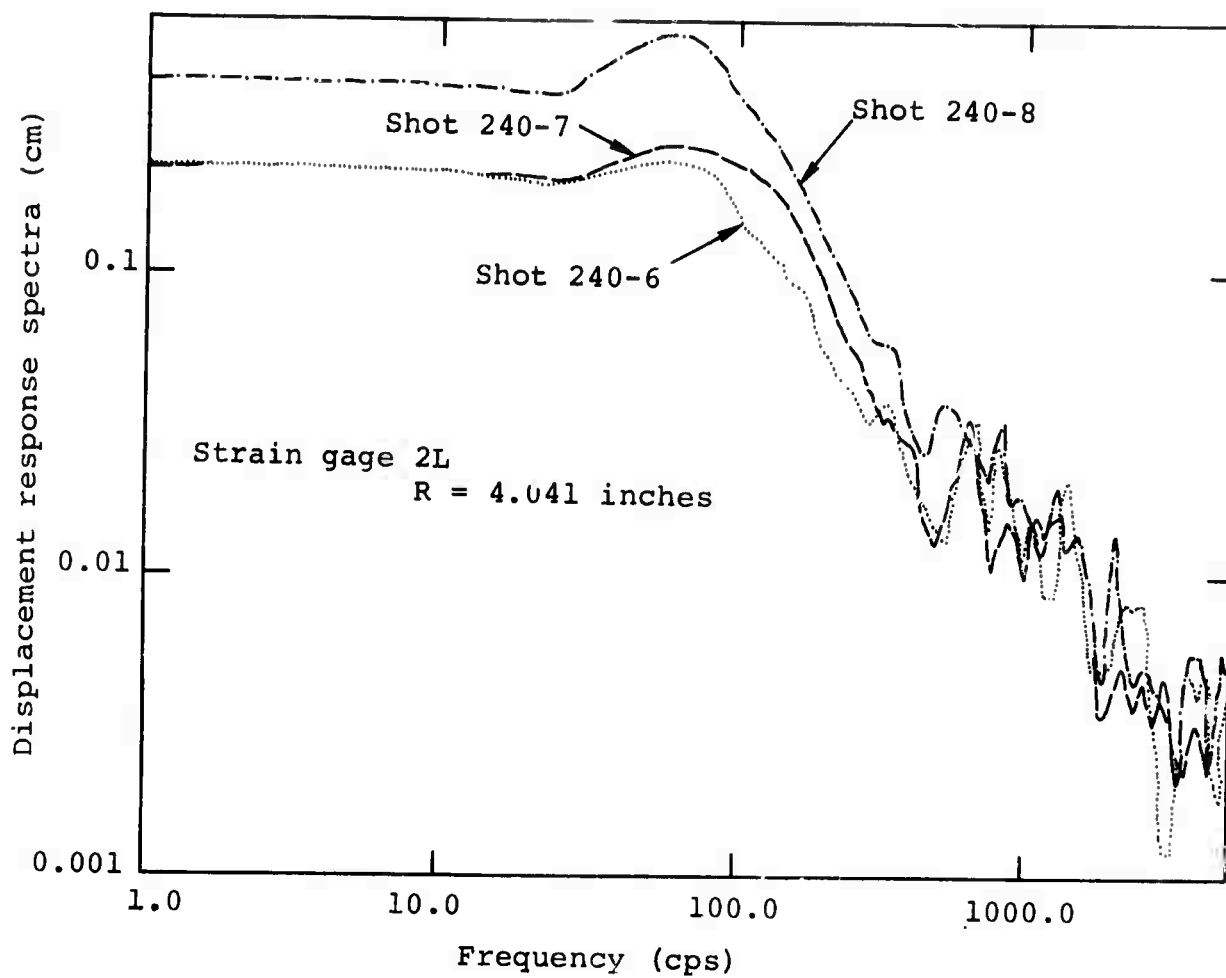


Figure 19 Displacement response spectra obtained from records of strain gage 2L for shots 240-6, 240-7, and 240-8.

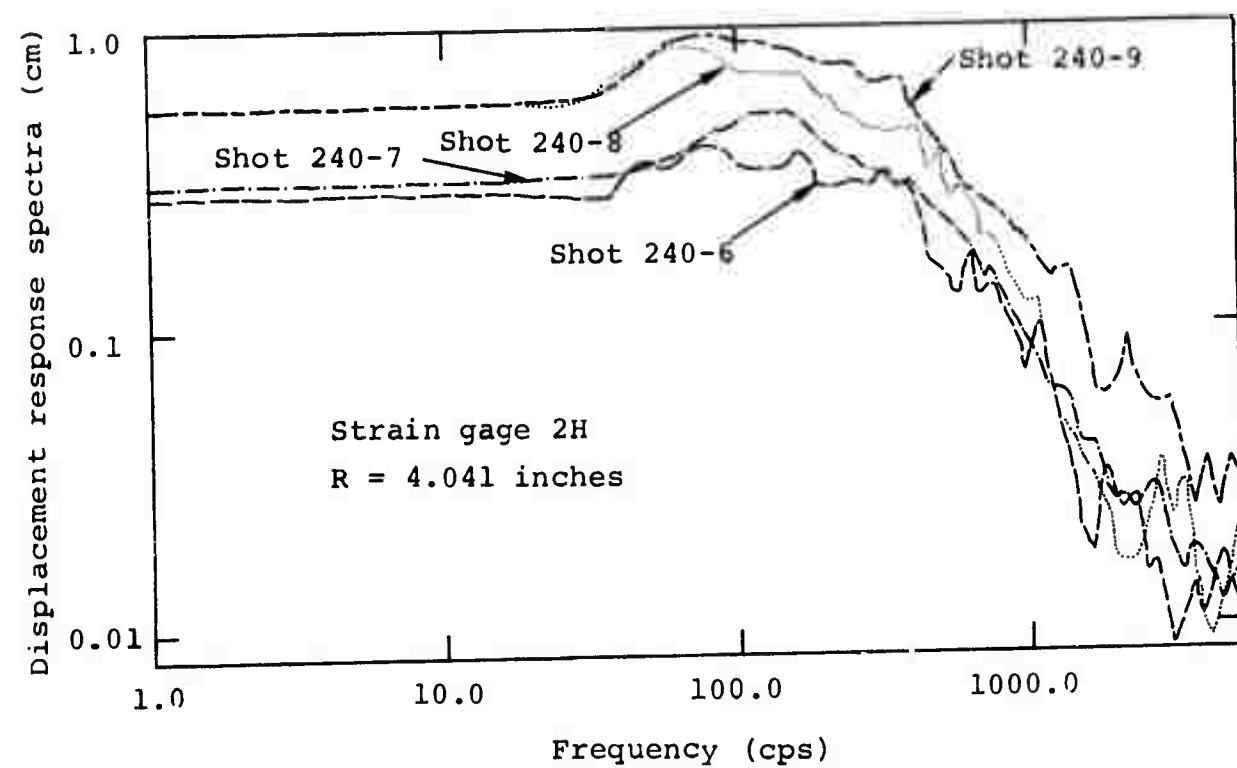
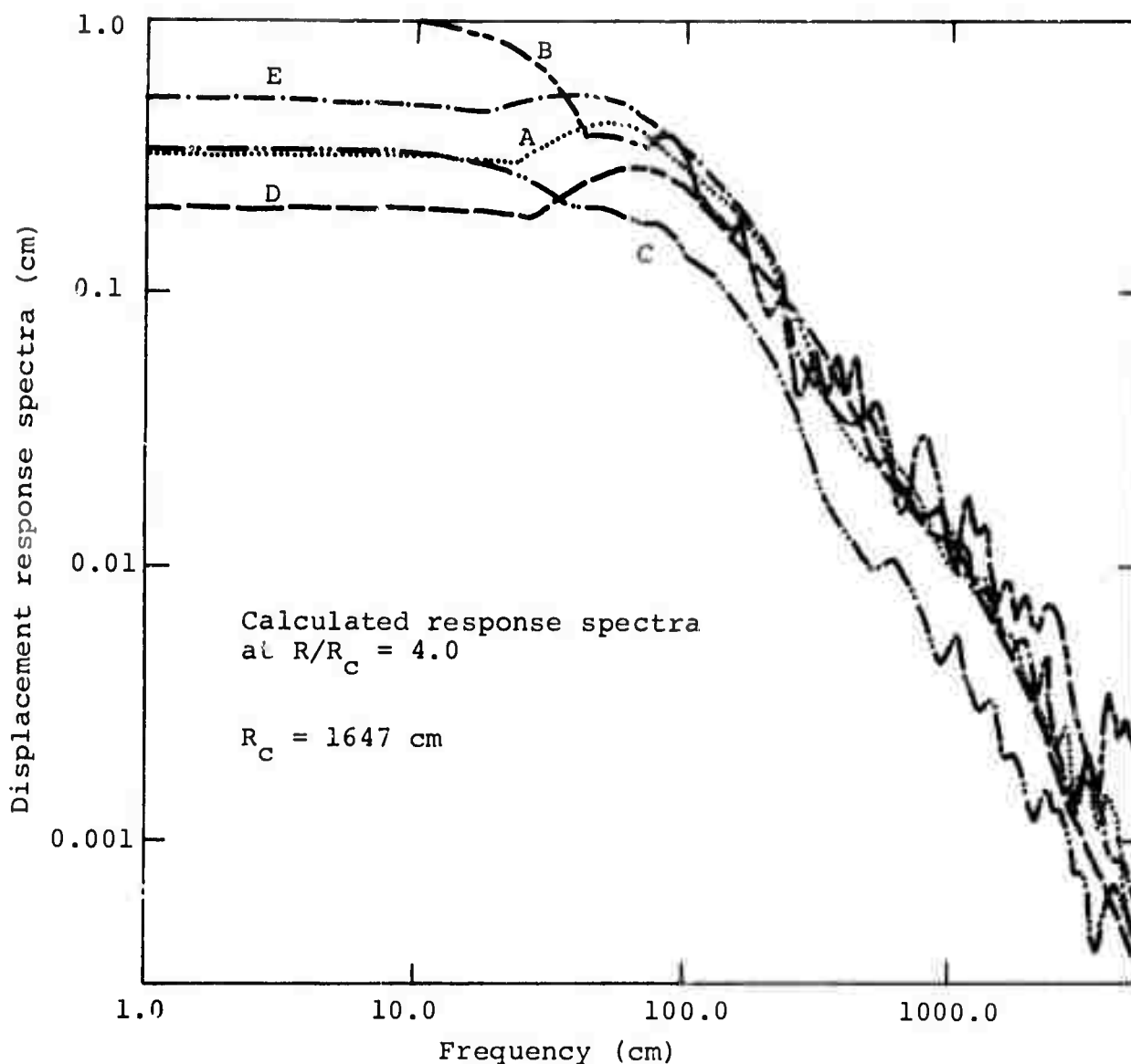


Figure 20 Displacement response spectra obtained from records of strain gage 2H from shots 240-6 to 240-9.



A	MC	P = 360	OB = 180	Key	MC = Mohr-Coulomb yield
B	MC	P = 360	OB = 0		VM = von Mises yield
C	MC	P = 180	OB = 0		OB = Overburden
D	VM	P = 180	OB = 0		P = Cavity equilibrium pressure
E	VM	P = 360	OB = 0		

Figure 21 Displacement response spectra obtained from large-scale calculations illustrating various energy sources and rock yield models.

If the salt were to respond purely elastically in compression but were to fail in tension at very low stress levels, then equilibrium cavity pressures up to three times the overburden pressure could be sustained before failure, and by definition, increased coupling would occur. However, the well-established failure of rock under conditions of high pore pressure (Reference 11) would dictate that tensile failure at lower cavity pressures should probably occur.

The artificially pressed salt used for Shots 240-6 through 240-9 might be expected to respond elastically to compressional loading due to the work-hardened nature of this material. It was not possible to anneal the salt blocks after they had been pressed and the high pressures (30,000 psi) required to press the salt to the desired density indicated that severe work-hardening was taking place during the pressing operation. The artificially pressed salt still had some porosity and permeability and it is surprising that pore-pressure effects at the higher firing pressures were not more pronounced. Additional efforts to investigate this phenomenon would certainly be warranted.

Excellent strain gage displacement records were also obtained from strain gage 2 in Shots 240-6, 240-7 and 240-8. The output of this gage was monitored by both a low-frequency and a high-frequency amplifier. A reasonably good high-frequency record was also obtained from strain gage 2 in Shot 240-9. The displacement response spectra calculated from these strain gage records are shown in Figure 19 for the low-frequency amplifier records and in Figure 20 for the high-frequency amplifier records.

The displacement response spectra shown in Figures 19 and 20 generally confirm the conclusions drawn from the response spectra of strain gage 1H shown in Figure 18. Shots 240-8 and 240-9, fired with twice the initial pressure of Shots 240-6 and 240-7, do not show any increased coupling due to the higher equilibrium cavity pressures. In fact, the displacement response spectra for strain gage 2H (Figure 20) show less than a factor-of-two increase between the low-pressure and high-pressure shots. This less than expected increase in displacement response can probably be attributed to the poorer recording characteristics of the strain gage system at larger distances from a test cavity.

The displacement response spectra obtained from both the low- and high-frequency records of strain gage 2 in Shots 240-6 and 240-7 do not show the large discrepancy which appeared in the records of strain gage 1H as already discussed. The peak displacements observed in Shot 240-7 are still slightly higher than the 240-6 displacements although theoretical considerations (Reference 10) indicate otherwise. Quite possibly the assumption that maximum detonation energy release is realized when the reaction products are just CO and H₂O is erroneous. If reactions leading to the formation of CO₂ can contribute to the energy of detonation, then the 1:2 methane-oxygen mixture would have a higher-energy output, and larger displacements would be expected.

As a final evaluation the results of the spectral analyses of scaled experimental data were compared with displacement spectra obtained from the output of several one-dimensional parametric calculations. These calculations were recently conducted within the theoretical portion of the research program (Contract No. DASA 01-70-C-0094) that covered the small-scale experiments reported upon here. These calculations were designed

to critically demonstrate and evaluate the possible effects upon decoupling phenomena of various material property, explosive loading, and overburden stress conditions. The displacement response spectra for several calculations particularly comparable to the small-scale experiments are illustrated in Figure 21. A good comparison between calculated and experimental results is shown in Figure 22. Both records were made from data at approximately 4 cavity radii for approximately 360 bar cavity equilibrium pressure and 180 bar overburden. Natural cavity resonance is at 49 cps (see Section 4.2) and this can be clearly seen. The calculated amplitude at the lower frequencies is lower than the experimental value but the yield surface used for the calculation may be higher than that of the salt used in the experiment. Additionally the overburden in the calculation was a constant 180 bars and in reality it should decrease near the cavity. Thus the artificially constant overburden in the calculation suppresses yielding near the cavity and results in the lower amplitudes calculated for the low frequency portion of the section. Nevertheless the good agreement attests strongly to the validity of the experimental technique, the strain gage diagnostic system and the calculational technique. The displacement response spectra obtained from the data of strain gage 2L in Shot 240-8 (Figure 19) is also very comparable to two of the calculated curves shown in Figure 21. Three of the response curves are for calculated models using a 360-bar equilibrium cavity pressure, equivalent to that of Shot 240-8. One of these curves is for a model with a 180-bar (2600 psi) overburden pressure--a Mohr-Coulomb yield model (MC-360 at 180). The response spectra for Shot 240-8 lies intermediately between the calculated spectra for the Mohr-Coulomb model with overburden and that for a Von Mises model without overburden (VM-360 at 0). This comparison indicates that some yielding of the salt did take place in Shot 240-8.

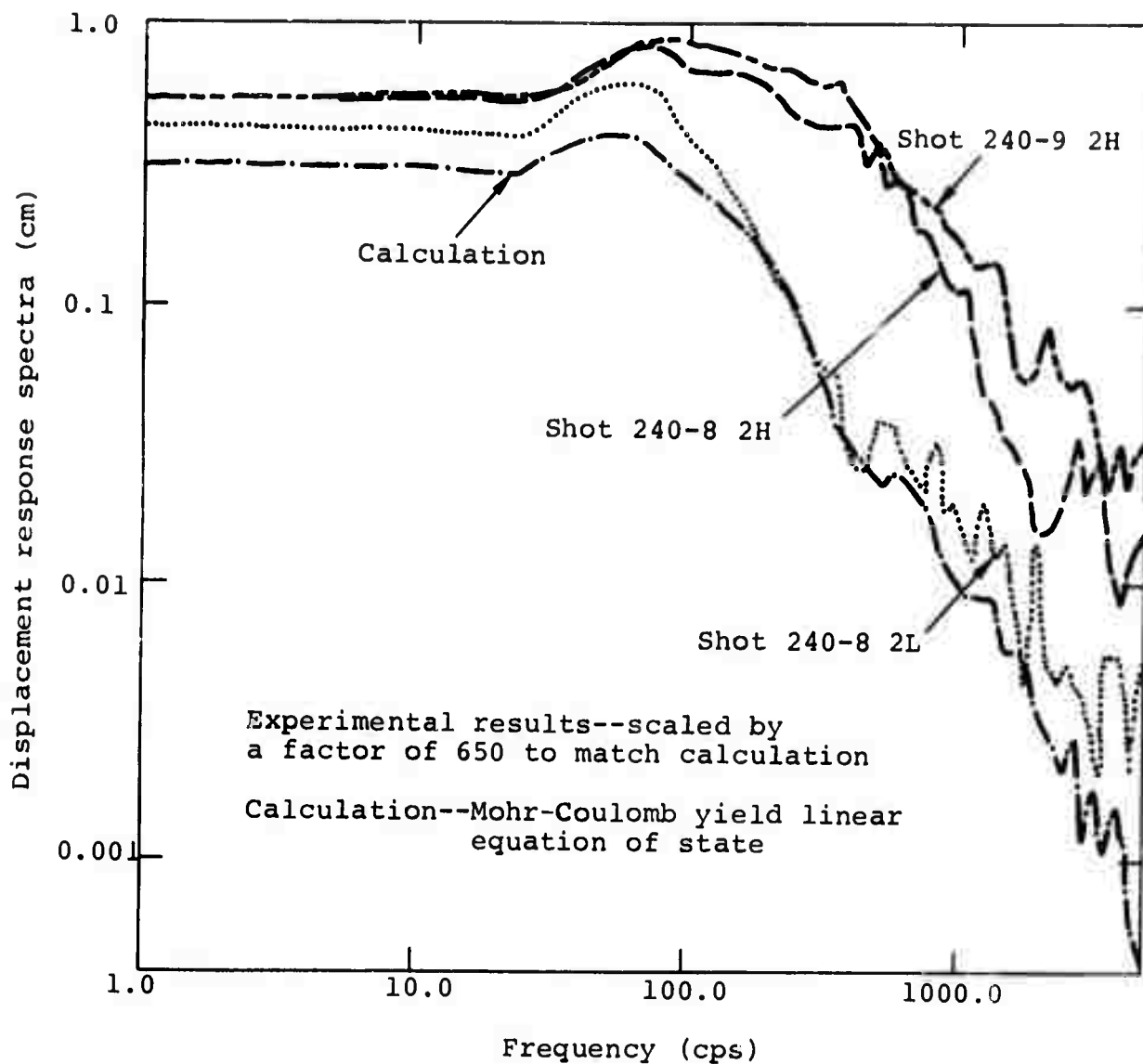


Figure 22 Comparison of experimental and calculational results for 180 bar overburden, approximately 360 bar cavity equilibrium pressure at 4 cavity radii.

The effects of having a very weak material are illustrated by the curve for a Mohr-Coulomb model without overburden (MC-360 at 0) in Figure 21. Because Mohr-Coulomb yielding is pressure dependent, the absence of overburden pressure in the calculation allows extensive permanent deformation to take place. This deformation may continue into late times as radial displacements effect a reduction in hoop stresses and thus mean pressure, which allows for additional Mohr-Coulomb yielding. This late-time yielding is illustrated by the rapid increase in displacement response at lower frequencies. Since none of the experimental results show such low-frequency behavior, it is apparent that all of the salt materials used in the experiments were not subject to such late-time yielding, as would be expected with the presence of overburden.

3.4 SUMMARY

A capability for conducting small-scale experiments to study decoupling phenomena was successfully developed, tested, and used to evaluate some of the basic concepts of decoupling theory. Because of the low cost and high data quality associated with small-scale tests, numerous parameters of possible interest to decoupling may be studied in a cost effective fashion. Because overburden pressures, test materials, and explosive loading conditions may be varied as desired in small-scale experiments, this capability complements both field tests and calculations and would be preferable to in situ experiments (both large and small scale) for many decoupling studies.

The greatest problems that had to be overcome in developing the small-scale experimental capability were associated with detonating methane-oxygen gas mixtures in small cavities and with eliminating electrical noise from the strain gage diagnostic system. Both of these difficulties were overcome with the successful development of a PETN detonator fired by a long delay line of MDF. The only aspect of the experimental system which could benefit from further development is the strain gage diagnostic technique for measuring radial displacements. Although high-quality and informative displacement-time histories were obtained with the strain gage technique, it is felt that any future studies of this type should utilize an electromagnetic-velocity gage diagnostic system.

Nine small-scale experiments were fired using the small-scale capability developed on this research program. With the exception of electrical noise problems in two of the experiments, excellent strain gage data were obtained from gages embedded in the salt material at various radii from a 2-inch-diameter "decoupling" cavity. Analysis of the strain gage records confirms the basis for the large-cavity decoupling theory. In natural rock salt, significant increases in coupling were observed as the energy released by detonation of a methane-oxygen mixture in the test cavity was increased. In an artificially pressed rock salt, increased coupling was not observed over the cavity pressure ranges studied. This phenomenon is definitely attributable to the work-hardened nature of this material resulting from the cold pressing used in preparing test blocks.

A data analysis technique involving a spectral response analysis was developed and used to further evaluate the data obtained from the small-scale experiments. The displacement response spectra obtained in this analysis revealed many features of the data that were not apparent in the reduced displacement-time curves obtained from the strain gage records. The displacement response spectra confirmed the increased coupling, or lack of it, observed in the displacement-time records. Comparison of these response spectra with those obtained from calculated (using a one-dimensional finite-difference code) displacement-time histories revealed very good agreement between the two.

Not all aspects of decoupling phenomena that are of interest could be investigated within the scope of the program. It would have been particularly informative to conduct a few experiments (in both natural and artificially pressed rock salt test blocks) using a higher initial gas pressure to obtain higher explosive

energy loadings of the test cavities. The results of such experiments would have extended the range and degree of increased coupling for the natural rock salt tests and would have established the pressure and energy levels at which increased coupling occurred for the artificially pressed salt. Any future small-scale decoupling experiments should probably include such tests.

SECTION 4

CALCULATIONS

4.1 CALCULATIONAL TECHNIQUE

4.1.1 Code Capability. Most of the calculations described in this section were carried out on the POD code. POD is a one-dimensional time-dependent finite difference Lagrange code, which is used to calculate the dynamic motion of continua including elastic-plastic and hydrodynamic media. The differential equations that govern the motions of these media are approximated by difference equations applied to a network of zones that describe the physical space occupied by the media. Groups of contiguous zones of the same material are described by constitutive equations which are coupled to the equations of motions. There are three possible symmetries--plane, cylindrical and spherical. The POD code offers a variety of initial and boundary conditions, an extensive equation of state and yield model library and many other specialized options developed and applied on a wide range of problems in continuum physics.

The two-dimensional calculation which was partially completed in the course of this contractual effort was carried out on the ELK code which is a coupled Eulerian-Lagrangian code. This code was developed specifically for calculating explosive phenomena in which the hydrodynamic area of the explosion is

calculated on an Eulerian grid and the elastic-plastic regions away from the explosion are calculated on a Lagrange grid coupled to the Eulerian grid. There are two possible symmetries--planar and axisymmetric. Most of the equation of state and yield models, boundary and initial conditions, and other special options available on POD, are available with ELK.

Both POD and ELK codes are compatible with Physics International's data display code which allow time histories, profiles of any variable, and shock trajectories to be plotted in almost any desired format.

In the calculations discussed in this report, the goal was to examine the stress waves generated by a violent explosion, after they had propagated for seismologically significant distances into the surrounding earth media. At large distance the kinetic energy density of outward propagating stress waves quickly decays because of the internal friction of the medium and the geometric divergence of the waves. Beyond a characteristic "elastic radius" the stress waves become ordinary acoustic waves and may be treated by the theory of linear elasticity. It is obvious that a considerable saving in computer time and storage space can be realized if the thermodynamic iterations and plastic flow computations are not performed for those finite-difference zones that lie beyond the "elastic radius" of the energy source of the problem.

Rather than modify the Lagrange continua mechanics codes to skip over these unnecessary calculations for elastic zones, Physics International developed an efficient elastic finite-difference code which couples to the Lagrange codes. This code,

called LEEK, computes elastic zones about 40 times faster than the Lagrange codes. LEEK is a sophisticated elastic code and may be used by itself as a tool for studying seismic wave propagation. The code is flexible enough to compute problems in which the elastic constraints are arbitrary functions of position and in which zones are arbitrary quadrilaterals. Either stresses or displacements may be specified as the boundary conditions. A description of the LEEK code is provided in Appendix A.

It is practical with the aid of advanced high speed computers such as the CDC 7600 to use the LEEK code to calculate detailed problems of seismological interest. For example, a one-dimensional LEEK grid with 1 meter zone width and 10,000 zones (10 km) can be coupled to an elastic-plastic Lagrange grid containing an explosive or fault source. Once the activity of the source has subsided, the Lagrange grid can be disconnected and the boundary of the LEEK code can be maintained at the equilibrium stress state, while the stress waves generated by the source are observed in detail as they propagate out several kilometers. A two-dimensional problem utilizing LEEK would be of much greater interest because of the inclusion of free surfaces and layering. However, to be practical, the zonal resolution would be coarser, for example on the order of 5 meters, and the extent of the grid might be limited to three or four kilometers. Stress, displacement and velocity histories can be saved at interesting locations and used as gage setting information, as data prediction or interpretation aids, or as forcing functions for observing structural response. The salient features of this type of calculation are the inclusion of free surfaces, arbitrary layers and compactible equation of state models. It should be noted that an increase in zone-cycle time results when a simple compaction equation of state is used rather than a linear equation of state in the LEEK code.

4.1.2 Calculational Procedure. The one-dimensional calculations reported herein were carried out in two basic steps. A hydrodynamic source calculation was made and the pressure history at the cavity wall was saved on tape. This boundary tape was then used to drive a Lagrange grid of salt. The LEEK grid of purely elastic salt was coupled to the outer boundary of the Lagrange grid at the appropriate time. Stress and velocity histories were saved on tape at locations of 1 cavity radius (the cavity wall), 4 cavity radii, 8 cavity radii and 10.7 cavity radii (the Lagrange--LEEK interface). The cavity radius for all the one-dimensional calculations was 1674 cm corresponding to the estimated volume of the STERLING/MIRACLE PLAY cavity. The LEEK grid extended from 10.7 cavity radii to 25.25 cavity radii, or nearly half a km from the source center. The calculational procedure is illustrated schematically in Figure 23.

The hydrodynamic source calculations were of two types--a mixture of methane-oxygen detonated at the center of the cavity and a nuclear source (with a higher shock reverberation frequency) also detonated at the center of the cavity. In all the source calculations the cavity wall was fixed--the very small effect of the wall motion on the gas pressure being neglected.

Three detonable source calculations (all with mixtures of $\text{CH}_4 + 1.5\text{O}_2$) were made, corresponding to 180 bars, 360 bars and 720 bars equilibrium cavity pressure. All three calculations were carried out to 0.1 sec.

One "nuclear" calculation was made as representative of a high frequency source with the same equilibrium cavity pressure, 360 bars, as one of the gas calculations. This high frequency

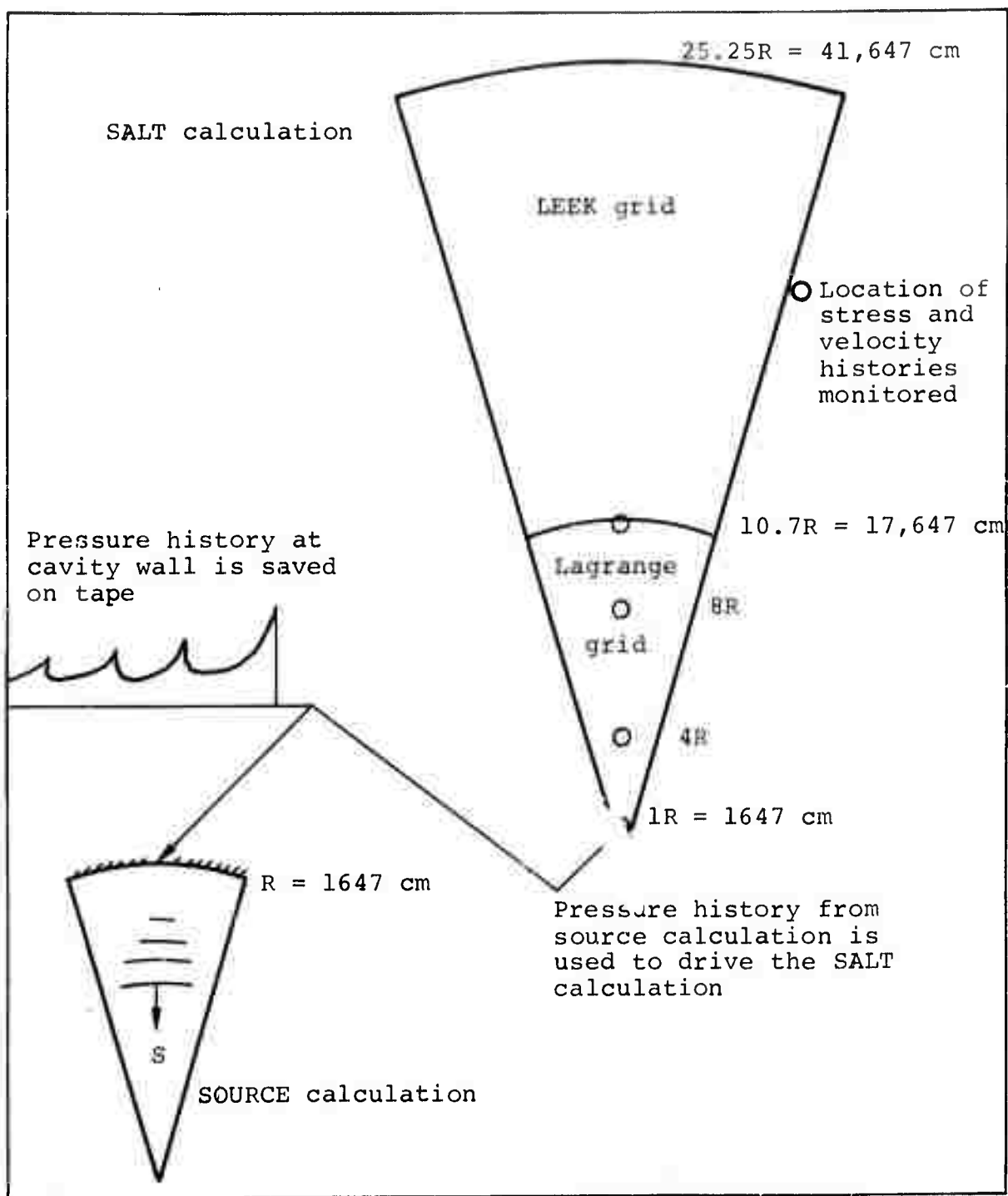


Figure 23 Calculational procedure for the one-dimensional POD problems.

source consisted of a 892 cm diameter ball of $\gamma = 1.3$ gas at 1.21×10^{-3} gram/cm³ and 18 kilobars. The rest of the cavity volume was void. Since the void occupied about 98% of the total volume, the temperature of the expanded fireball was high and the source frequency higher (by about a factor of 3) than the STERLING nuclear source. A more realistic model of a nuclear source such as STERLING would require the cavity volume outside of the fireball to be filled with ambient air and would require radiation diffusion between the hot fireball gases and the surrounding cold air. (A summary of the hydrodynamic source calculations is given in Table 3.) The cavity wall pressure histories of these source calculations were then applied to a Lagrange grid of salt (Figure 23). The Lagrange grid was chosen large enough so that the stress wave reaching the outer edge was always elastic. The grid started out with two-hundred 5 cm wide zones and was rezoned in stages to 10 cm wide zones, 20 cm wide zones, 40 cm wide zones and finally 80 cm wide zones. Upon the fourth rezone, the LEEK grid of three-hundred 80 cm wide zones was added and the problems run for about 0.1 second.

In the salt calculations several parameters were varied. Three different gaseous detonation sources and one high frequency nuclear source were used to drive salt with two different yield models (a von Mises and Mohr-Coulomb model), three different equations of state (one linear and two compaction), and overburdens of zero, 180 bars and 360 bars. The overburden pressures were generally constant throughout the Lagrange grid, however, one calculation was carried out with the equilibrium cavity stress distribution for a case in which no yielding occurred

TABLE 3

SUMMARY OF SOURCE CALCULATIONS FOR THE 3294 cm DIAMETER CAVITY

No.	<u>Type of Calculation</u>	<u>Initial Conditions</u>	<u>Equilibrium Cavity Pressure</u>
1	Gaseous Detonation $\text{CH}_4 + 1.50_2 + 1 \text{ atmos. air}$	$\rho = 1.3 \times 10^{-2} \text{ gram/cm}^3$ $\gamma = 1.2169$ $E = 6.535 \times 10^{-2} \text{ eu/gram}$ $D = 0.2507 \text{ cm}/\mu\text{sec}$	184 bars
2	Gaseous Detonation $\text{CH}_4 + 1.50_2 + 1 \text{ atmos. air}$	$\rho = 2.4 \times 10^{-2} \text{ gram/cm}^3$ $\gamma = 1.213$ $E = 6.897 \times 10^{-2} \text{ eu/gram}$ $D = 0.2550$	354 bars
3	Gaseous Detonation $\text{CH}_4 + 1.50_2 + 1 \text{ atmos. air}$	$\rho = 4.7 \times 10^{-2} \text{ gram/cm}^3$ $\gamma = 1.208$ $E = 7.36 \times 10^{-2} \text{ eu/gram}$ $D = 0.2596 \text{ cm}/\mu\text{sec}$	717 bars
4	Nuclear Detonation Evacuated Cavity Yield = 0.66 KT	$\rho = 1.21 \times 10^{-3} \text{ gram/cm}^3$ $\gamma = 1.3$ $E = 50 \text{ eu/gram}$ Fireball diameter = 892 cm	360 bars
5	Nuclear Detonation in air filled cavity Yield = 0.66 KT	$\rho = 0.335 \text{ gram/cm}^3$ $\gamma = 1.3$ $E = 1.094 \text{ eu/gram}$ Fireball diameter = 506 cm	360 bars

Fireball and cavity air artificially mixed and shrunk to 506 cm diameter ball to approximate the peak pressure of the first pulse.

prior to the explosion. It is possible to read in equilibrium overburden distributions around the cavity with yielding by utilizing Physics International's Static Code, but this was not carried out due to a lack of time and money.

A summary of the various salt calculations is given in Table 4 and a description of the equation of state models and yield models is given in Appendix B.

Several one-dimensional calculations were carried out with various zoning schemes and stability criteria to estimate the effect of the calculational technique on the answers obtained. Problems were run with constant 80 cm wide zones (rather than rezoning in four stages from 5 cm zones to 80 cm zones) and with constant 160 cm wide zones.

These same problems were re-run with different values of the safety factor for the Courant stability condition. In problems involving the propagation of elastic waves across a large number of finite difference zones, artificial dispersion of the wave occurs. This artificial dispersion of the waveform can be minimized by maintaining a constant zone width and operating with a time step as close to the Courant limit as possible, without jeopardizing the stability of the difference equations. This was done in all the calculations discussed above.

In the two-dimensional problem, the nuclear source and salt grids were calculated simultaneously. The cavity for this calculation was of pillbox geometry, with a diameter five times the

TABLE 4

SUMMARY OF ONE-DIMENSIONAL SALT CALCULATIONS

<u>No.</u>	<u>Source Type and Cavity Equilibrium Pressure</u>	<u>Yield Model</u>	<u>Equation of State</u>	<u>Overburden</u>	<u>Zoning and Courant Stability Condition Safety Factor (FRAT)</u>
1	Gaseous Detonation 180 bars	Mohr Coulomb	$P = 0.265 \mu$	0	4 rezones to 80 cm zones FRAT = 0.95
2	Gaseous Detonation 360 bars	Mohr Coulomb	$P = 0.265 \mu$	0	4 rezones to 80 cm zones FRAT = 0.95
3	Gaseous Detonation 360 bars	Mohr Coulomb	$P = 0.265 \mu$	180 bars	4 rezones to 80 cm zones FRAT = 0.95
4	Gaseous Detonation 360 bars	Mohr Coulomb	$P = 0.265 \mu$	360 bars	4 rezones to 80 cm zones FRAT = 0.95
5	Gaseous Detonation 720 bars	Mohr Coulomb	$P = 0.265 \mu$	360 bars	4 rezones to 80 cm zones FRAT = 0.95
6	Gaseous Detonation 360 bars	Mohr Coulomb	$P = 0.06 \mu$ Loading $P = -0.0044 + 0.265 \mu$ unloading	0	4 rezones to 80 cm zones FRAT = 0.95
7	Gaseous Detonation 360 bars	Mohr Coulomb	$P = 0.18 \mu$ Loading $P = 0.0018 + 0.265 \mu$ unloading	0	4 rezones to 80 cm zones FRAT = 0.95

TABLE 4

SUMMARY OF ONE-DIMENSIONAL SALT CALCULATIONS (cont.)

No.	Source Type and Cavity Equilibrium Pressure	Yield Model	Equation of State	Overburden	Zoning and Courant Stability Condition Safety Factor (FRAT)
8	Gaseous Detonation 360 bars	Mohr Coulomb	$P = 0.265 \mu$	180 bars	80 cm zones FRAT = 0.95
9	Gaseous Detonation 360 bars	Mohr Coulomb	$P = 0.265 \mu$	180 bars	80 cm zones FRAT = 0.67
10	Gaseous Detonation 360 bars	Mohr Coulomb	$P = 0.265 \mu$	180 bars	160 cm zones FRAT = 0.95
11	Gaseous Detonation 360 bars	Mohr Coulomb	$P = 0.265 \mu$	180 bars	160 cm zones FRAT = 0.67
12	Nuclear Detonation Evacuated Cavity 360 bars	Mohr Coulomb	$P = 0.265 \mu$	360 bars	4 rezones to 80 cm zones FRAT = 0.95
13	Gaseous Detonation 180 bars	von Mises	$P = 0.265 \mu$	30 bars-- 180 bars equili- brium stress distribu- tion	4 rezones to 80 cm zones FRAT = 0.95

TABLE 4

SUMMARY OF ONE-DIMENSIONAL SALT CALCULATIONS (cont.)

<u>No.</u>	<u>Source Type and Cavity Equilibrium Pressure</u>	<u>Yield Model</u>	<u>Equation of State</u>	<u>Overburden</u>	<u>Zoning and Courant Stability Condition Safety Factor (FRAT)</u>
14	Gaseous Detonation 180 bars	von Mises	$P = 0.265 \mu$	0	4 rezones to 80 cm zones FRAT = 0.95
15	Gaseous Detonation 360 bars	von Mises	$P = 0.265 \mu$	0	4 rezones to 80 cm zones FRAT = 0.95

height and a cavity volume equal to that of the one-dimensional spherical calculations. The source was a 984 cm diameter fireball of $\gamma = 1.3$ gas at 1.21×10^{-3} gram/cm³ and 15.6 kbars surrounded by ambient air. However, there was no radiation diffusion mechanism included in the description of the fireball gas or surrounding air. The salt was described by a linear equation of state ($P = 0.265 \mu$) and a Mohr-Coulomb yield model [$Y = \min(50 + 0.33 P, 200 \text{ bars})$], but zero overburden. The zoning of the Eulerian source grid and Lagrangian salt grid is shown in Figure 58. The calculation was run to 0.0075 sec, a time when the stress wave was just reaching the edge of the Lagrange grid. At this point, when the LEEK grid was to be added on, the calculation was terminated.

4.1.3 Spectral Analysis. As pointed out previously, stress and velocity histories were recorded at 1, 4, 8 and 10.7 cavity radii. The velocity histories were subjected to a spectral analysis in the following manner. The velocity history was integrated to yield the displacement history. The displacement time function was then used to drive an undamped mass-spring system (Figure 45). The equation of motion is solved and the Displacement Response Spectra (DSPEC) and Fourier Velocity Amplitude Spectra are computed. From the Displacement Response Spectrum, the Absolute Acceleration Response Spectrum [ASPEC = ω^2 DSPEC] can be derived. The spectra calculated for the one-dimensional problems are valid over the approximate range 10 cps to 2,000 cps. The lower limit of this range is imposed by the problem time of about 0.1 sec and the upper limit is governed by the onset of zonal noise. The Fourier Velocity Spectra, which is always equal to or less than the Displacement Response Spectra, is not strictly accurate as the driving functions are

terminated before they die away naturally. In most cases, as will be discussed below, the final character of the response spectra is established by the time the driving functions are terminated. A detailed discussion of the various response spectra can be found in Reference 12.

4.2 RESULTS

The cavity wall pressure histories for the three detonating gas source calculations are shown in Figures 24, 25 and 26. The initial gas conditions were taken from Reference 13 and an ideal gamma law description of the detonation products was assumed. The zoning of these calculations (80 zones initially) was sufficient to resolve the Chapman-Jouguet detonation pressure before the wave impinged on the cavity wall. At appropriate intervals after reflection of the spherical detonation wave, the gas calculation was dezoned to speed up the calculation. Representative pressure profiles for the three source calculations are shown in Figures 27 and 28. The equilibrium cavity pressures for the three calculations are 180 bars, 360 bars and 720 bars.

The cavity wall pressure history and representative pressure profiles for the nuclear source with no surrounding air, are shown in Figures 29 and 30. The equilibrium cavity pressure is 360 bars. A second nuclear source calculation with ambient air mixed in with the fireball gas was made and the wall pressure history is shown in Figure 31. The fireball and ambient gases were artificially pre-mixed since no radiation diffusion mechanism is presently available in the POD code. Artificially pre-mixing the gases gives the proper frequency of wall pressure pulses (Figure 31) and adjusting the initial size of the mixed

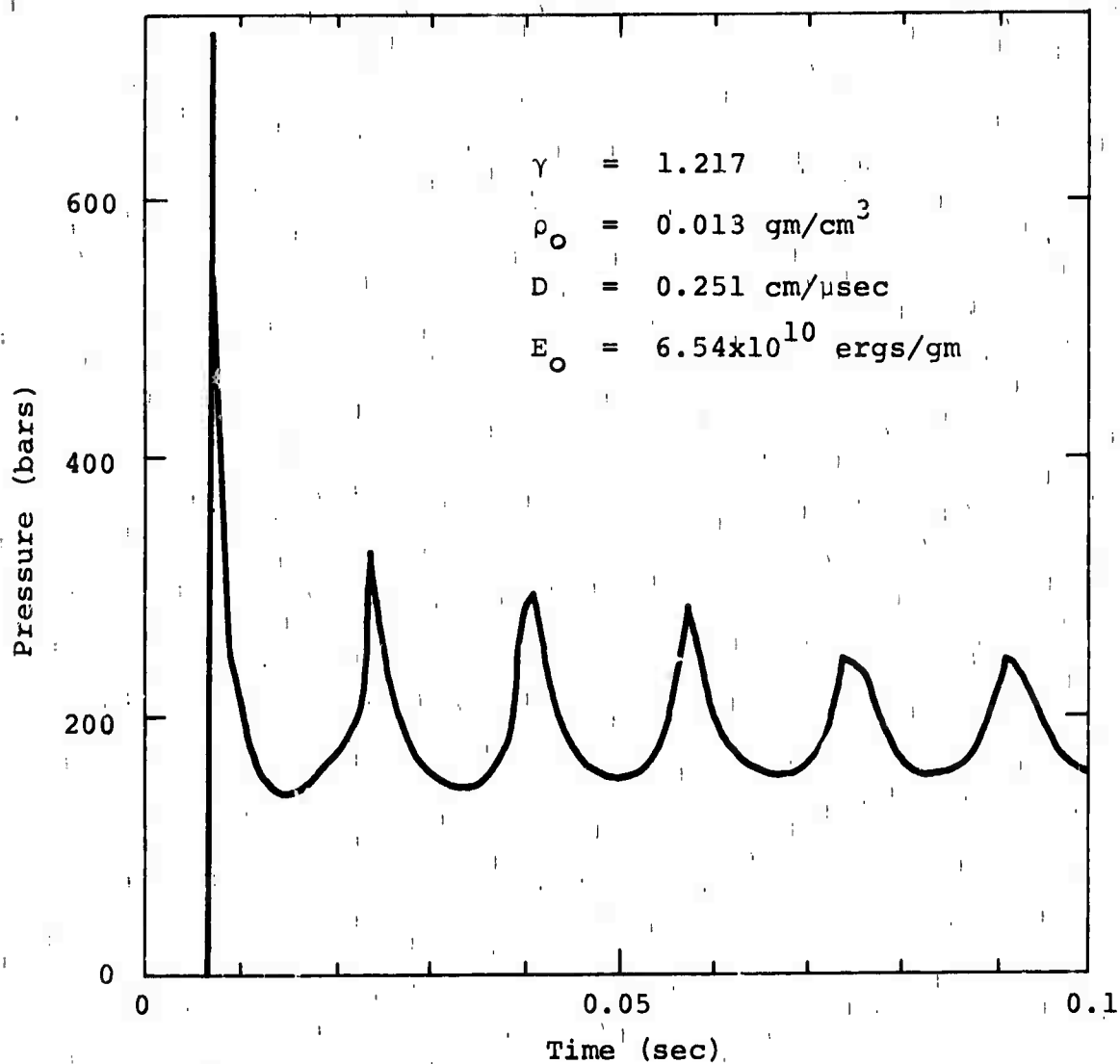


Figure 24 Cavity wall pressure history for cavity equilibrium pressure of 180 bars ($\text{CH}_4 + 1.50_2 + 1 \text{ atmos. air}$ at 300°K).

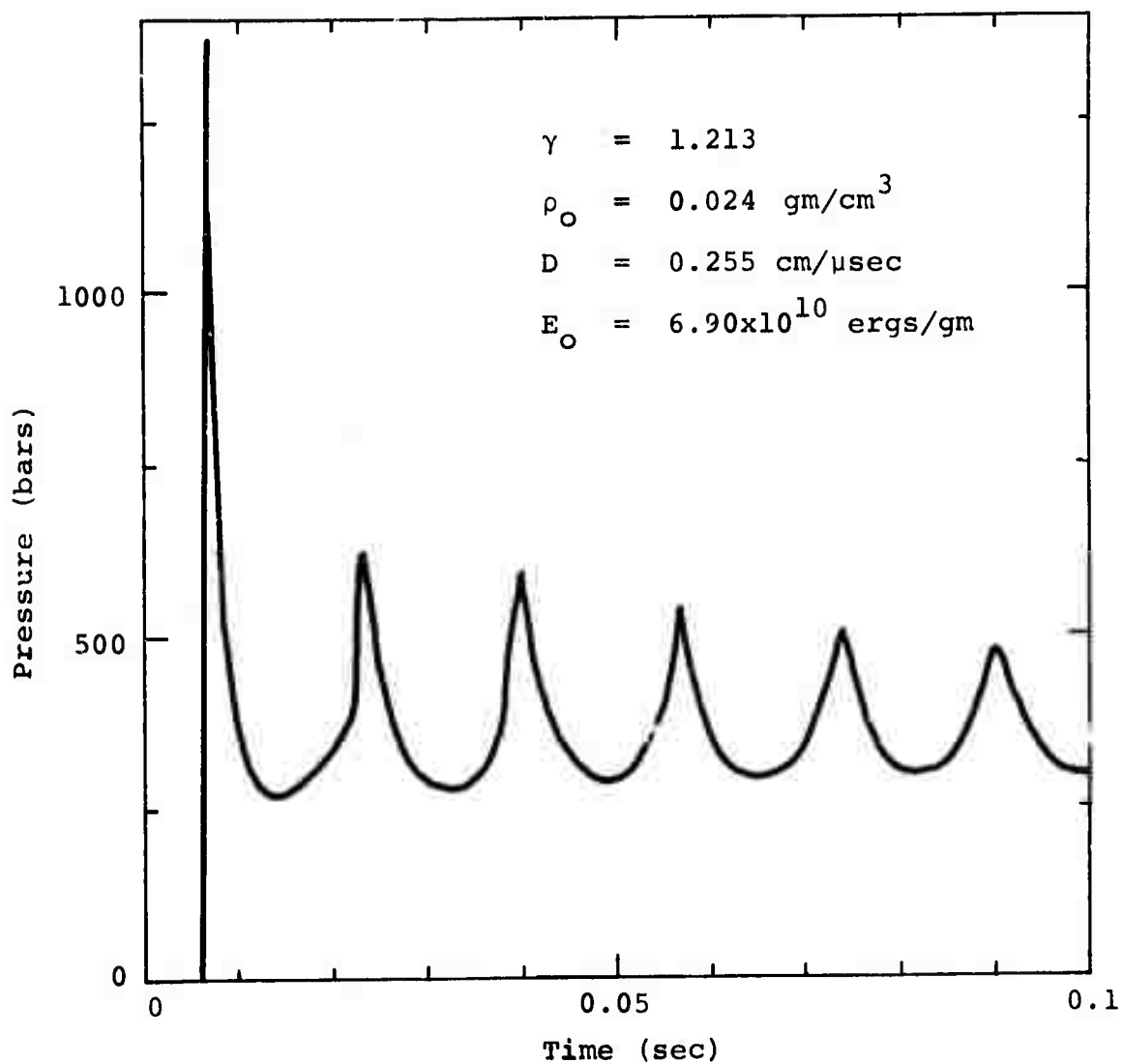


Figure 25 Cavity wall pressure history for cavity equilibrium pressure of 360 bars ($\text{CH}_4 + 1.5\text{O}_2 + 1 \text{ atmos. air}$ at 300°K).

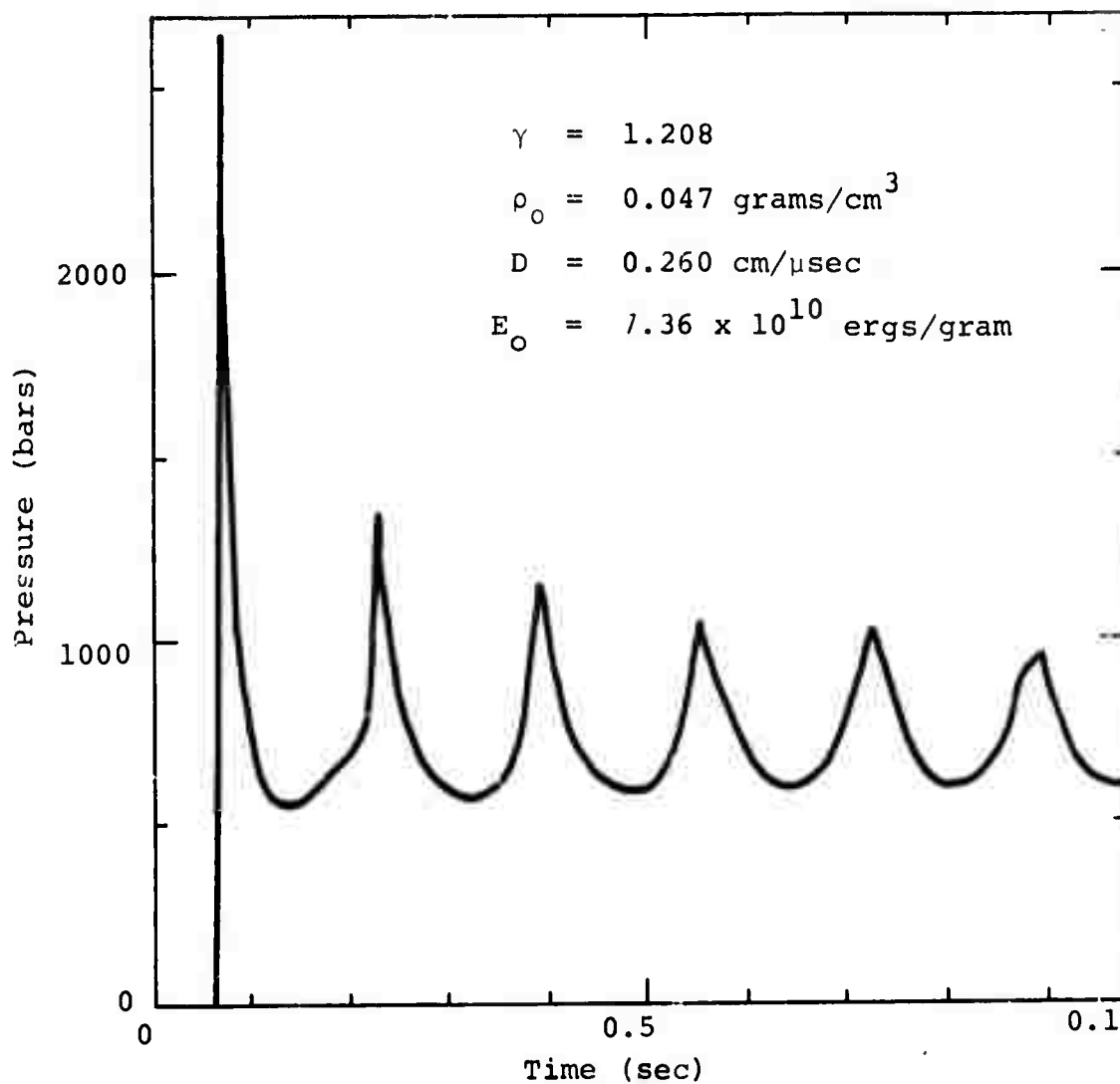


Figure 26 Cavity wall pressure history for cavity
 equilibrium pressure of 720 bars
 $(\text{CH}_4 + 1.5\text{O}_2 + 1 \text{ atmosphere air at } 300^\circ\text{K})$.

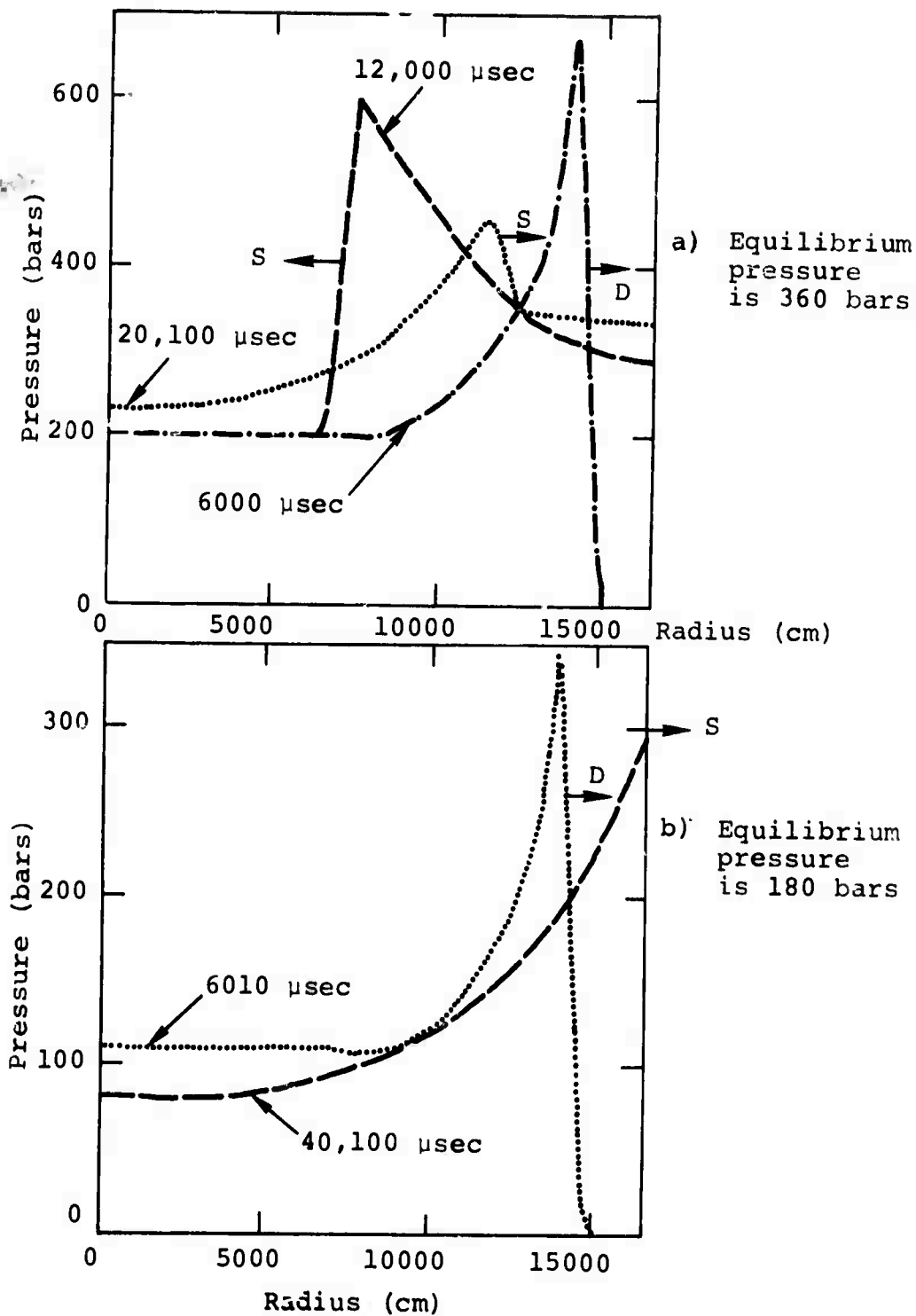


Figure 27 Selected pressure profiles for gas source calculations.

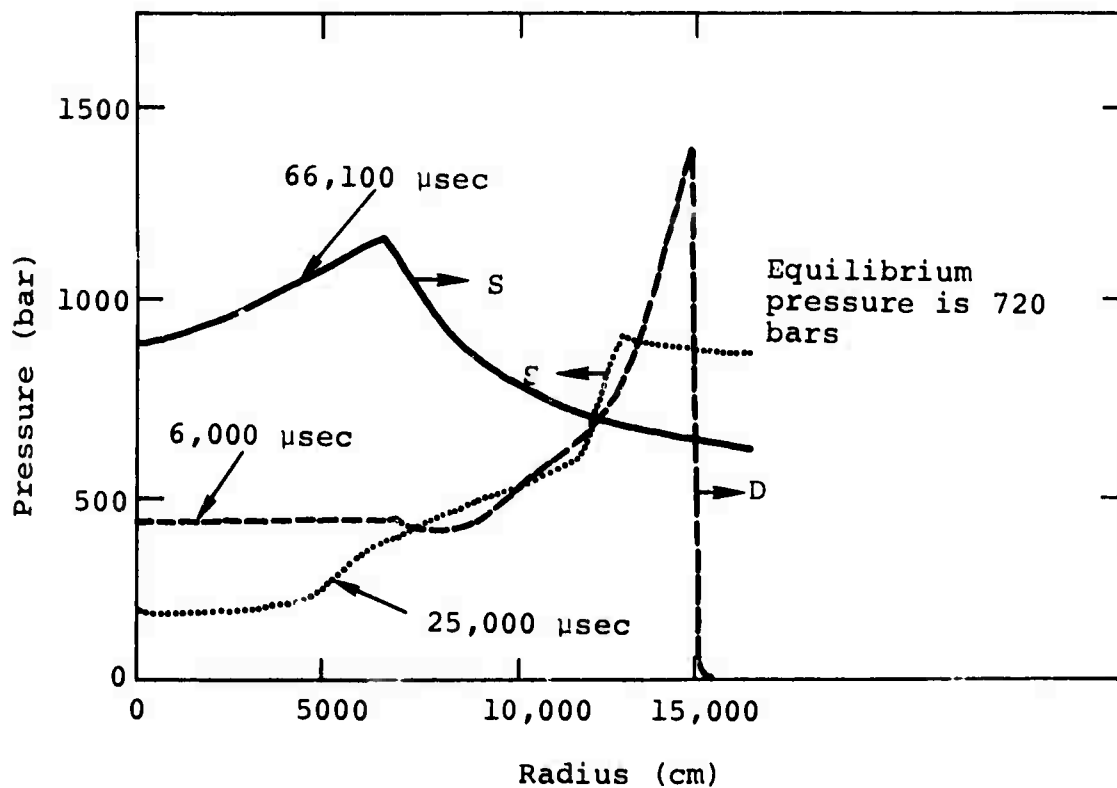


Figure 28 Selected pressure profiles for the gas source calculations.

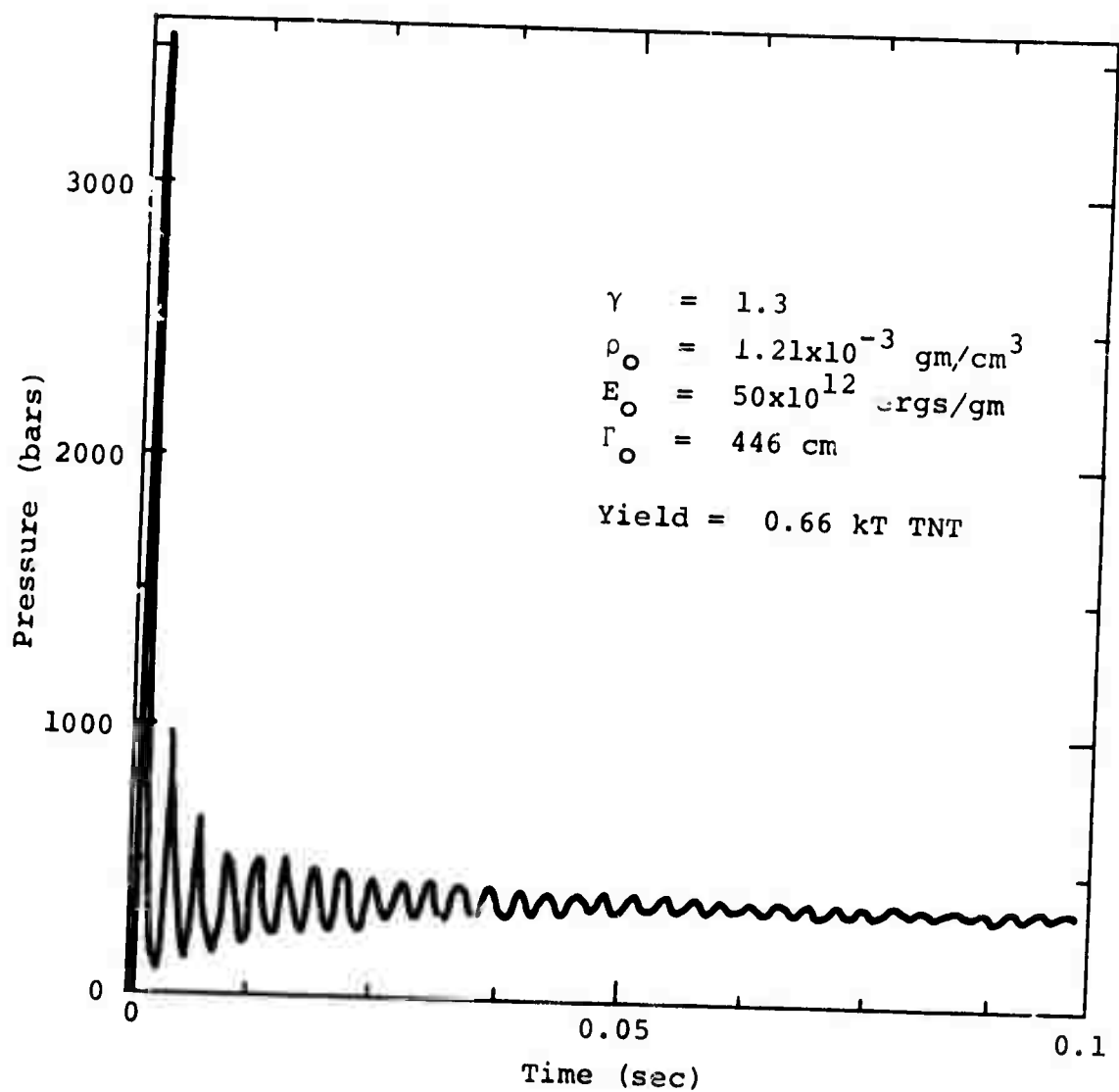


Figure 29 Cavity wall pressure history for cavity equilibrium pressure of 360 bars (nuclear source with no surrounding air).

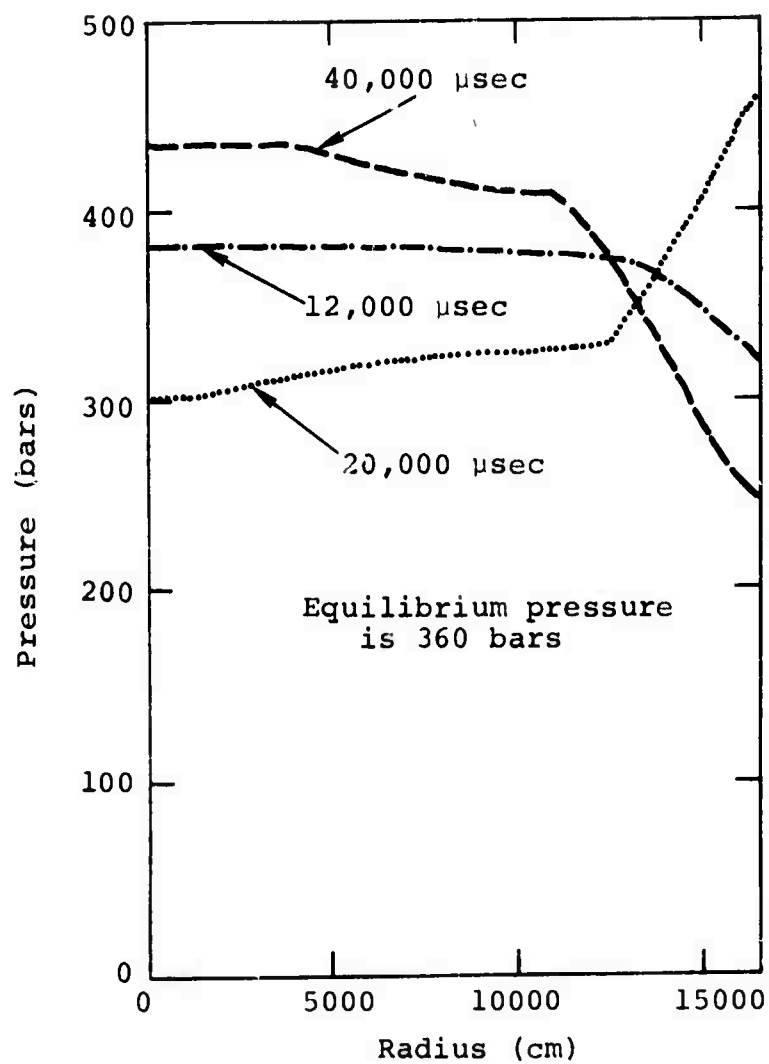
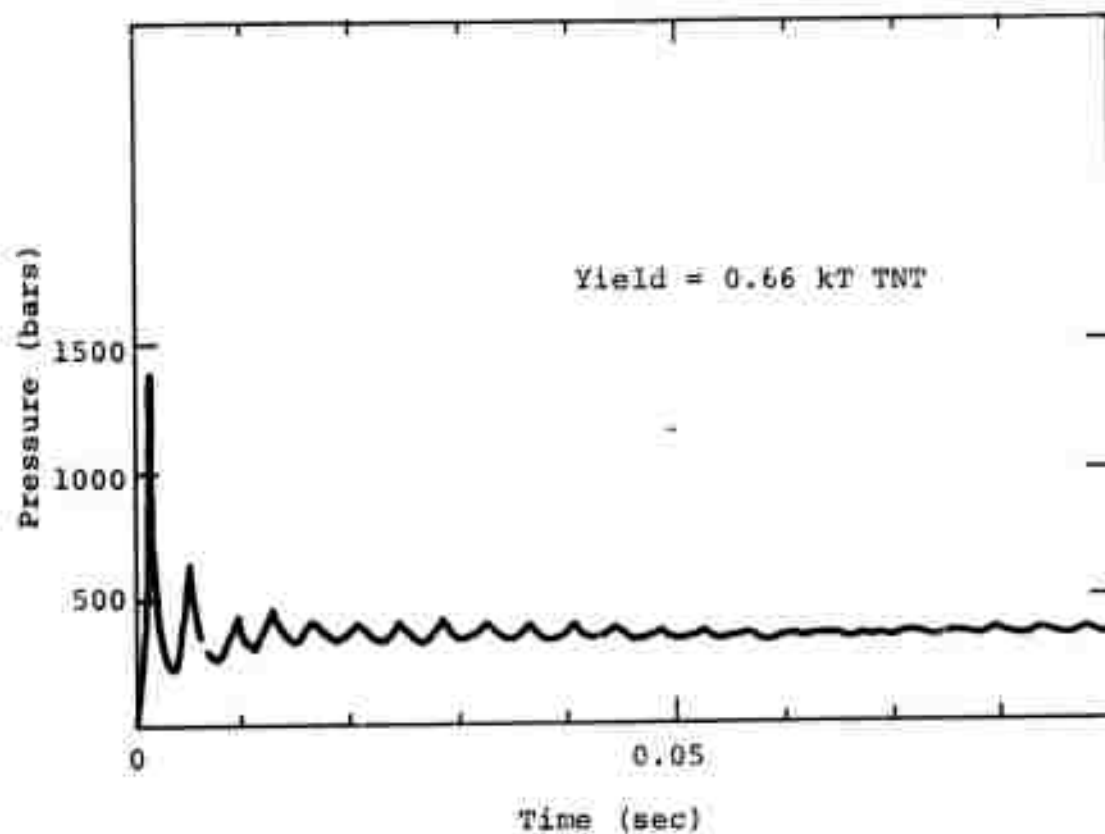


Figure 30 Selected pressure profiles for the nuclear source calculation.



Fireball $\gamma = 1.3$
 $\rho_0 = 0.335 \text{ gm/cm}^3$
 $E_0 = 11 \times 10^{11} \text{ ergs/gm}$
 $r_0 = 253 \text{ cm}$

Figure 31 Cavity wall pressure history for cavity equilibrium pressure of 360 bars (nuclear source mixed with air in cavity).

fireball adjusts the size of the initial pressure peak measured at the wall. However, because of limitations of time and funds, the second nuclear calculation was never used to drive a salt calculation.

The frequency of pressure pulses in the detonating gas calculations is in good agreement with the predicted gas dynamics of the MIRACLE PLAY series (Reference 14), however the nuclear source calculation, with no air, shows a considerably higher frequency of pressure pulses than shown in Reference 14. The second nuclear source calculation with mixed fireball and ambient gases, exhibits a frequency of wall pressure pulses more in agreement with those predicted for the STERLING event (Reference 14).

Representative results of the salt calculations are shown in Figures 32 through 44. Radial and tangential stress histories at 13176 cm or 8 cavity radii are shown in Figure 32 for the case of a linear equation of state, 180 bar overburden, Mohr-Coulomb yield and 360 bar cavity equilibrium pressure. The character of these histories reflect the pulsed character of the source pressure history. However, the character of the salt response changes significantly when the overburden is omitted (for the case of Mohr-Coulomb yielding) and changed even more so when a compaction equation of state is used (Figure 33). As would be expected, the overburden suppresses extensive plastic yielding around the cavity and the hysteresis associated with the compaction equation of state modifies the wave speeds of the stress waves and relief waves tending to cause successive pulses to coalesce. The effect of compaction is then to convert energy from the higher frequency modes to lower frequency modes. Increasing the overburden has the opposite effect of shifting energy to higher frequency modes.

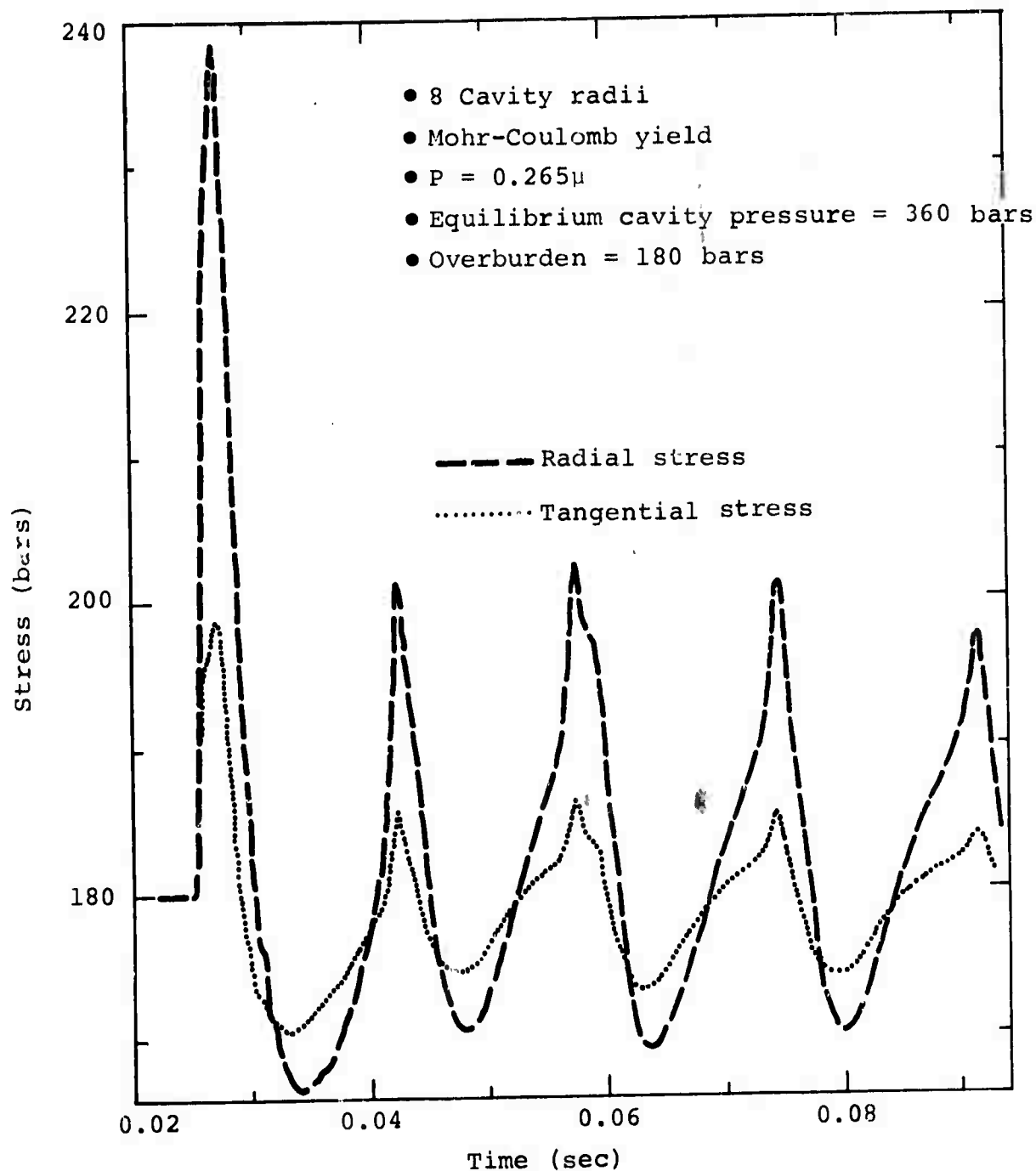


Figure 32 Typical calculated stress histories in the SALT from a gaseous detonation in a spherical cavity.

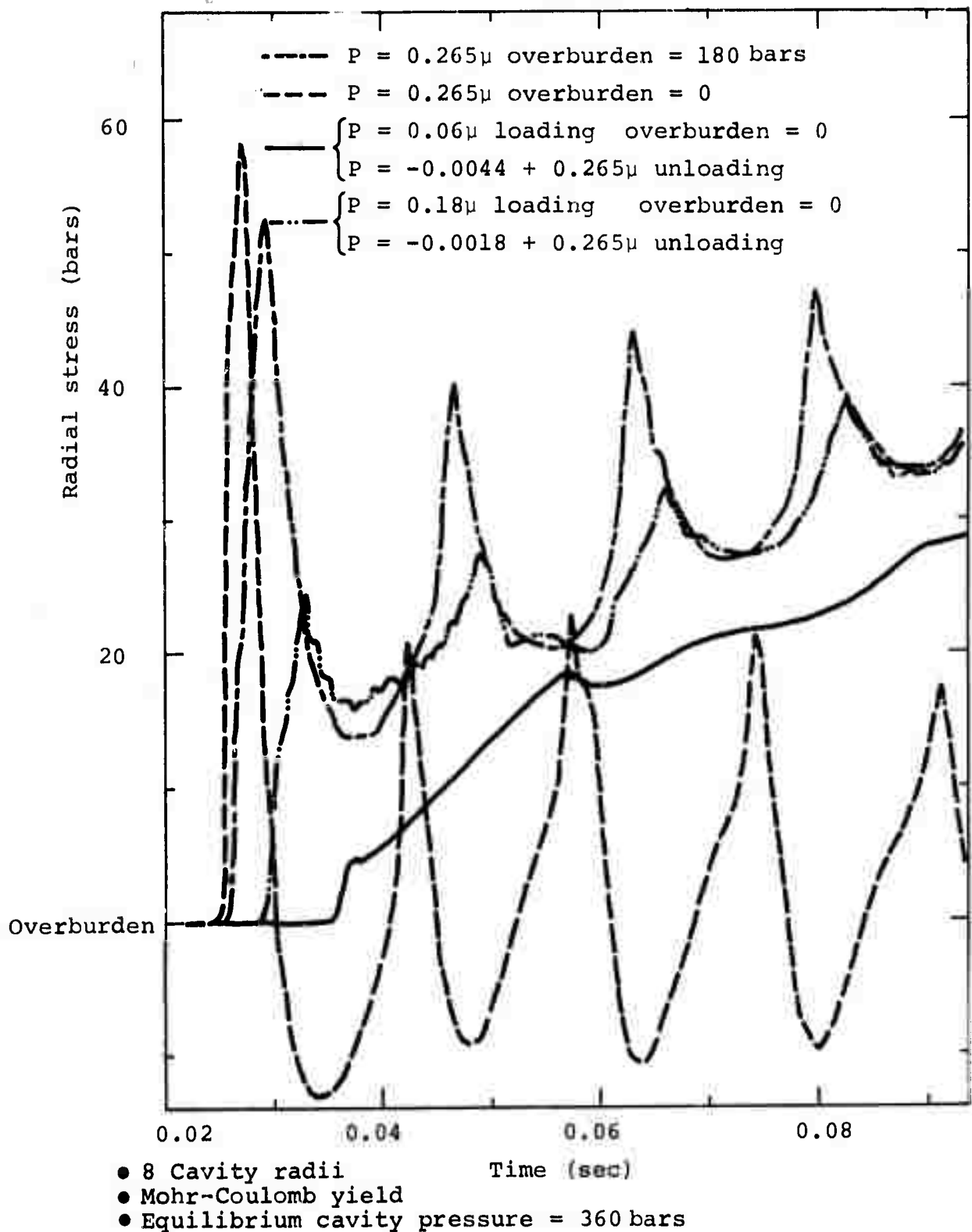


Figure 33 Typical radial stress histories showing the effects of overburden and compaction.

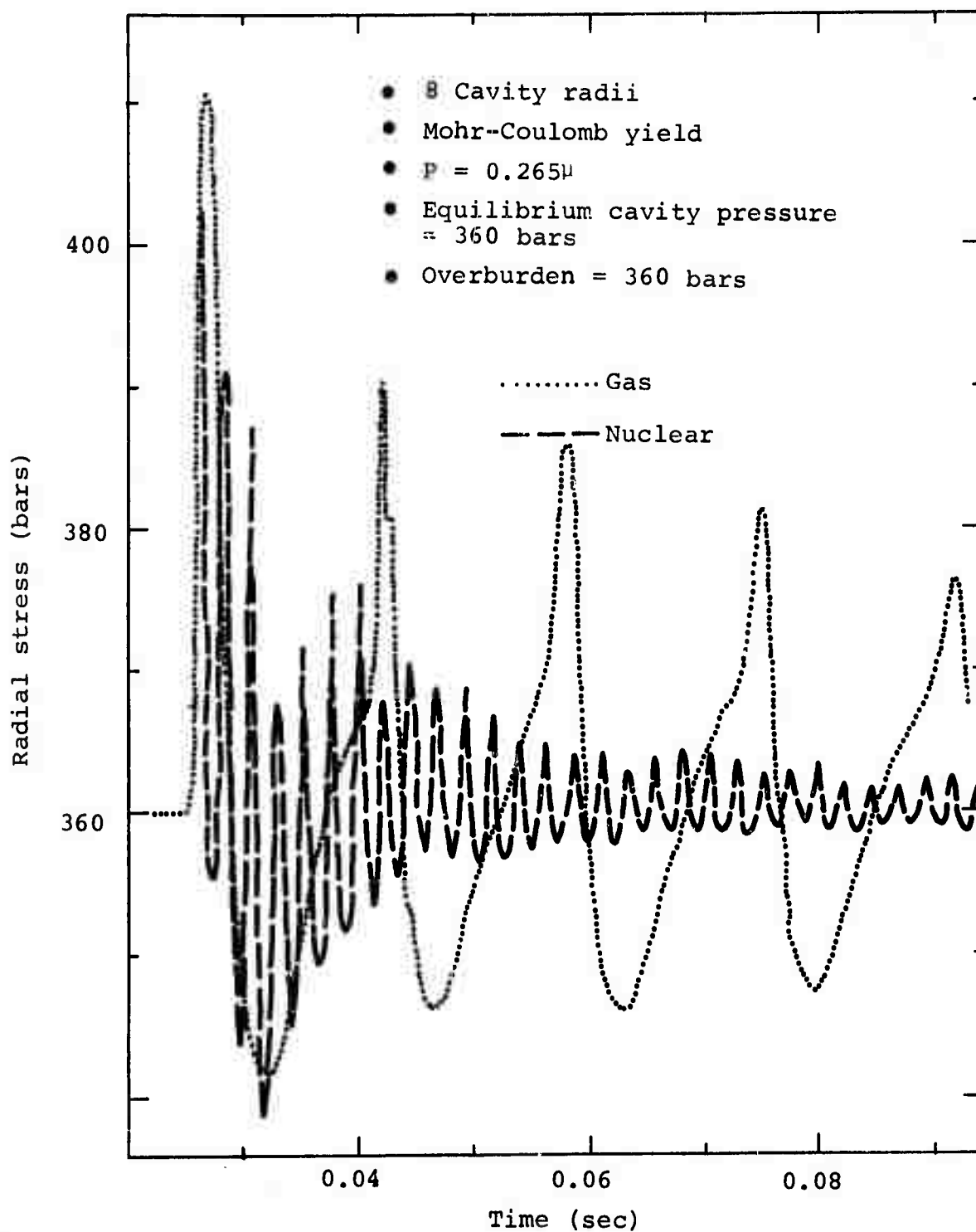


Figure 34 Typical radial stress histories for gas and nuclear sources.

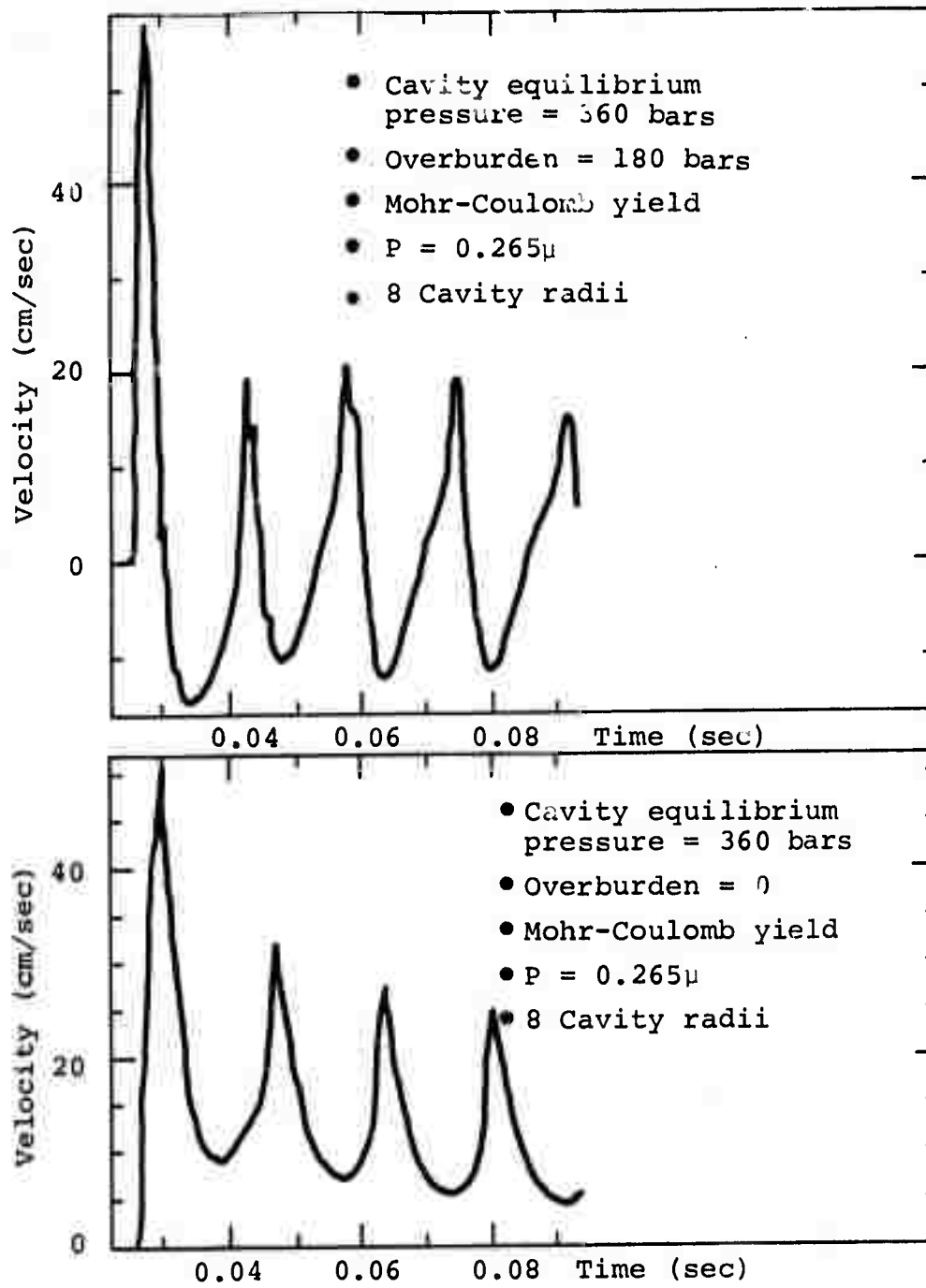


Figure 35 Velocity histories showing the effect of overburden.

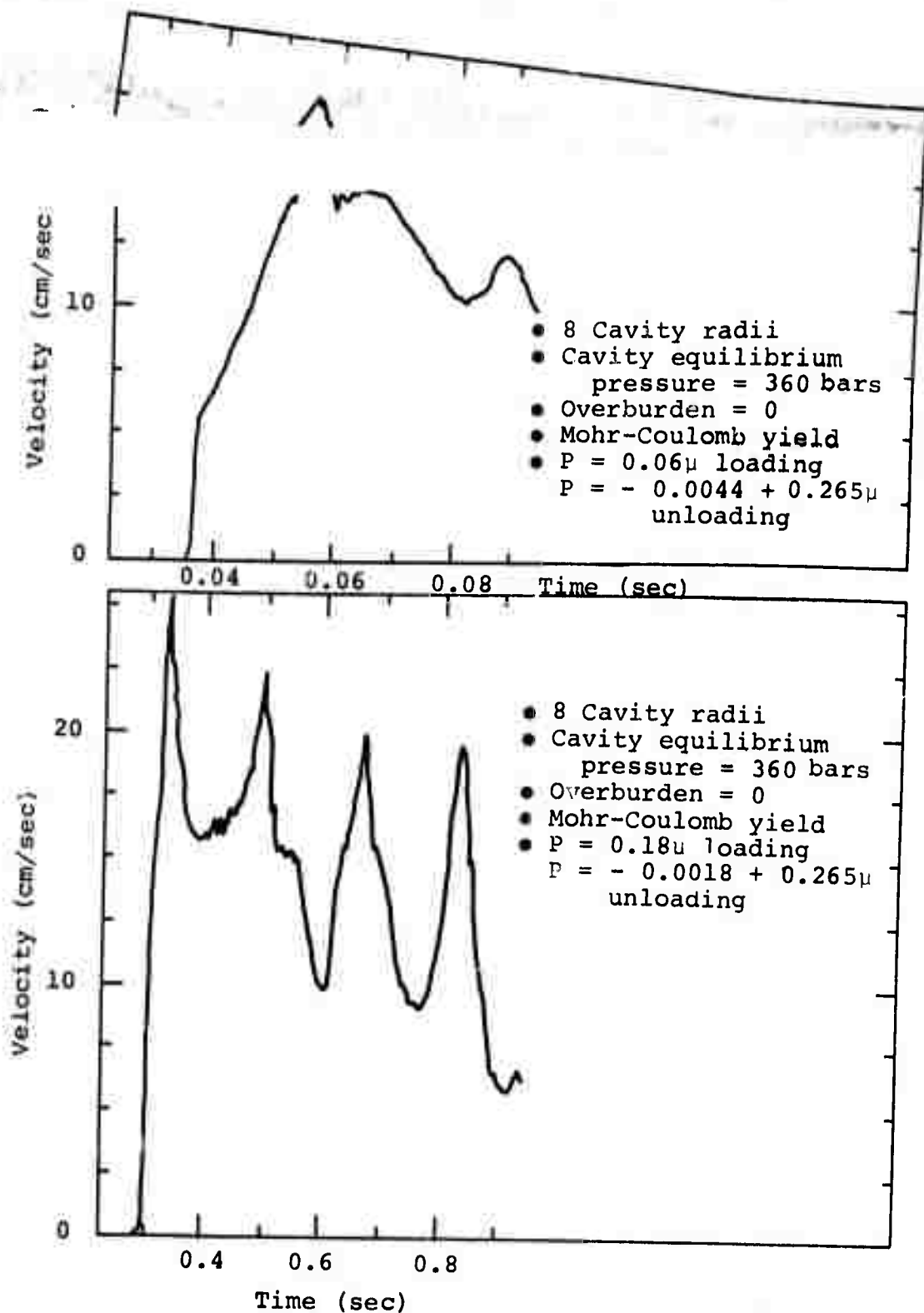


Figure 36 Velocity histories showing the effect of compaction.

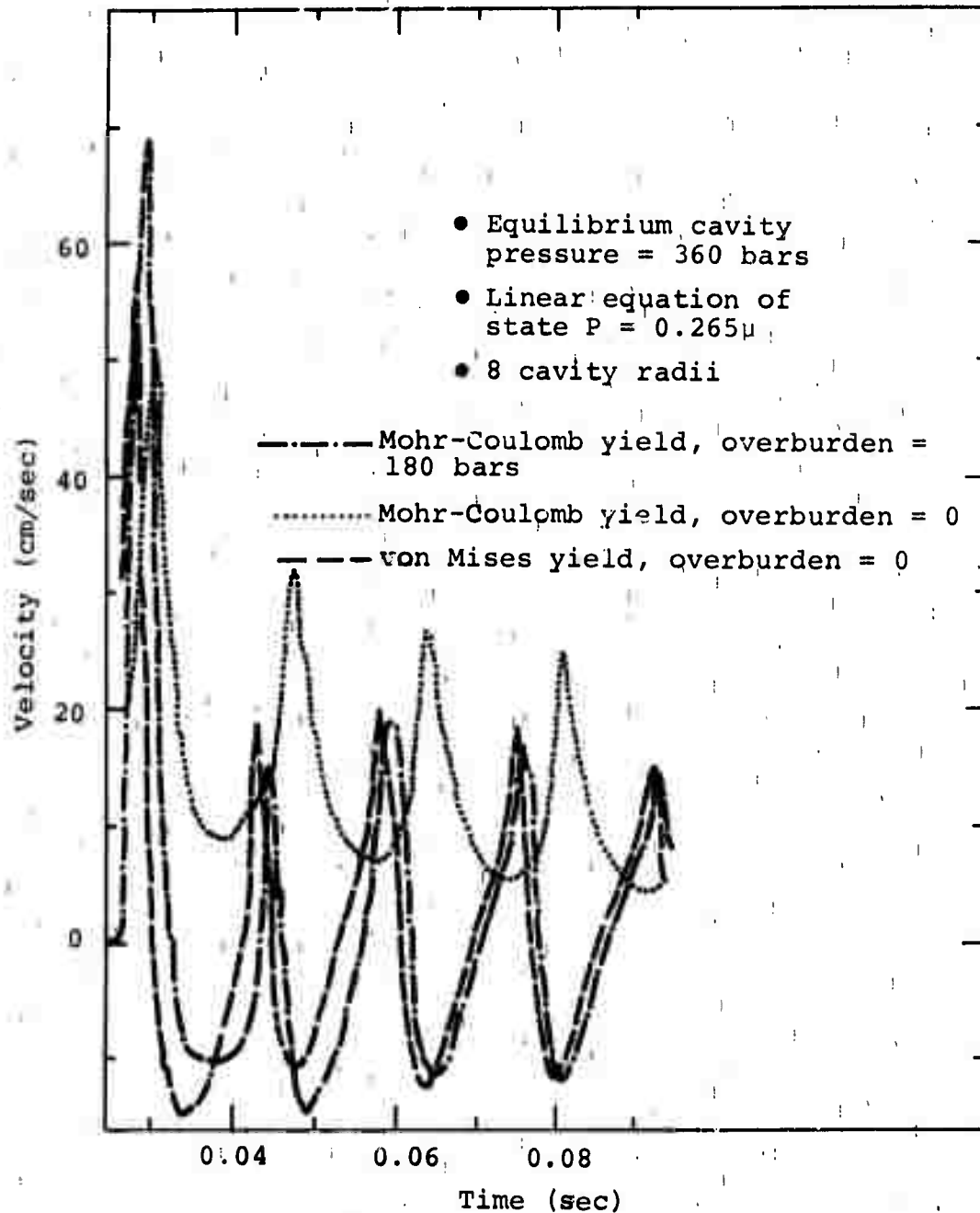


Figure 37 Velocity histories showing the effect of overburden and yield model.

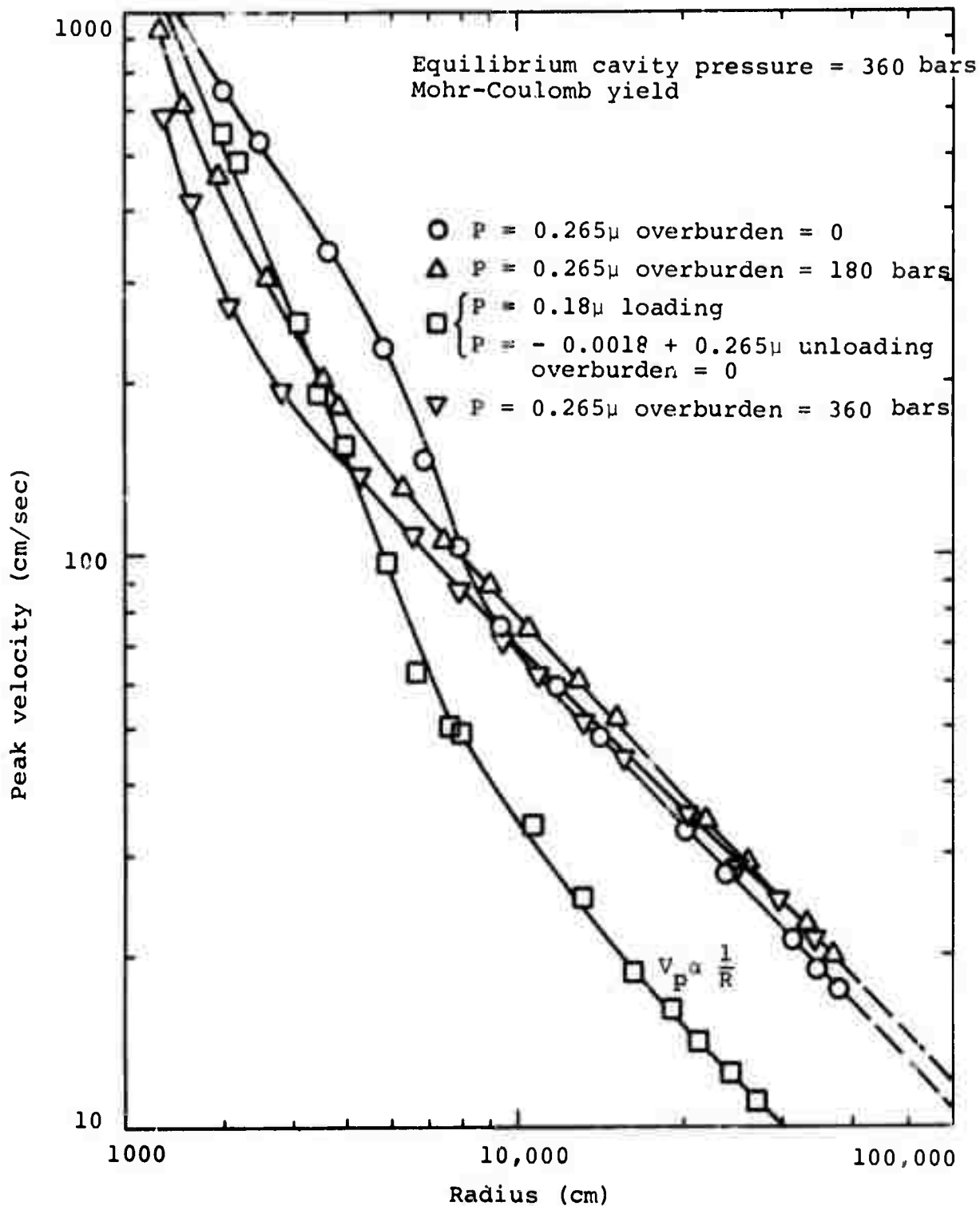


Figure 38 Peak particle velocity as a function of radius showing the effect of compaction and overburden.

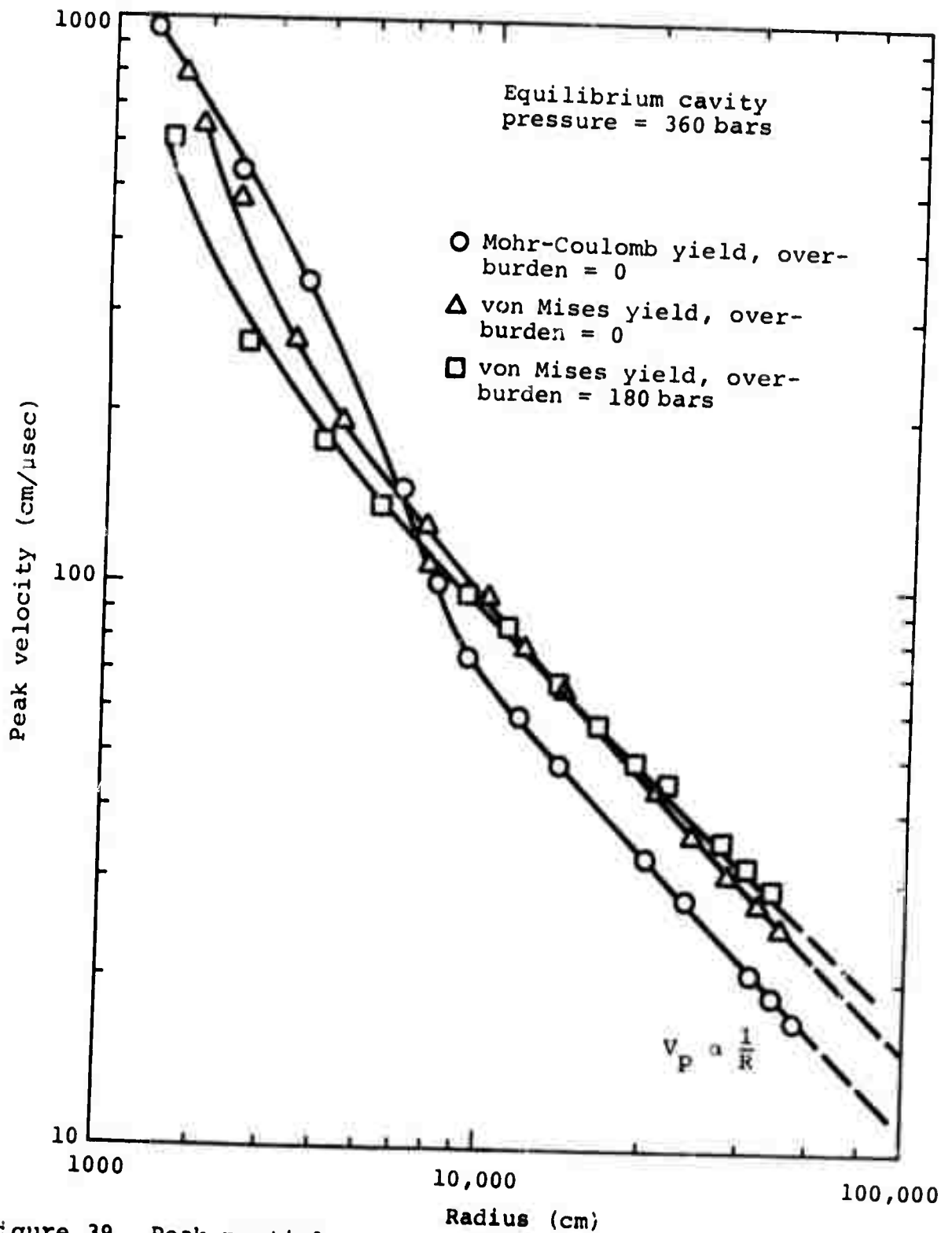


Figure 39 Peak particle velocity as a function of radius showing the effect of yield model and overburden.

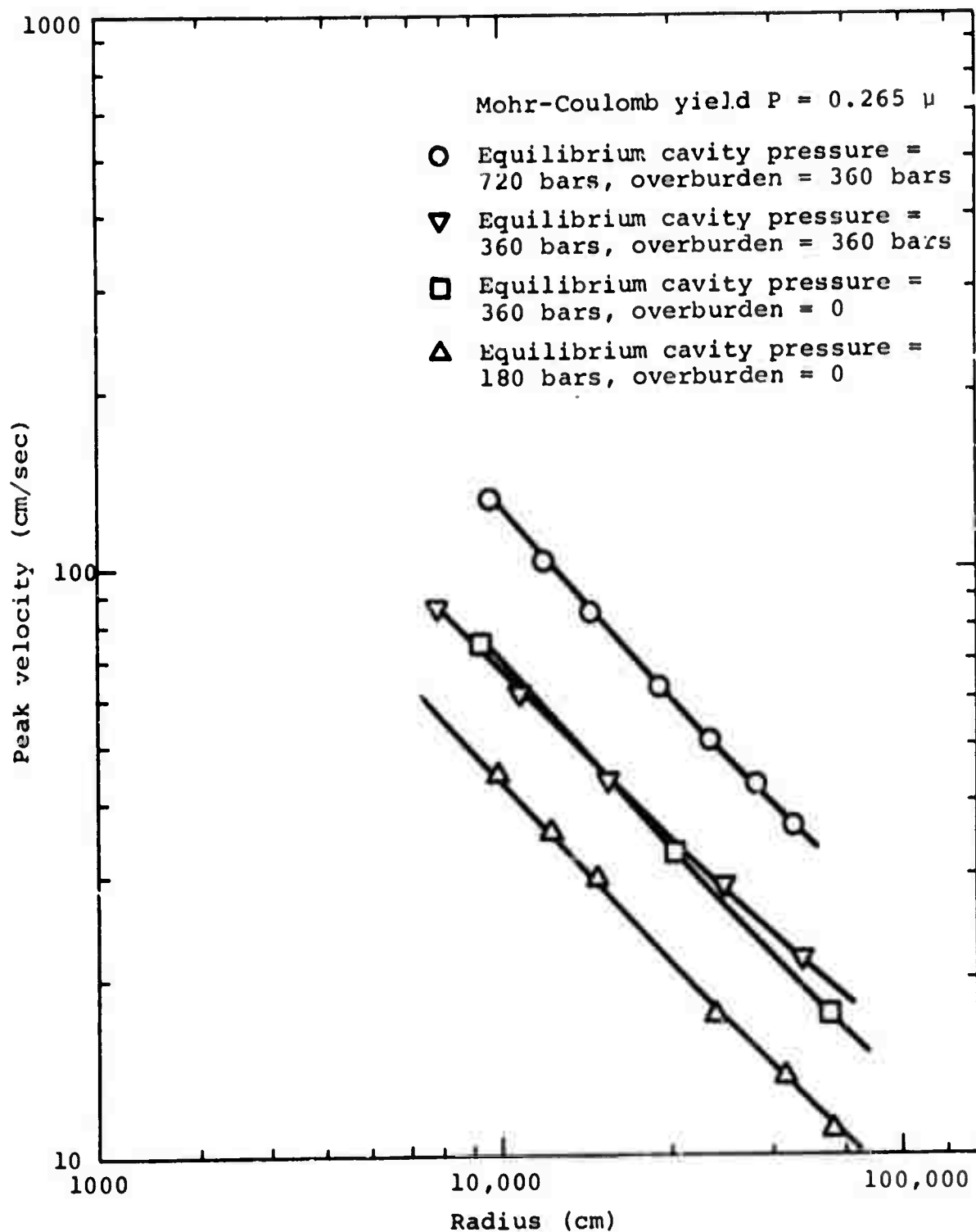


Figure 40 Peak particle velocity as a function of radius showing the effect of cavity equilibrium pressure.

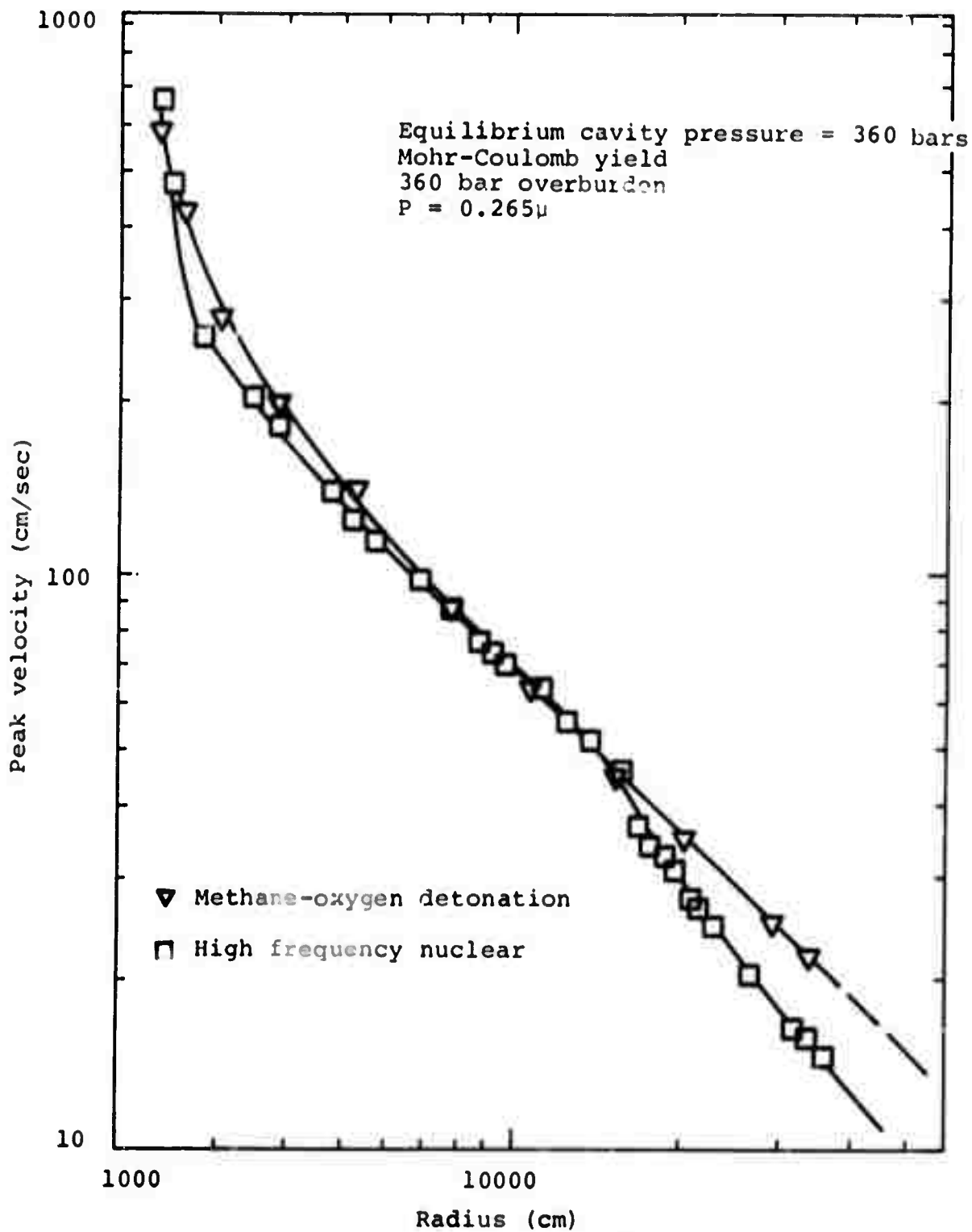


Figure 41 Peak particle velocity as a function of radius for nuclear and gas explosions.

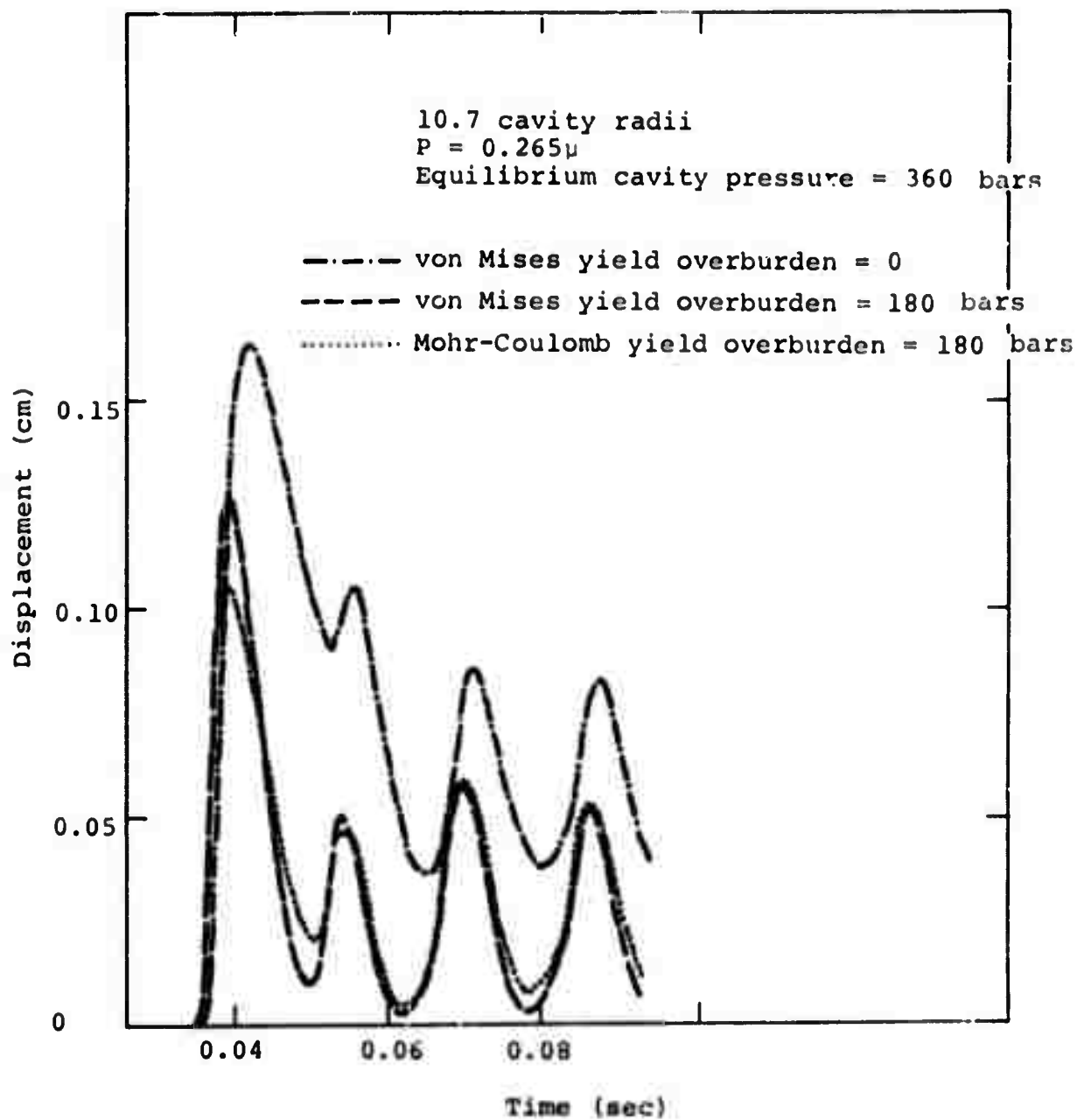
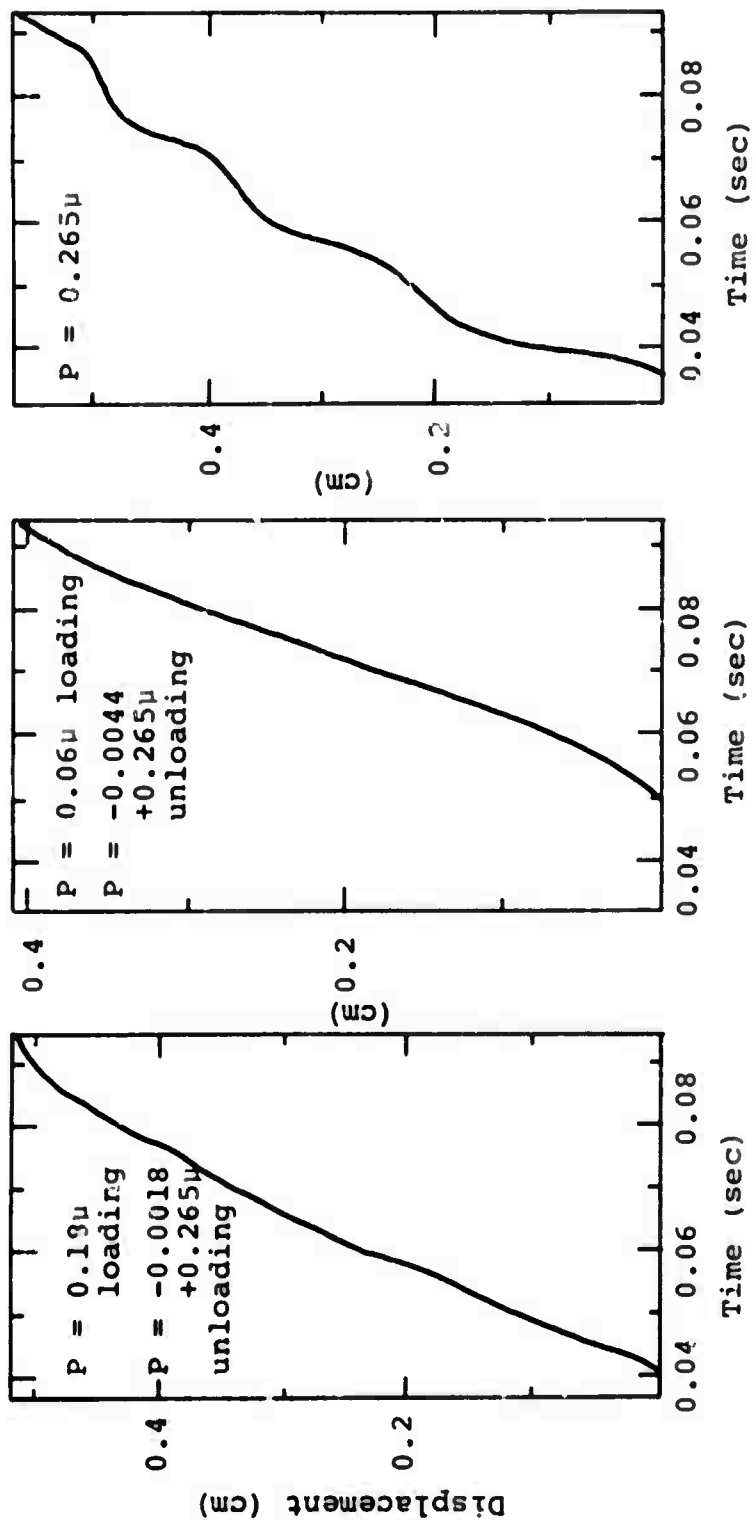


Figure 42 Displacement histories showing the effect of yield model and overburden.



10.7 Cavity radii
 Mohr-Coulomb yield
 Equilibrium cavity pressure = 360 bars
 Overburden = 0

Figure 43 Displacement histories showing the effects of compaction.

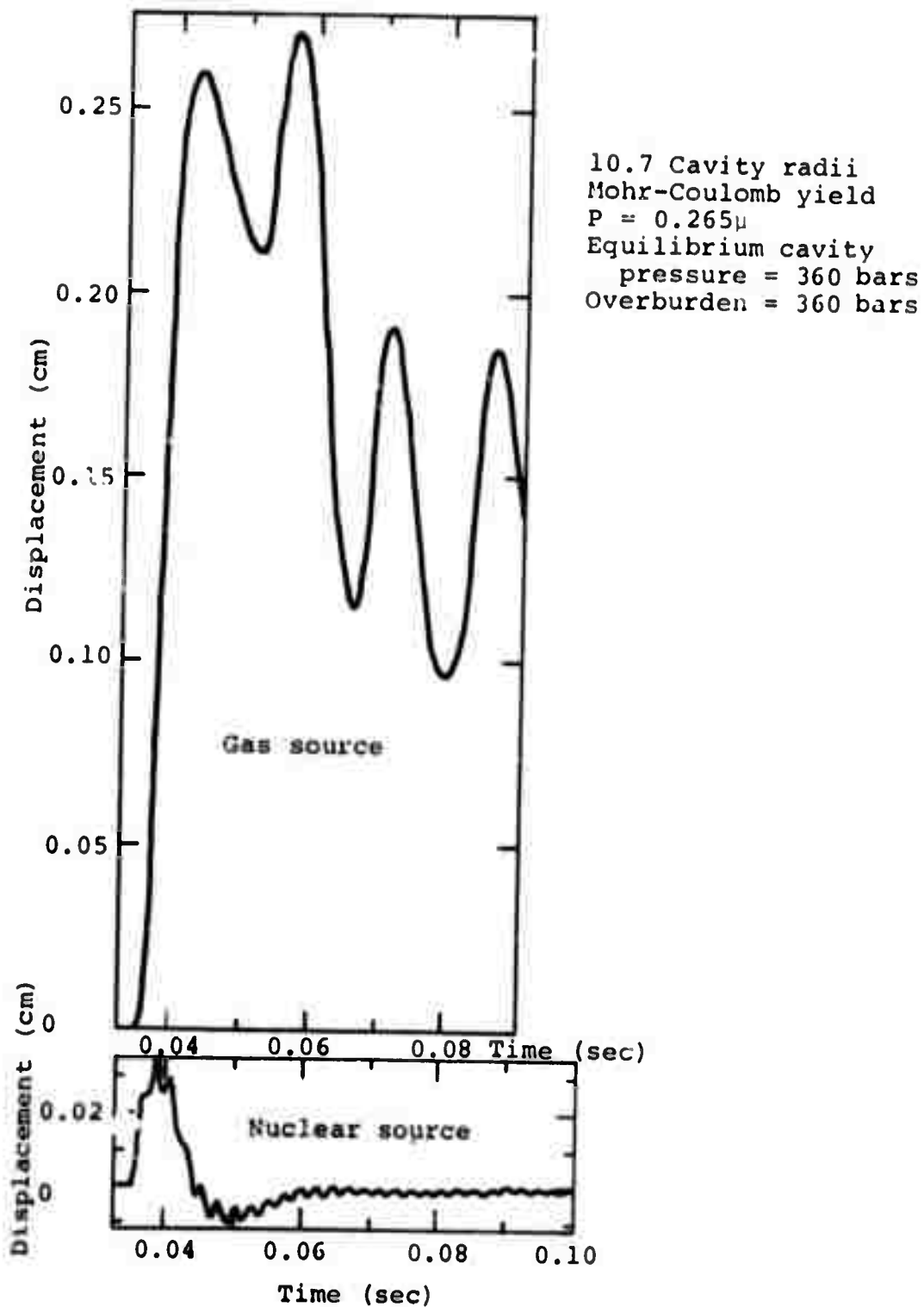


Figure 44 Displacement histories for gas and nuclear source.

The fundamental cavity frequency, calculated assuming a cavity in an infinite elastic media is given by:

$$\omega^* = \frac{1}{\pi} \frac{(1 - 2\nu)^{\frac{1}{2}}}{1 - \nu} \frac{C_L}{R} = \frac{C_S}{\pi R} \text{ (cps)}$$

where

ν = Poisson's ratio

C_L = longitudinal sound speed

R = cavity radius

C_S = shear wave velocity

For the linear equation of state salt used in the calculations:

$$\nu = 0.2713$$

$$C_L = 0.4510 \text{ cm}/\mu\text{sec}$$

$$R = 1647 \text{ cm}$$

$$\omega^* = 48.8 \text{ cps}$$

The cavity "ringing" is highly damped because of elastic energy radiating away and spherical divergence. However, the ringing can be seen clearly in the stress history in the salt driven by the high frequency nuclear source (Figure 34). Although a Mohr-Coulomb yield model was used, there was sufficient overburden to suppress most of the plastic yielding so that the cavity ringing can clearly be seen. It is less obvious in the equivalent gas calculation primarily because the frequency of pressure pulses (62 cps) is very close to the natural cavity frequency. However, as will be described later the fundamental cavity frequency can be seen unmistakably in the response spectra.

Selected particle velocity histories also at 8 cavity radii (13176 cm) are shown in Figures 35, 36 and 37. Figure 35 portrays the effect of overburden with a Mohr-Coulomb yield model and

Figure 36 shows the effect of varying the degree of compaction. A comparison of yield models is presented in Figure 37, where it is seen that the particle velocity for the case of Von-Mises yield with no overburden is very similar to that of Mohr-Coulomb yield with overburden. Yielding occurs at much lower stresses with the Mohr-Coulomb model and is suppressed when overburden is included. Particle velocity histories for the other one-dimensional salt calculations are given in Appendix D.

Plots of peak particle velocity as a function of radius are given in Figures 39 through 41. As expected the peak particle velocity is inversely proportional to radius when the wave is elastic. In all cases the extent of plastic yielding was well within the LEEK interface at 17,647 cm (10.7 cavity radii). The variation of peak velocity near the source is more complicated because of yielding and compaction. A close examination of these plots shows the filtering effects of compaction and yielding. For example, a compactible equation of state results in reduction in peak velocity by a factor of approximately 2.3 (Figure 38) while extensive Mohr-Coulomb yielding reduces peak velocity by a factor of about 1.4 (Figure 39) over that of simple Von Mises yielding. Doubling the cavity equilibrium pressure with and without overburden increases the peak velocity by a factor of approximately 1.6 (Figure 40). As will be discussed later, the maximum displacement and low frequency response spectrum is increased and the peak particle velocity is decreased when the media yields and/or is compacted.

Figure 41 compares the peak particle velocity versus radius behavior for a gas and nuclear source. They are remarkably similar except for an anomalous dip in the peak velocity at

about 10 cavity radii from the nuclear source. It is suspected that this is a result of a loss in resolution of the tip of the very narrow spike of the stress wave. This anomalous dip would not have occurred if the zoning in the salt were finer.

Typical displacement histories at 10.7 cavity radii (17.647 cm) are shown in Figures 42, 43 and 44. These show the increased decoupling with increased overburden (Figure 42) and demonstrates the importance of including overburden in calculations or experiments of decoupling phenomena. In the case of no overburden and/or compaction (Figure 43), the displacement continues to increase at the termination of the calculation and suggests that such calculations if carried out to much longer times would demonstrate significant seismological effects of yield model and compaction model variation.

The comparison of displacement histories generated by gas and nuclear source (Figure 44), shows that the nuclear source, which was fully decoupled (almost no yielding near the cavity was observed) results in peak displacement nearly an order of magnitude less than that resulting from the gas source. Part of this may be due to a tendency of the cavity to resonate with the gaseous detonation pressure pulses as the two frequencies are very close (49 cps resonant frequency excited by 62 cps pressure pulses). This comparison demonstrates the importance of source frequency on decoupling behavior.

Several calculations were made to investigate the effects of modifying the zoning and Courant stability condition safety factor. With coarser zoning the wave fronts were spread out but not seriously. Coarser zoning would be quite adequate for

extended calculations where seismologically significant effects are being studied. Even the higher frequency components of the waves (several hundred cps) do not appear to be seriously affected by coarser zoning as will be shown in the spectral analysis given later. With a high Courant stability condition safety factor there is significant noise generated in the relief waves. This is caused by an increased interpolation error in the difference equations as a result of the larger time step. It is therefore felt that the advantage of reduced numerical dispersion of the stress wave gained by using a very high safety factor is outweighed by the excessive noise generated in the relief wave.

4.3 DATA ANALYSIS

The velocity histories monitored for all the calculations were subjected to a spectral analysis. The velocity histories were integrated to give displacement histories whereupon the displacement response spectra and Fourier amplitude spectra were calculated (see Figure 45 and Reference 12 for example). Examples of displacement response spectra are shown in Figure 46 where the highlights such as theoretical fundamental cavity frequency, source shock reverberation frequency and the spectral window (determined by pulse length and onset of zonal noise) are illustrated. Zonal noise appears to be noticeable in the spectra at 2,000 to 2,500 cps. The transit time for a sound wave across a single zone is $80 \text{ cm} / 0.4510 \text{ } \mu\text{sec} = 177 \text{ } \mu\text{sec}$, which corresponds to 5,650 cps, so the observed onset of noise appears to be related to 2 to 3 zone transit times. Approximately 8 higher modes of the fundamental shock reverberation frequency are resolvable before the onset of noise.

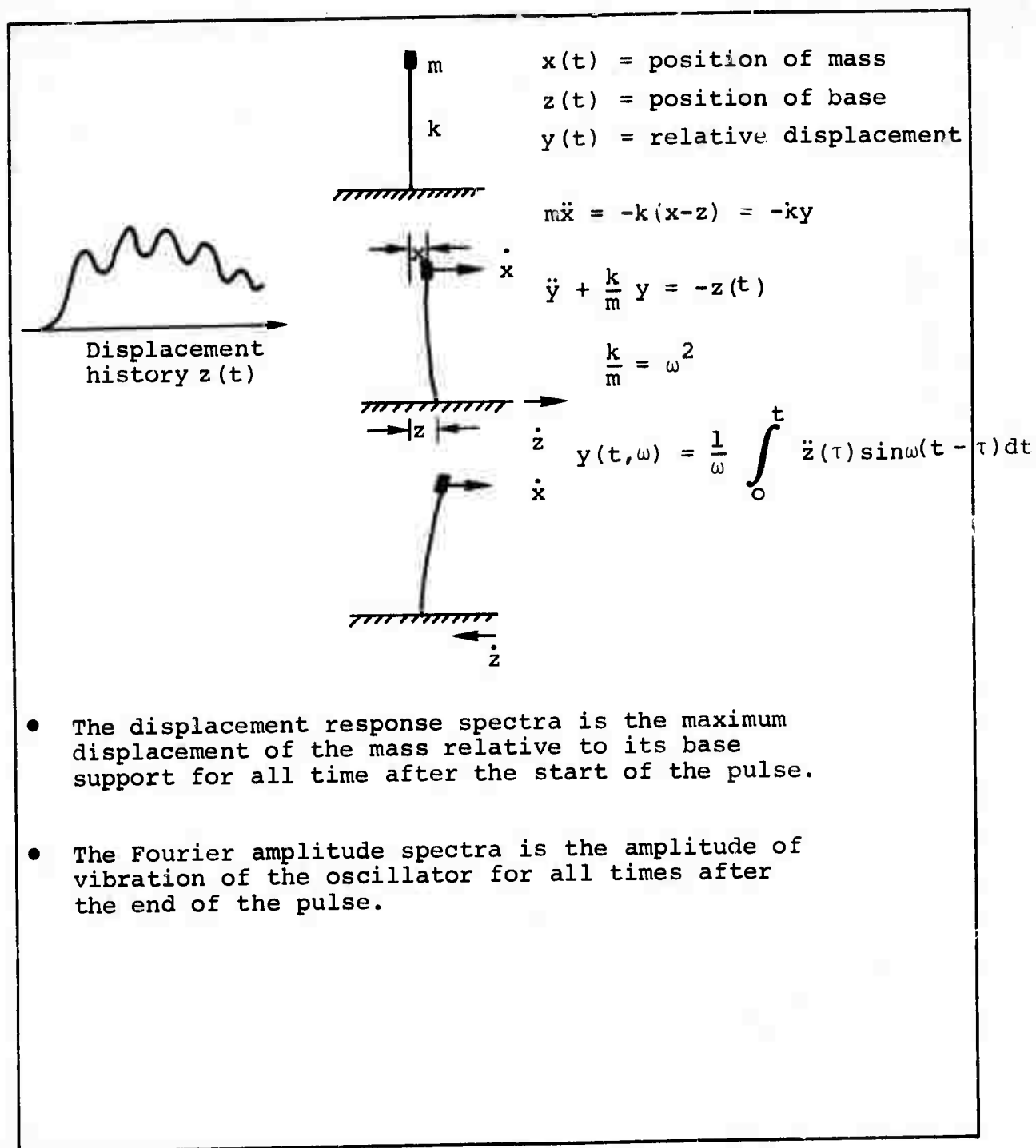


Figure 45 Mass-spring system used to determine the Fourier and response spectra.

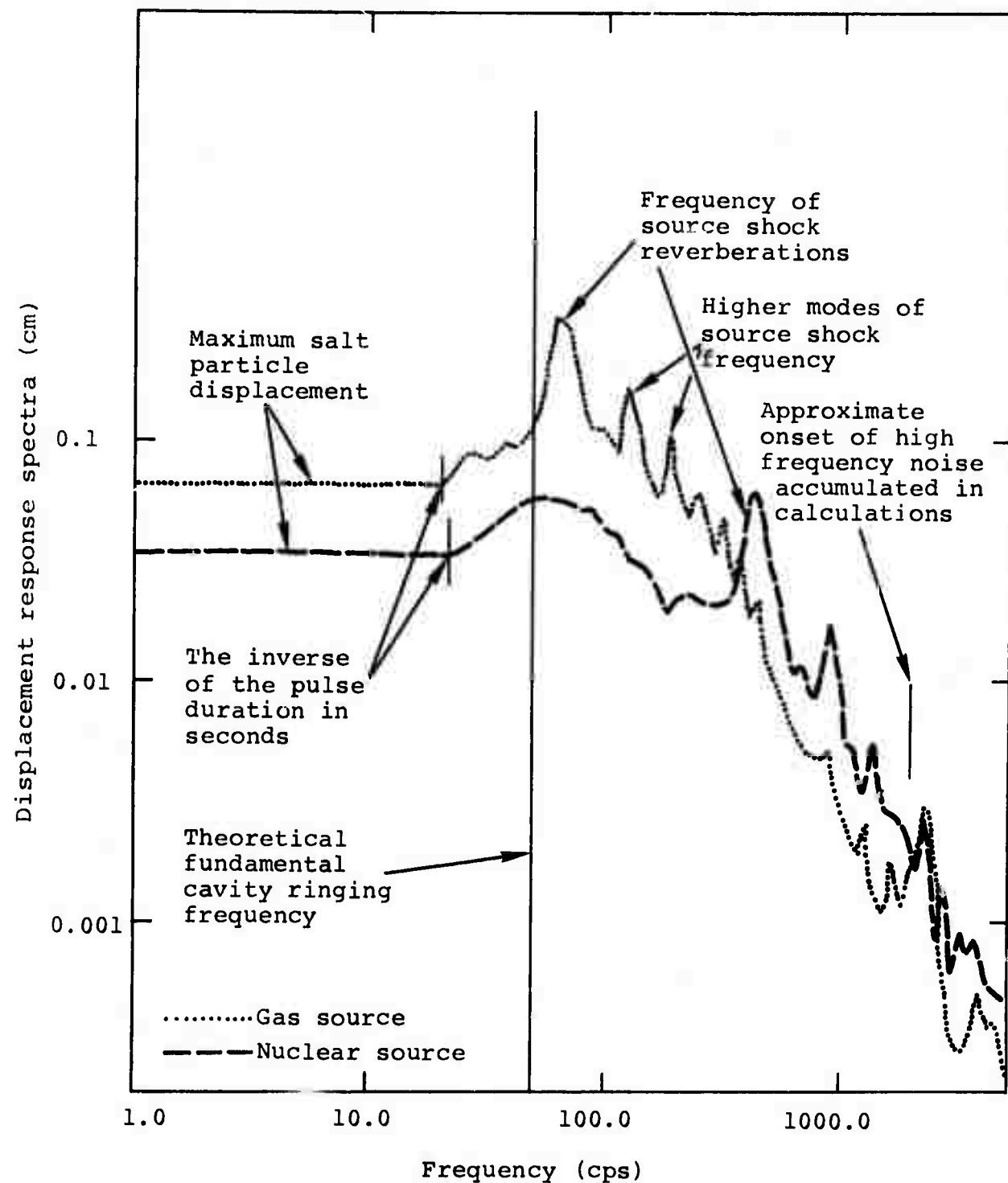


Figure 46 Structure of the displacement response spectra.

Figure 47 compares the response spectra of five 1/2 pulses with that of the first pulse only for a case with little yielding and no compaction. It is seen that the first pulse establishes the basic frame of the response spectra and determines the maximum displacement. Successive pulses build up the primary and higher order maxima and also excite some natural cavity resonance.

The salt response for the high frequency nuclear source is compared to that of the corresponding gas source in Figure 48 and it is seen that the spectrum, especially the low frequency portion, of the nuclear source is lower in amplitude (showing better decoupling). The pressure pulse frequency for the nuclear source is about 430 cps, while that of the gas source is 62 cps. The excitation of natural cavity resonance is clearly evident for the nuclear source and is readily apparent for the gas source.

The effect of radius on the response spectra is shown in Figure 49 for a case with little yielding and no compaction and all but the higher frequency content seems to scale as expected.

The effect of varying overburden with a Mohr-Coulomb yield model is shown in the response spectra of Figure 50. Increasing the overburden clearly suppresses the peak displacement ($\omega = 0$). The amplitude of the fundamental shock reverberation frequency (~ 62 cps) increases with overburden. As the overburden is removed more plastic yielding can occur and energy shifts from higher frequency to lower frequency modes.

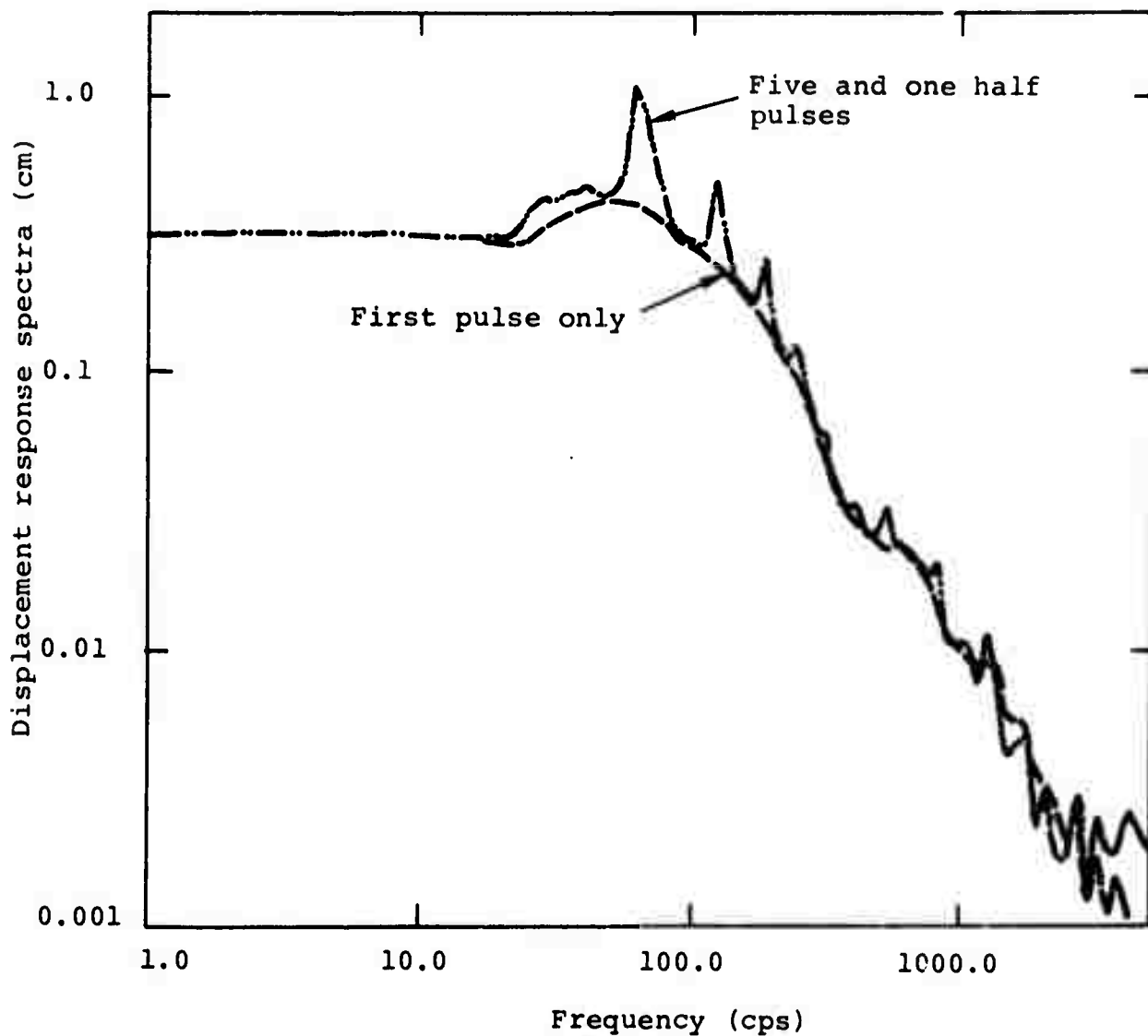


Figure 47 Response spectra for the first pulse and for the first five and one half pulses calculated for an equilibrium cavity pressure of 360 bars, overburden of 180 bars, Mohr Coulomb yield at 4 cavity radii.

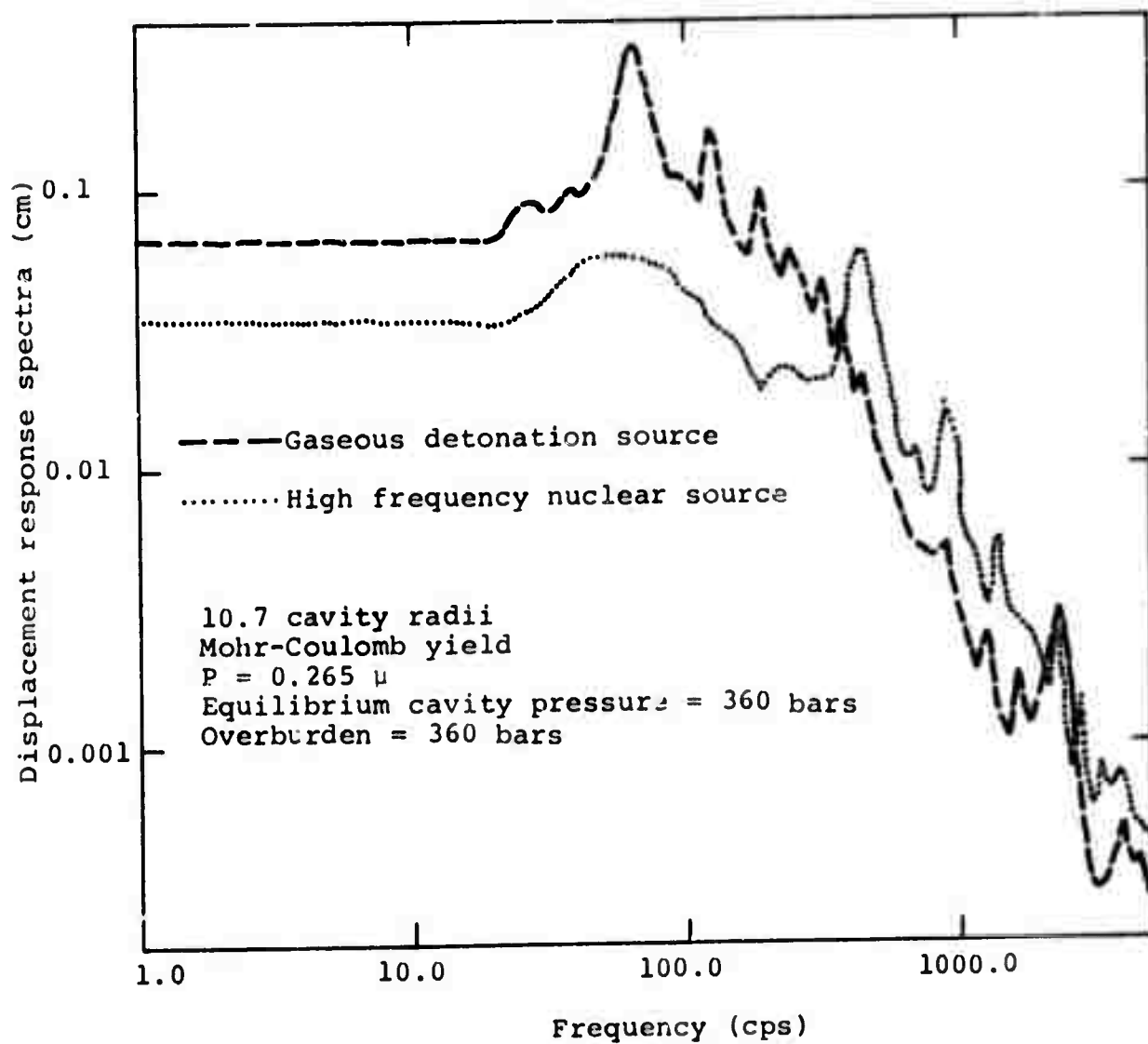


Figure 48 Displacement response spectra showing the effect of source frequency.

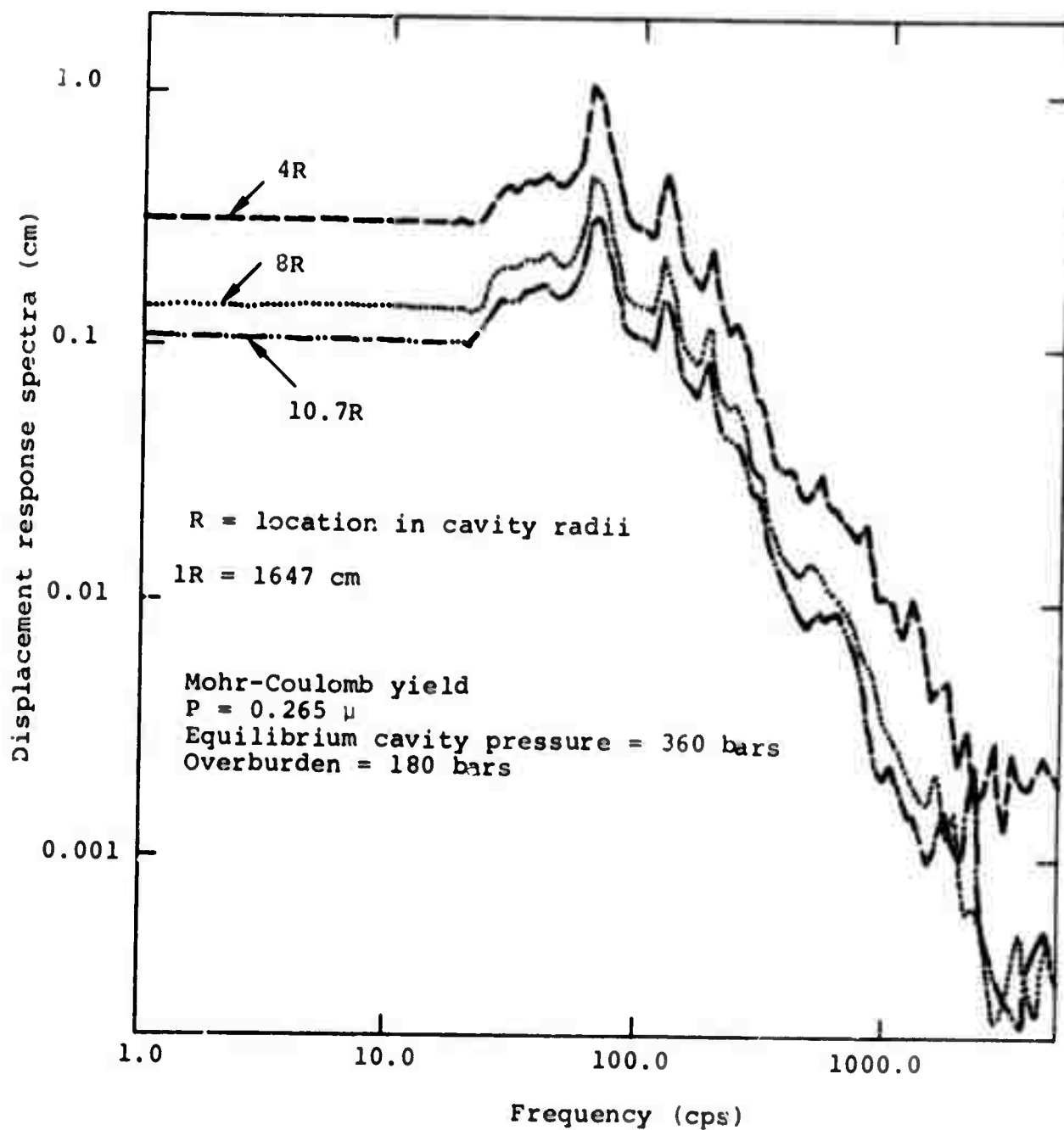


Figure 49 Displacement response spectra showing the effect of distance from the source.

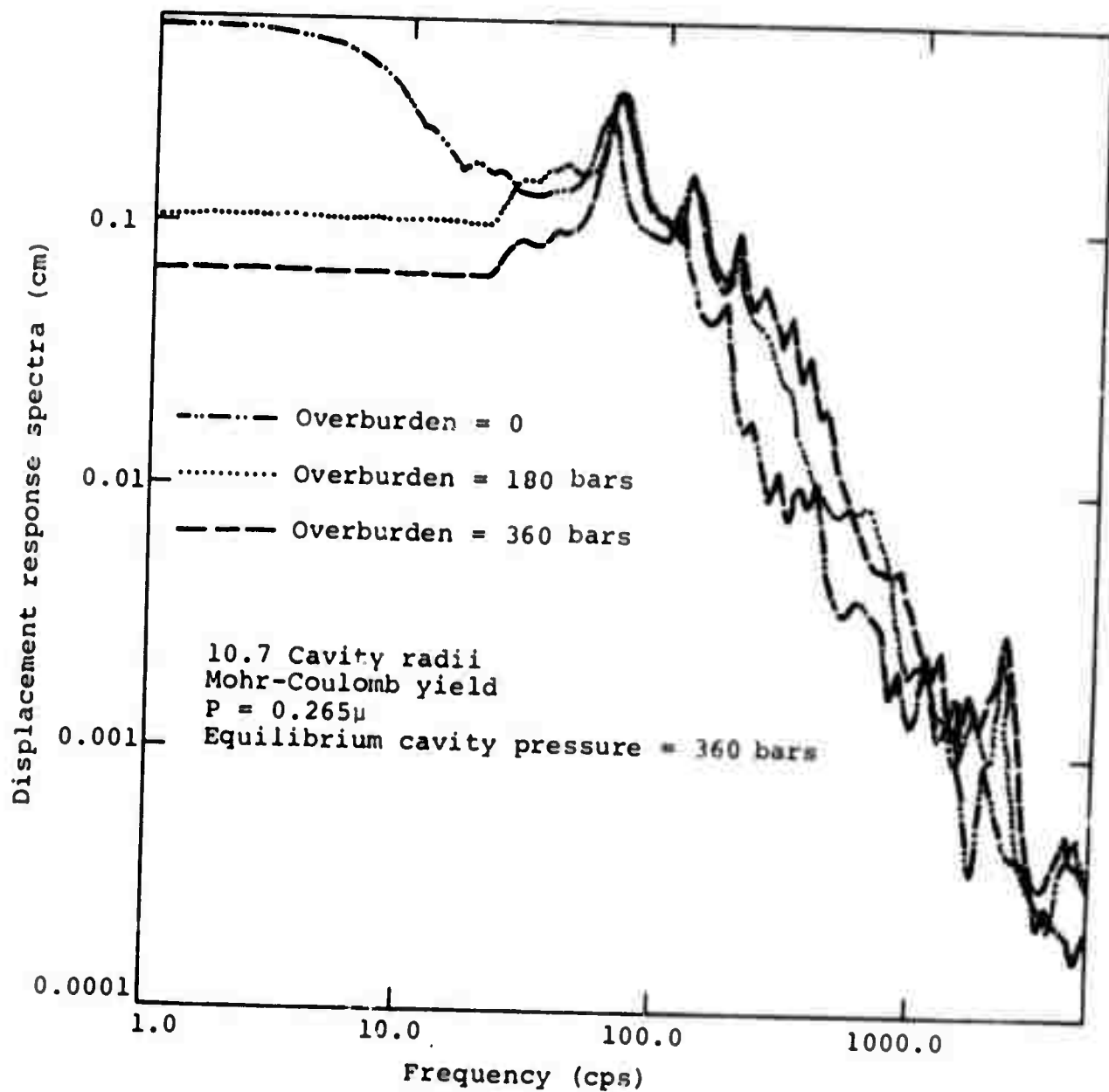


Figure 50 Displacement response spectra showing the effect of overburden.

The effects of varying overburden with a von Mises yield model are not as striking (Figure 51) since with or without overburden there was not extensive yielding in either of the two cases calculated.

The comparison of the von Mises and Mohr-Coulomb yielding with overburden (Figure 51) is interesting. All things being equal, it would be expected that the amplitude of the low frequency spectrum would be higher with the Mohr-Coulomb model, since more yielding occurs. From Figure 51, the opposite appears to be true. The reason is that in the Mohr-Coulomb calculation the overburden was constant 180 bars, starting from the cavity wall and extending outward. In the von Mises calculation the equilibrium overburden distribution was put in, starting at 30 bars at the cavity wall and increasing to 180 bars at very large distances. The stress reached 170 bars at about 2-1/2 cavity radii. Evidently enough yielding occurred close to the cavity to cause the peak displacement to be higher than in the Mohr-Coulomb calculation. This demonstrates that including the equilibrium stress distribution around the cavity does have a detectable effect and should be included for accurate calculation of decoupling behavior.

Figure 52 portrays the response spectra showing the effects of compaction. With compaction there is a dramatic shift of energy from high to low frequency modes and the shock reverberation frequency maxima are obscured or completely missing. If overburden were included in the compaction calculations, the maximum displacements ($\omega = 0$) observed would be lower, however, the spectra would still not show the reverberation frequency maxima and there would still be a substantial shift of energy from higher frequency to lower frequency modes.

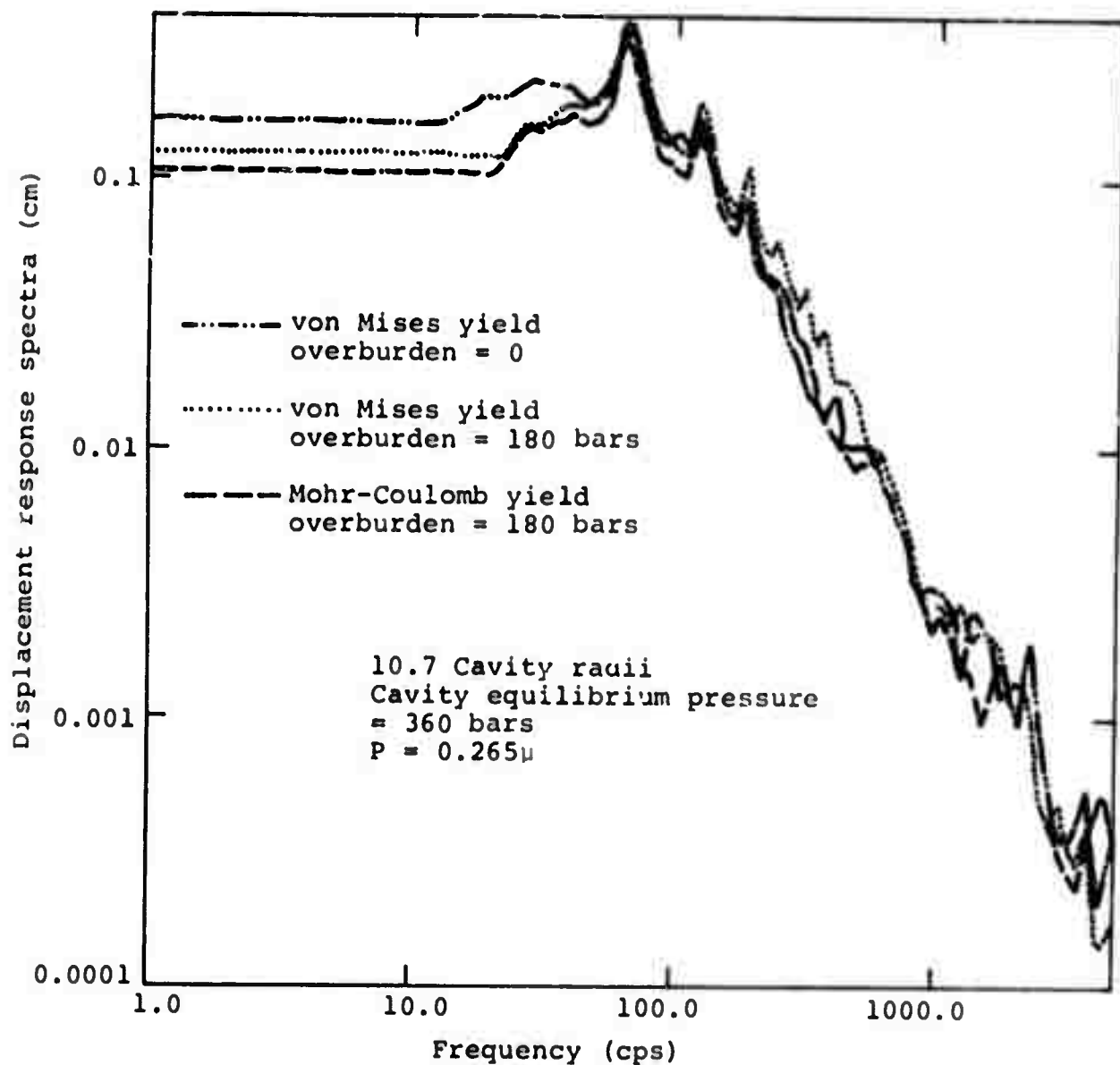


Figure 51 Displacement response spectra showing the effects of overburden and yield model.

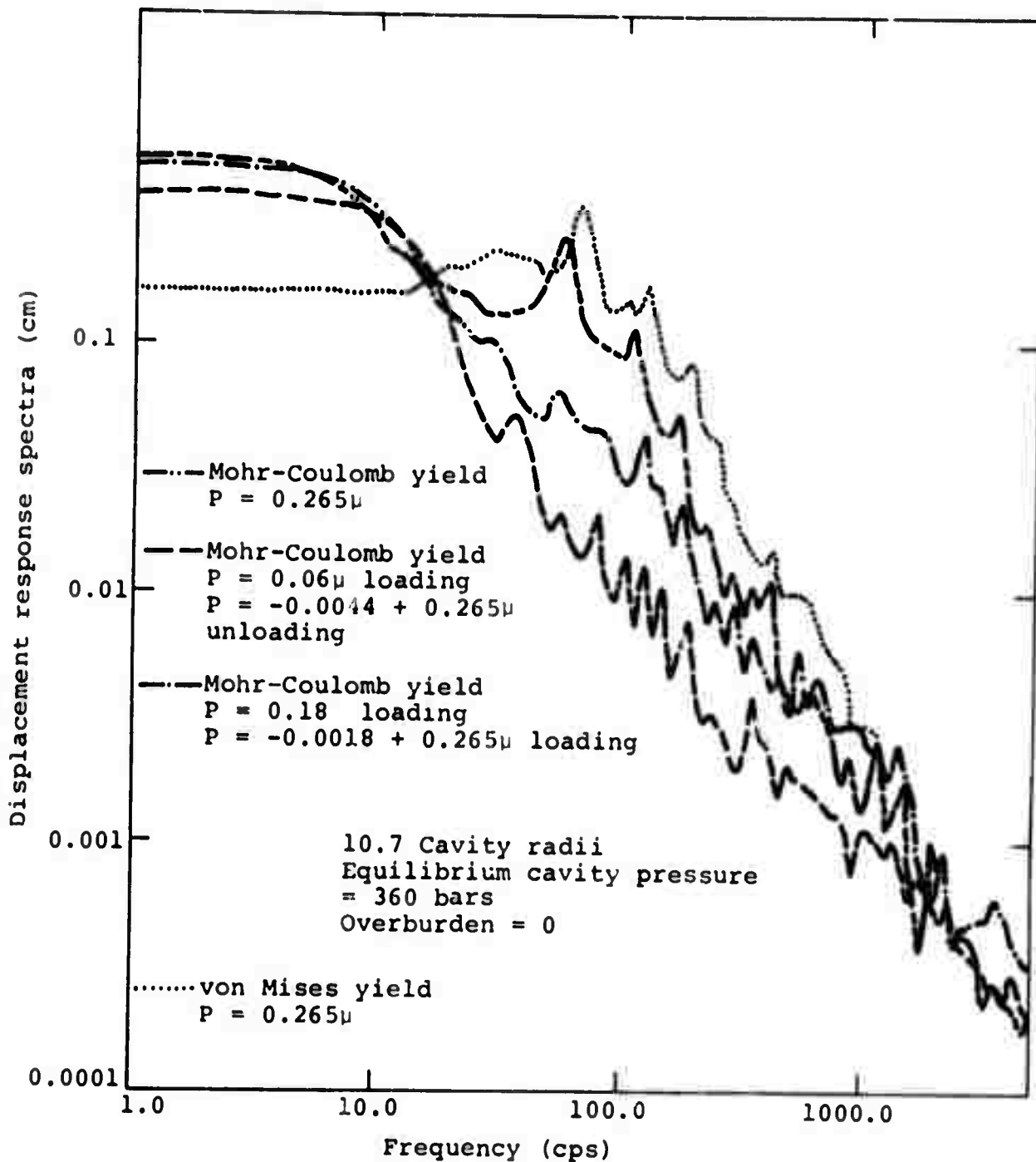


Figure 52 Displacement response spectra showing the effects of compaction and yield model.

Figure 53 shows the effect of increasing cavity equilibrium pressure on the displacement response spectra with and without overburden. With the higher cavity equilibrium pressures, more yielding occurs and there is less decoupling as expected.

A summary of maximum displacements for most of the calculations is shown in Figure 54 as a function of radius. The reduced decoupling effectiveness of yielding and/or compactible media is evident in this plot. Compaction and lack of overburden with Mohr-Coulomb yielding results in strongly coupled cavity response, and the high frequency nuclear source is seen to be the best decoupled case.

The response spectra for various zoning and Courant stability condition safety factors are shown in Figure 55. Some losses are associated with coarser zoning but the effects are minor. Coarser zoning than used in the present calculations would not seriously affect the results of the calculations and would save computer time, especially for extended runs.

For the case of Mohr-Coulomb yield, overburden and linear equation of state, the response and Fourier spectra are compared in Figure 56. As expected the Fourier spectrum is equal to or less than the response spectrum. The spectra coincide at the shock reverberation frequency and its higher modes and nearly coincide at the natural cavity resonant frequency. The maximum displacement (which from Figure 47 results from the first pulse) is larger than the Fourier amplitude (which is the maximum displacement after the entire signal).

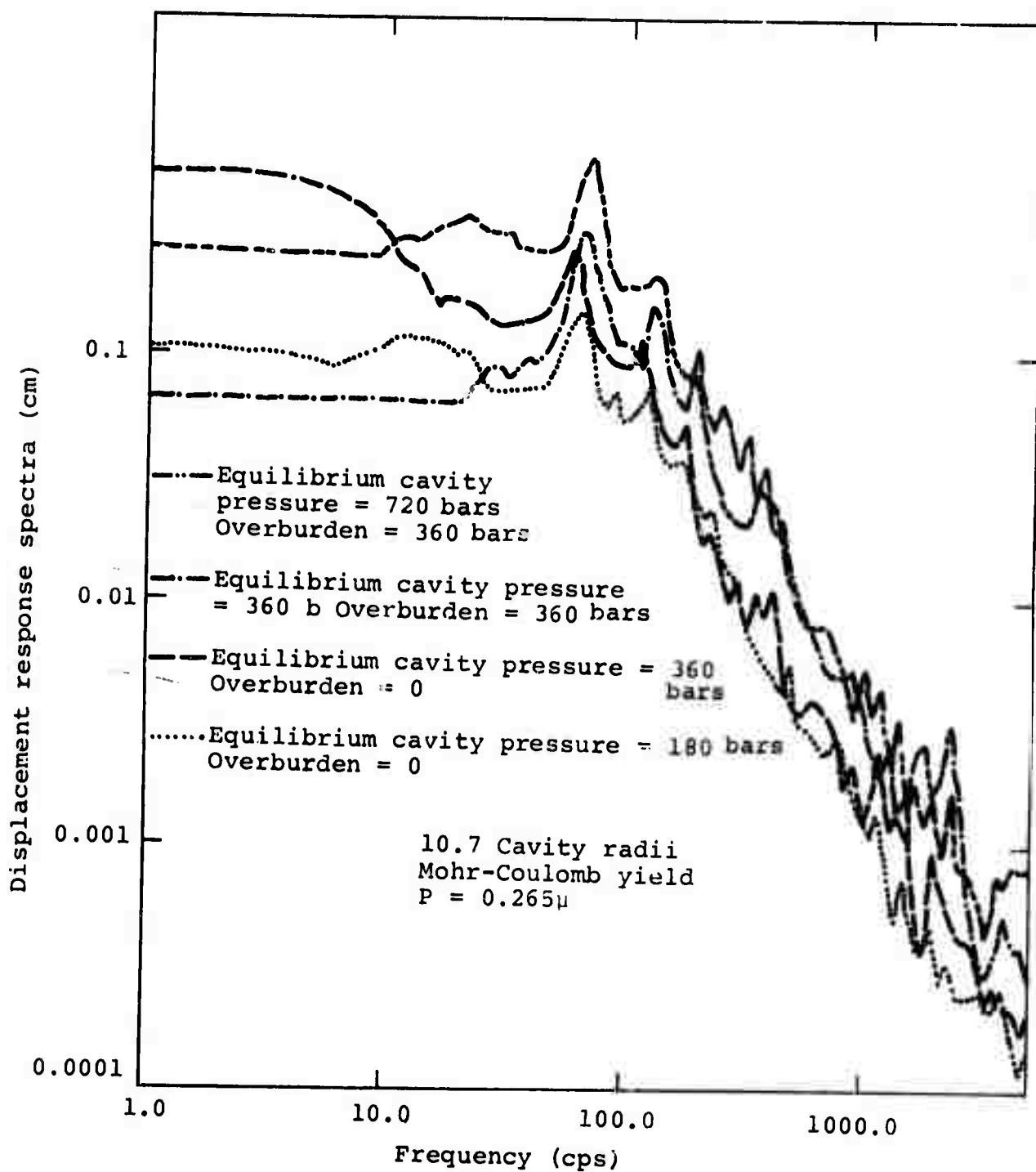


Figure 53 Displacement response spectra showing the effects of equilibrium cavity pressure and overburden.

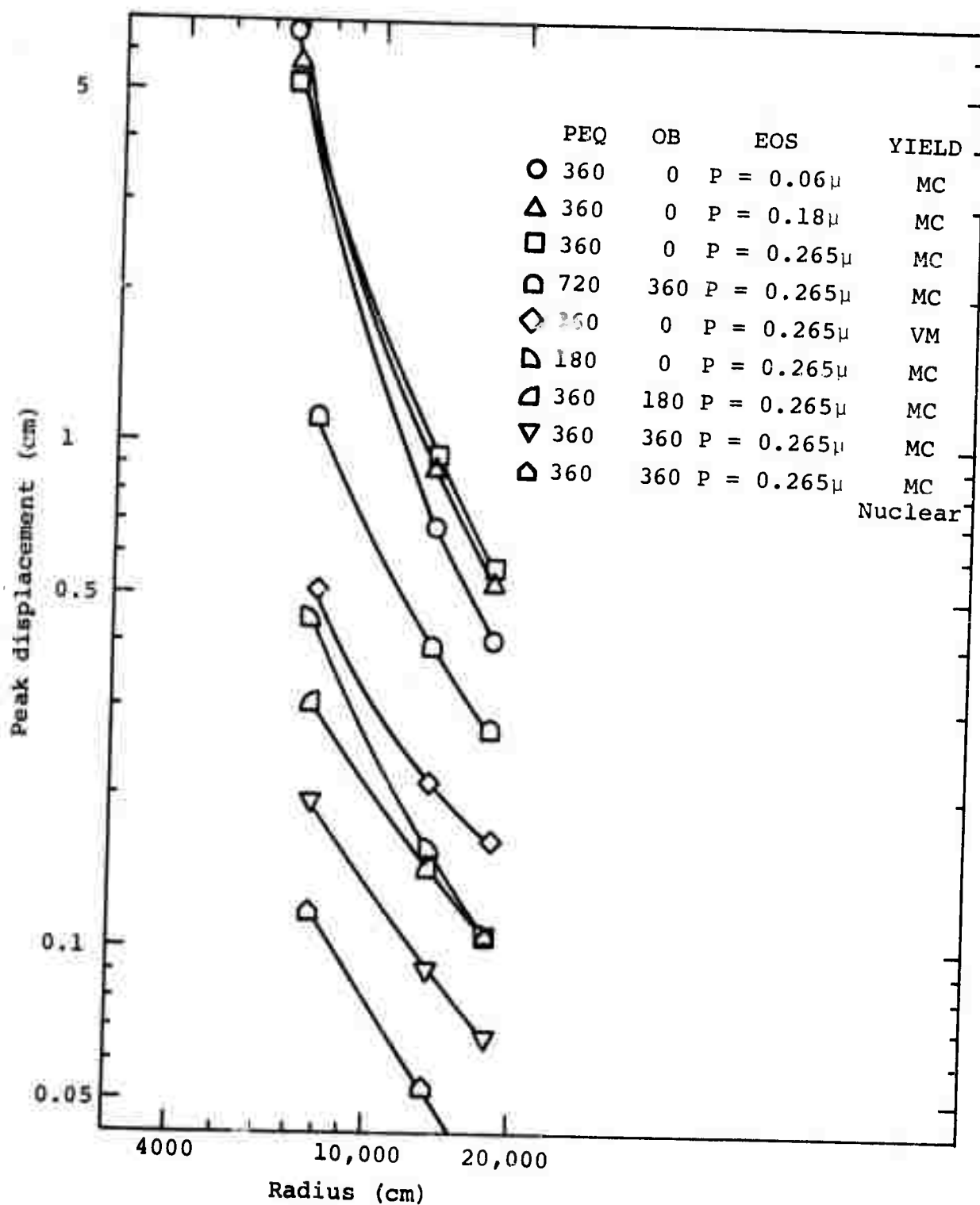
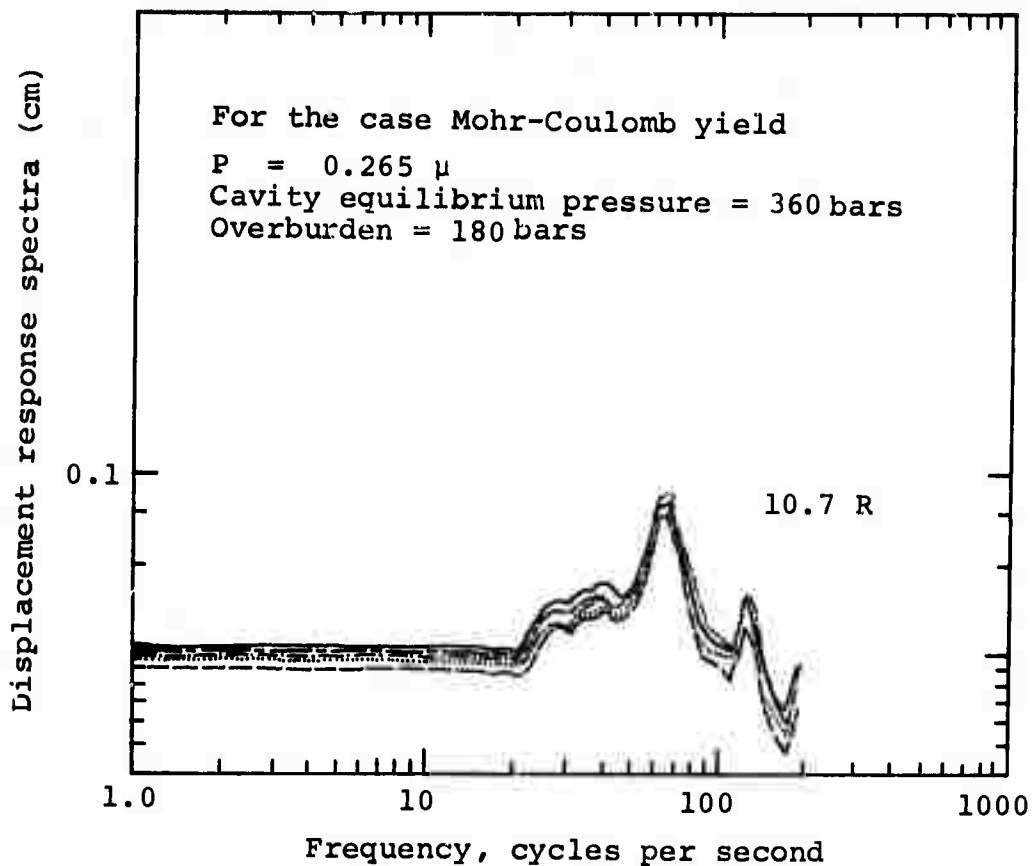


Figure 54 Peak displacement ($\omega = 0$) as a function of radius for selected runs.



Run	Zoning	Courant stability safety factor	Dspec w=0 at 4R	Dspec w=0 at 8R	Dspec w=0 at 10.7R
—	80 cm zones after four rezones	0.95	0.320	0.145	0.106
----	80 cm zones constant	0.95	0.300	0.138	0.098
----	80 cm zones constant	0.67	0.302	0.138	0.102
----	160 cm zones constant	0.95	0.283	0.125	0.090
.....	160 cm zones constant	0.67	0.285	0.130	0.096

Figure 55 Displacement response spectra showing the effect of zoning and the courant stability condition safety factor.

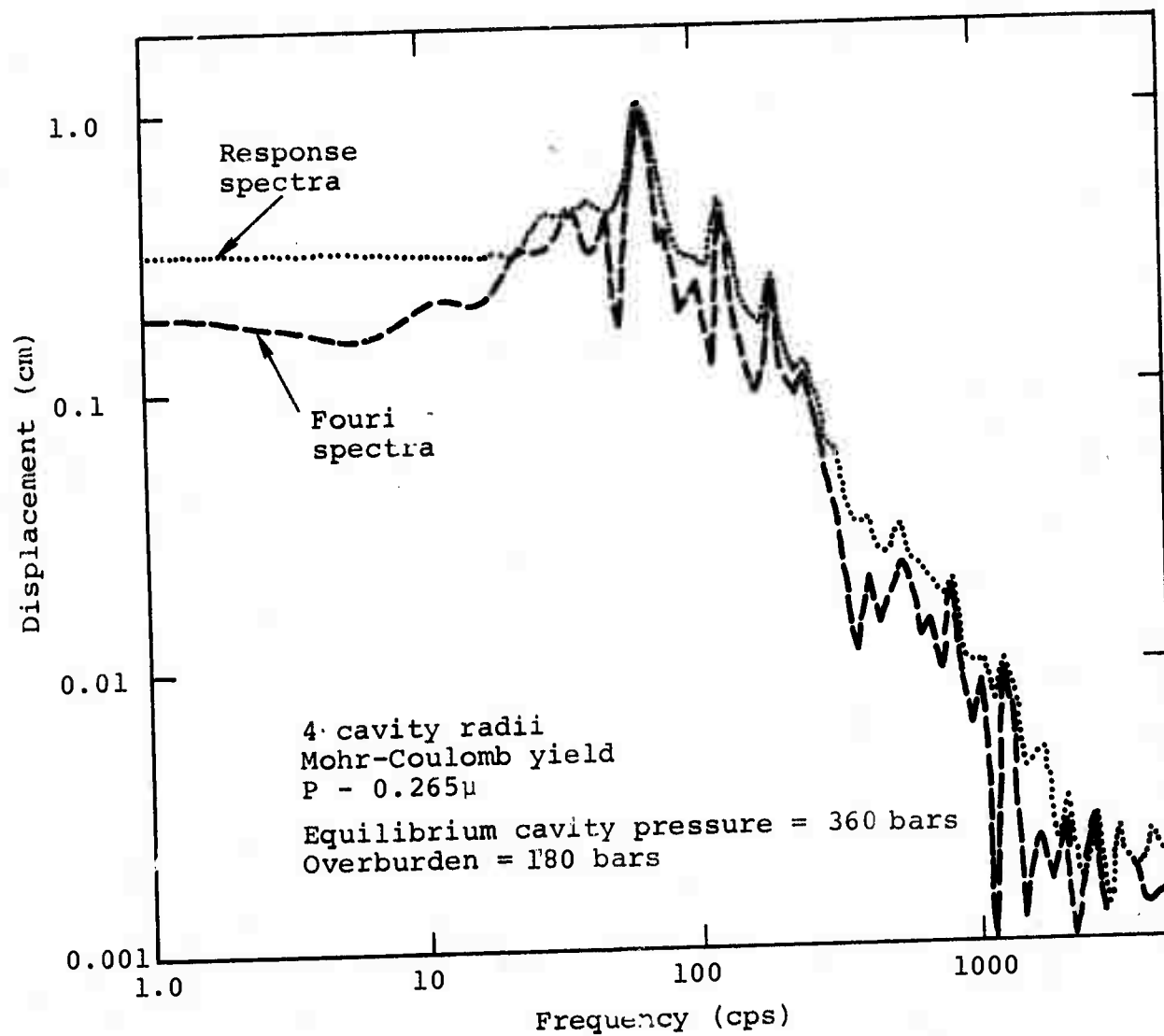


Figure 56 Comparison of response and Fourier spectra for linear media with yielding and gas source.

In the case of a compactible media (Figure 57), the response and Fourier spectra virtually coincide since the displacements were still increasing (Figure 43) when the calculation was terminated.

For an explosion source (the first pressure pulse is the largest), the degree to which the response and Fourier spectra coincide is a measure of the compaction and yielding or other non-linear behavior that occurs in the media.

4.4 PARTIAL RESULTS OF THE 2-D CALCULATION

The zoning of the 2-D Lagrange grid is shown in Figure 58. The cavity is a pillbox with a diameter five times its height and the interior of the cavity is represented by an Eulerian grid. The initial configuration of the fireball is shown in Figure 58. The fireball is approximately a 984 cm diameter sphere of $\gamma = 1.3$ gas at 1.21 gram/cm³ and 15.6 kbars and is surrounded by air at atmospheric conditions.

As the fireball expands it first strikes the cavity directly above it and spreads rapidly to fill the entire cavity. The gas dynamics are very complicated but because of the coarse zoning of the Eulerian grid, most of the finer detail was lost. Velocity histories in the surrounding salt along the X and Y axes (Figures 60 and 61) show that at a given distance from the origin the stress wave arrives first along the Y axis (the fireball expands at a higher velocity than stress waves move in the media) and that the initial wave is stronger along the Y axis.

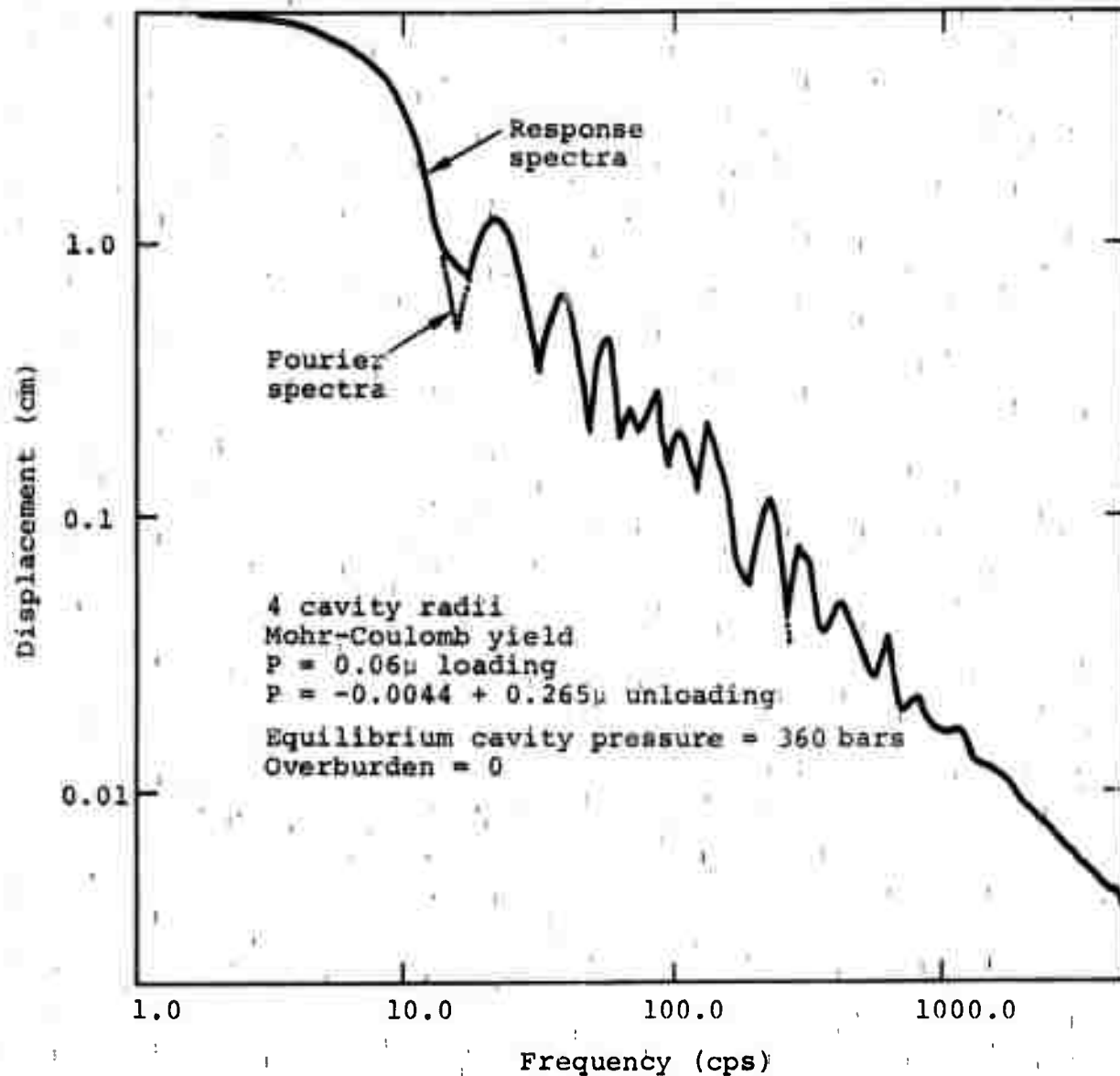


Figure 57 Comparison of response and Fourier spectra for compactible media with yielding and gas source.

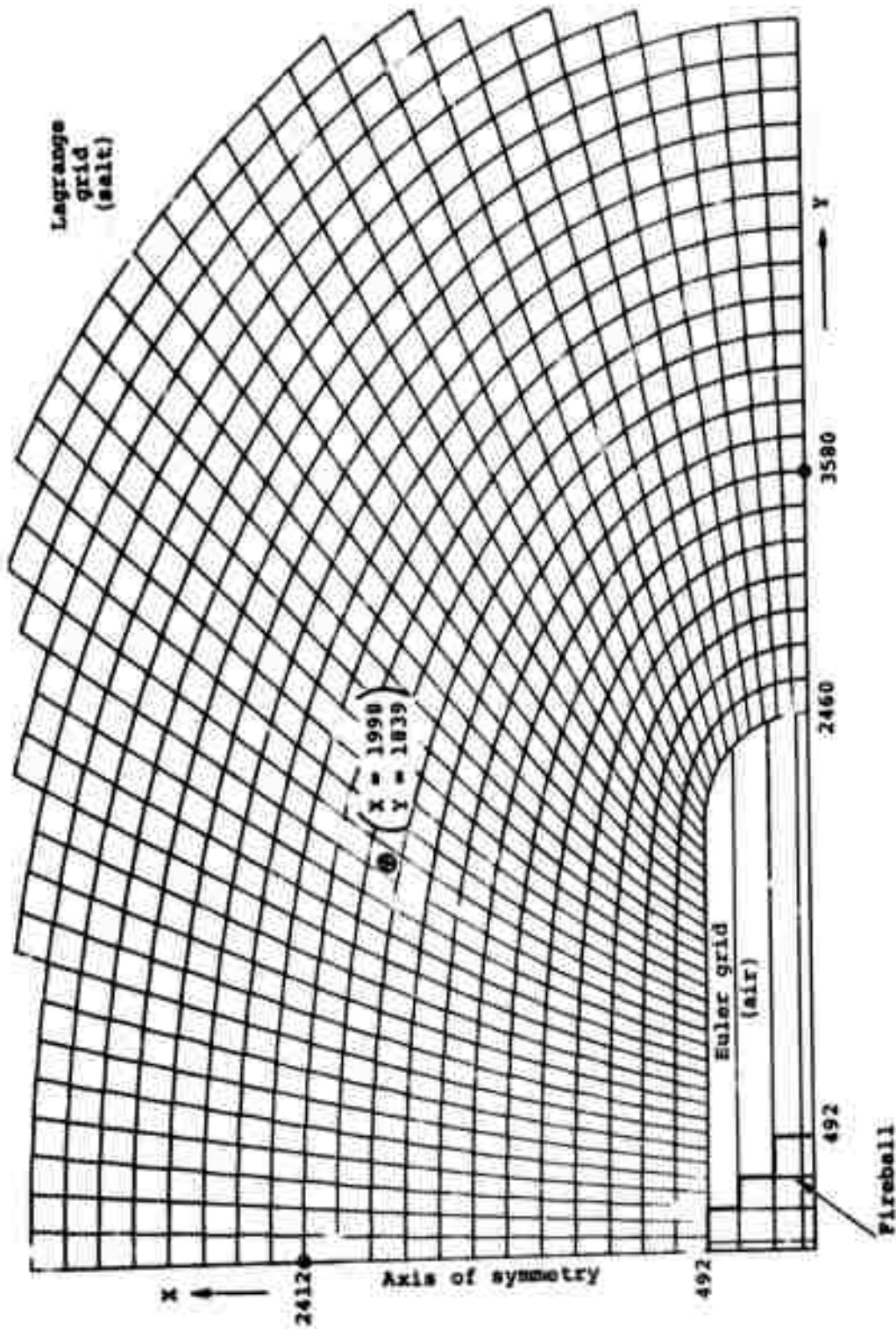


Figure 58 Lagrange grid at $t = 7500 \mu\text{sec}$. Also shown are locations of stress and velocity histories and initial fireball configuration.

The velocity vector plot at $t = 0.0075$ sec (Figure 59) indicates that the pillbox geometry results in substantial shear wave energy although it is too early to tell if it is seismologically important. This type of plot is especially useful in visualizing the waves as they radiate into the salt and shows the shear waves quite clearly.

The X, Y and shear stress histories at 45° from the axis of symmetry are shown in Figures 62, 63 and 64 and the peak X stress is seen to be about $1/3$ larger than the peak Y stress.

The calculation was terminated just before the LEEK grid was to be added. It was intended to run the calculation to $t = 0.05$ and compare the stress and velocity histories with those of the one-dimensional calculations.

4.5 SUMMARY

The calculations presented in this report demonstrate a technique whereby finite difference codes may be used to study decoupling phenomena. Hydrodynamic and elastic-plastic grids are used to calculate the details of the explosion source and the complex response of the media in the vicinity of the cavity. A purely elastic code, LEEK, is coupled to the elastic-plastic Lagrange grid to permit stress waves to propagate far out into the media. It is also feasible to carry out near teleseismic calculations (~ 3 -5 km from the source) by using two-dimensional codes coupled to a LEEK grid. Such calculations would include the effect of layering, free surfaces and material compaction and would have zonal resolution on the order of 5-meters. When run on advanced computer systems such as the CDC 7600, the cost

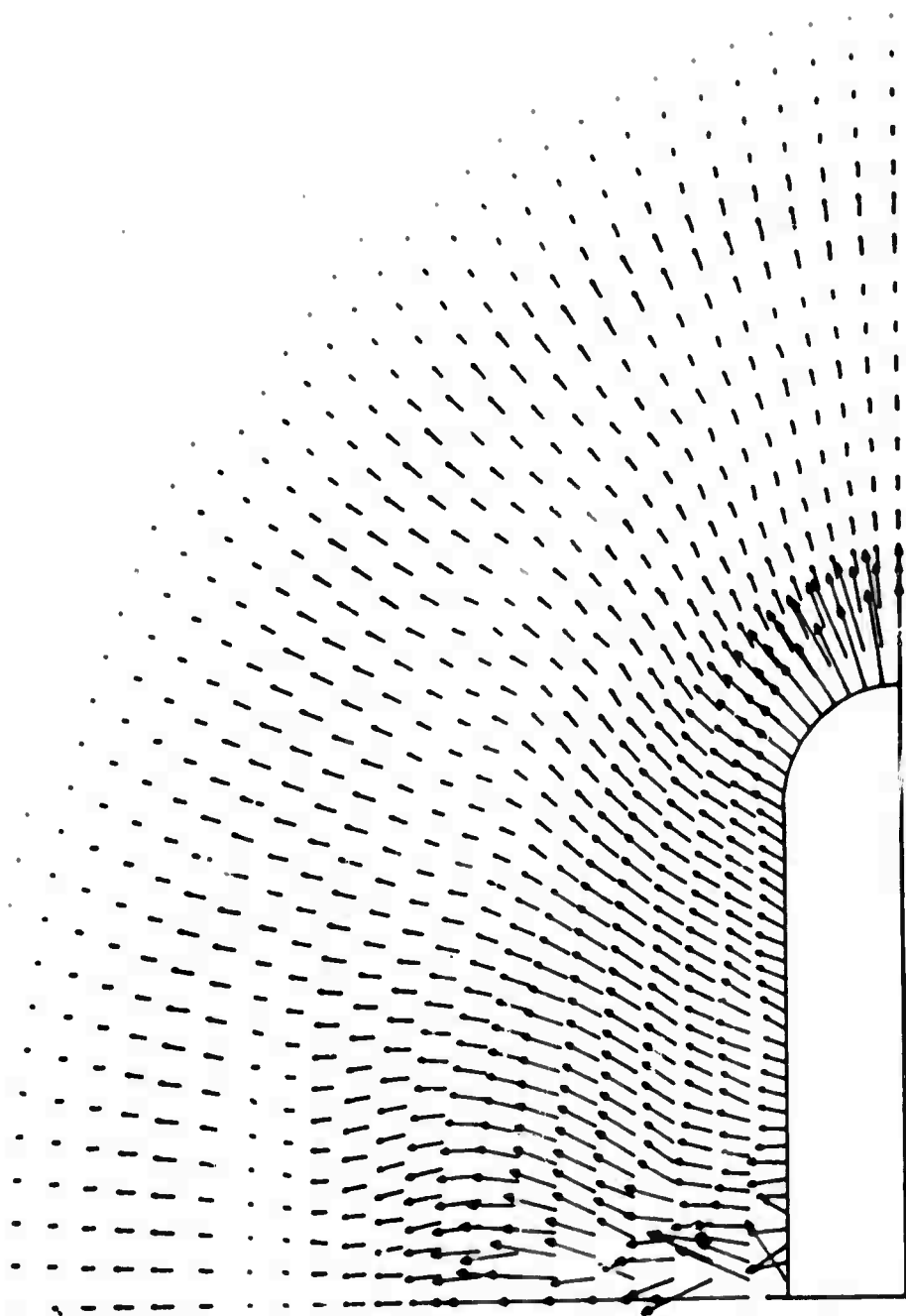


Figure 59 Velocity vector plot of the Lagrange grid at $t = 7500 \mu\text{sec.}$

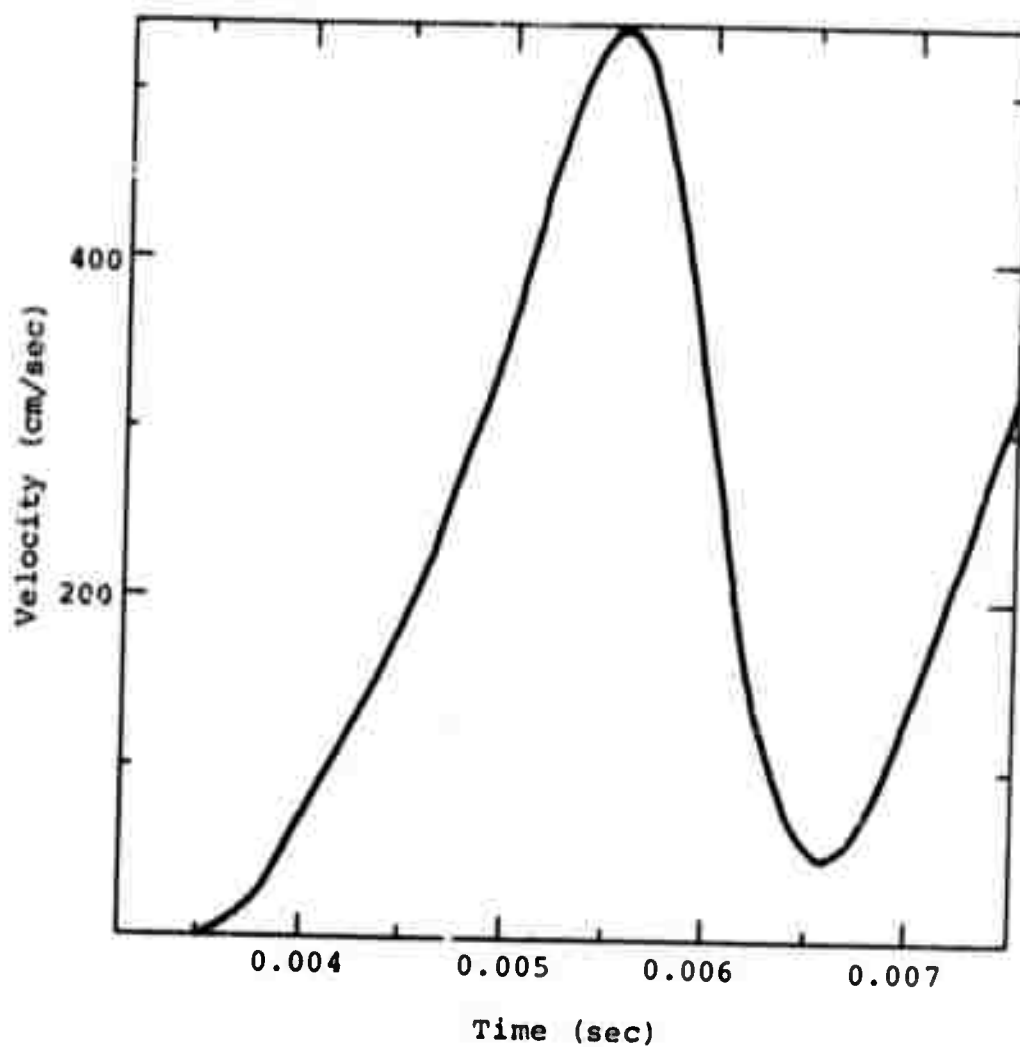


Figure 60 Velocity (\dot{X}) history parallel to the axis of symmetry of the cavity at $X = 2412$ cm and $Y = 0$ cm.

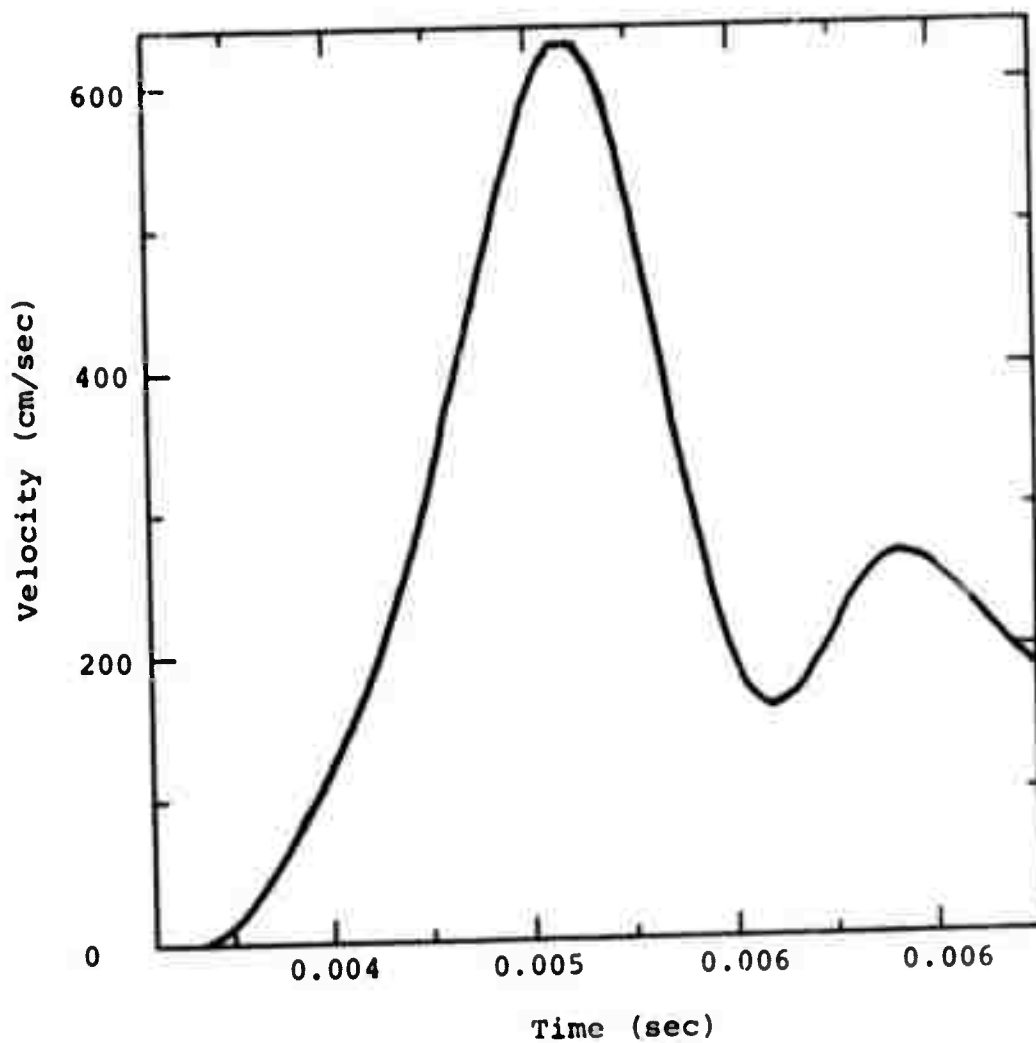


Figure 61 Velocity (\dot{Y}) history perpendicular to the axis of symmetry of the cavity at $X = 0$ cm and $Y = 3580$ cm.

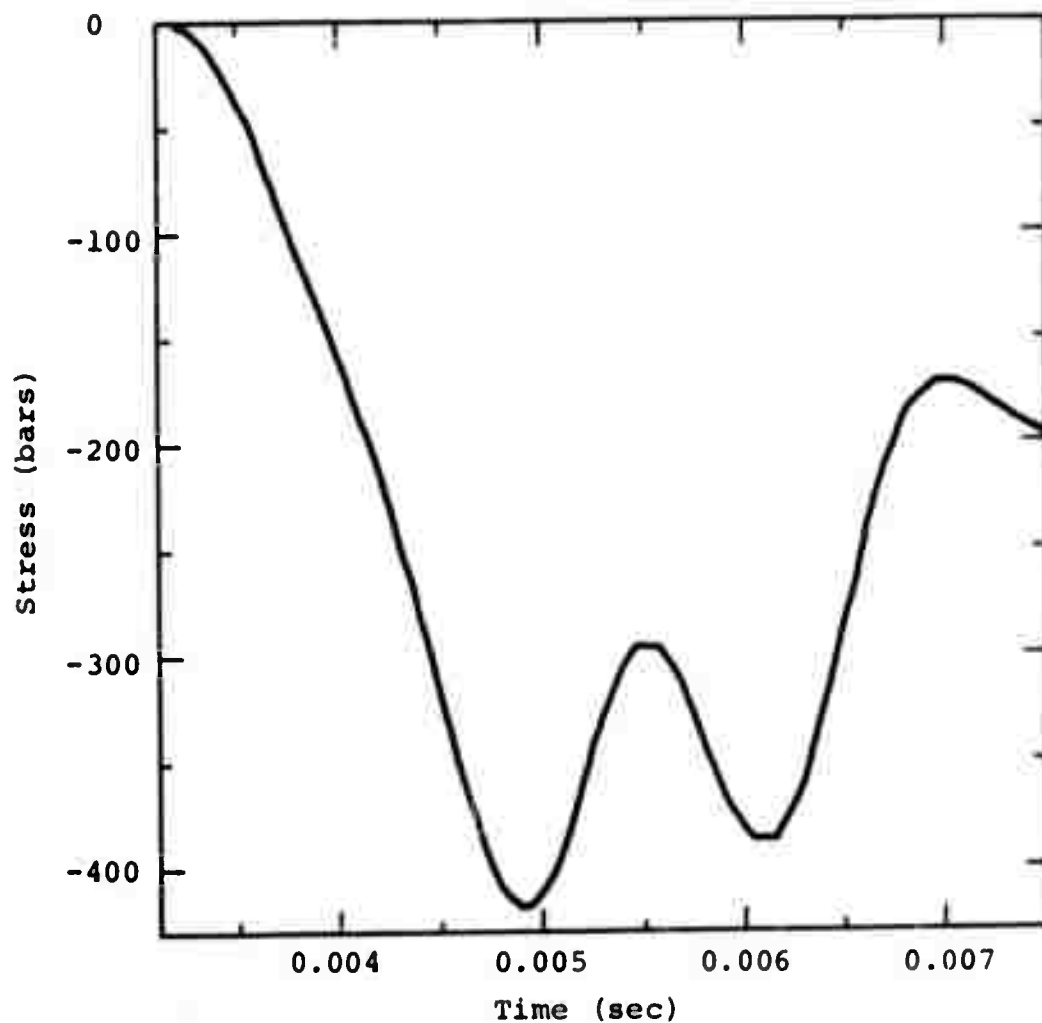


Figure 62 Stress (τ_{xx}) history parallel to the axis of symmetry of the cavity at $X = 1998$ cm and $Y = 1839$ cm.

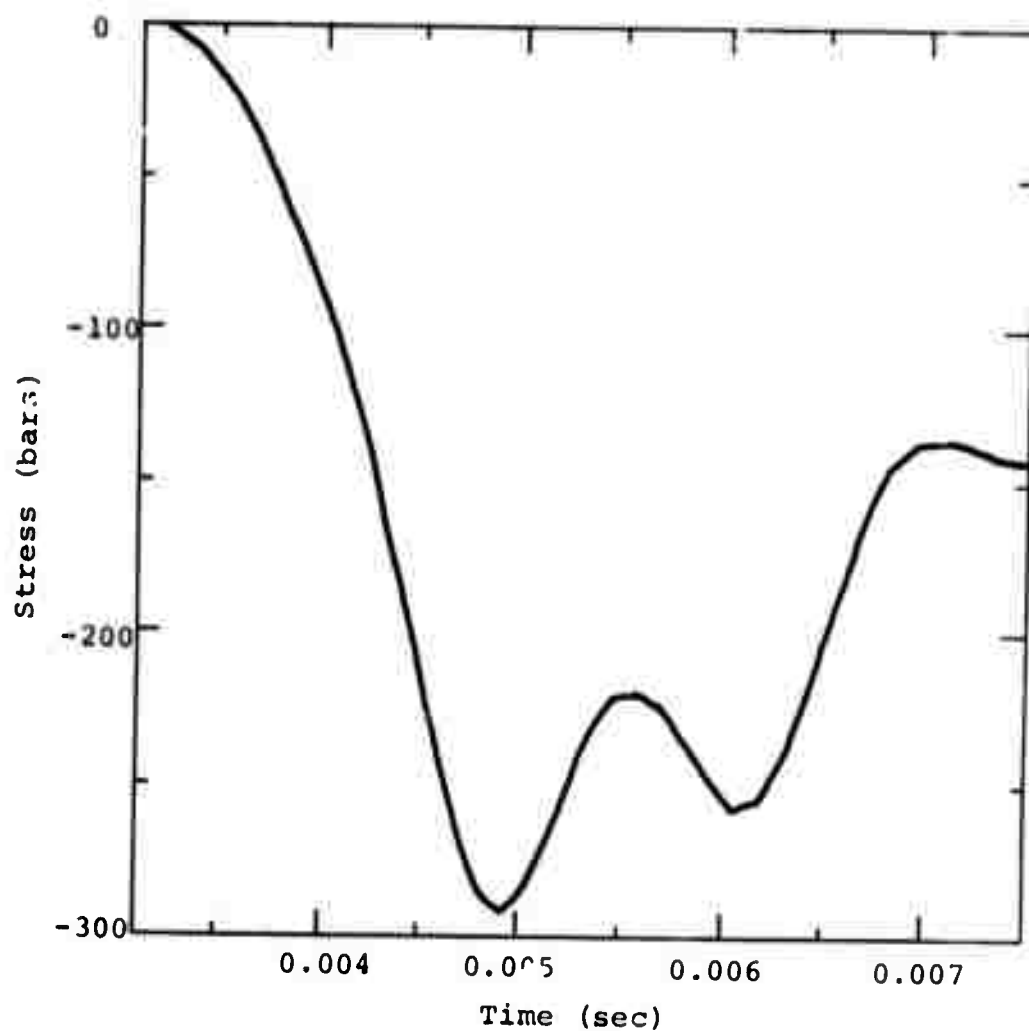


Figure 63 Stress (τ_{yy}) history perpendicular to the axis of symmetry of the cavity at $X = 1998$ cm and $Y = 1839$ cm.

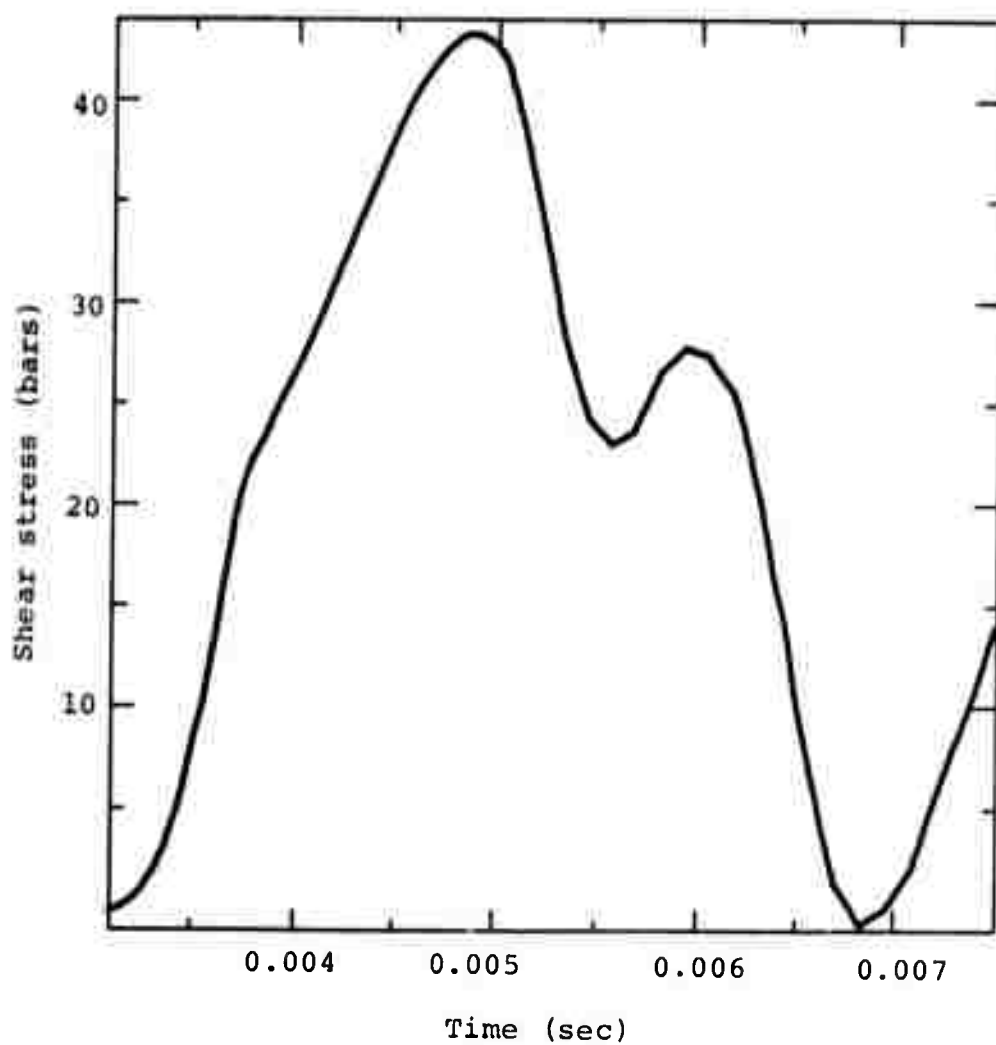


Figure 64 Shear stress (τ_{xy}) history at $X = 1998$ cm and $Y = 1839$ cm.

of these calculations would be reasonable. The results of this type of calculation would provide insights for interpreting near teleseismic data gathered on many recent underground tests.

In the course of the one-dimensional calculations reported herein, the effects of yield model, overburden, compaction, source amplitude and frequency were studied. An evaluation of the salt response in the time and frequency domain revealed that several of the above parameters could have a controlling effect on the seismic signal generated by the explosion.

For a given cavity and explosion source, the plastic yielding in the vicinity of the cavity (in the first few cavity radii), shifts energy from the high frequency modes (tens and hundreds of cps) to the low frequency modes which are able to be transmitted to teleseismic distances. Although there is a net loss of energy associated with yielding, there is an amplification of energy in the low frequency modes.

The effect of increasing overburden is to suppress yielding and thereby suppress the transfer of energy to the lower frequency modes. Equilibrium overburden stress distribution around the cavity is important in the calculation, since there is significant yielding in the immediate area of the cavity which has an important role in determining the low frequency content of the energy spectrum.

One of the most dramatic effects observed in the calculations was that of material compaction. Compaction causes a large amount of net energy loss, but there is still a net amplification in the low frequency content of the energy spectrum. No calculations of a highly coupled source in a yielding, compactible media

with overburden was made. However, it is not clear that in such a case that the energy losses in the yielding, compacting media would be large enough to overcome the amount of energy shifted from the higher frequency modes to the lower (and seismically important) modes. The object of decoupling is to minimize the low frequency amplitude of the signal and the calculational technique used in the present study can be a valuable tool in studying presently held views of large cavity decoupling or in optimizing source, cavity and media properties to minimize the low frequency signal amplitudes in future underground tests.

Most of the calculations reported herein were made for a detonating gas source relevant to the MIRACLE PLAY Series. One high frequency source representative of a nuclear explosion in an evacuated cavity is presented. The effect of increased source frequency, all other things being equal, was a marked reduction in coupling to the surrounding media. The source frequency of the nuclear calculation was well above the natural cavity resonance frequency and there was very little cavity yielding. Consequently, most of the radiated energy resides in the high frequency portion of the spectrum (several hundred cps) and will decay quickly.

A two-dimensional calculation to investigate the effect of cavity geometry on the observed signal, was partially completed and indicated that substantial shear wave energy is generated although the calculation was not carried out far enough to determine if this was of seismic importance.

SECTION 5

CONCLUSIONS

A capability for conducting small scale experiments with various materials, overburdens and sources has been successfully developed. Used in conjunction with field tests and calculations, this technique can be used to isolate and study parameters affecting decoupling and can lead to increased understanding of presently available data, and possibly reduce the number of underground tests required in the future. The small scale experiments reported herein concentrated on methane-oxygen detonations in spherical cavities in salt. The salt behavior was in general agreement with large cavity decoupling theory. Increased coupling was observed at higher pressures in natural salt but was not observed over the pressure range studied in artificially pressed salt where work-hardening and overburden apparently suppressed extensive yielding.

High quality data was obtained using a strain gauge diagnostic system, however even better data can be obtained with electromagnetic velocity gage systems now available at Physics International. Subjecting the data to a response spectra analysis further clarifies the decoupling effects of yielding and overburden as it provides a measure of the transfer of energy from higher to lower frequency modes. The salt response observed in these tests is also in general agreement with the response predicted by a series of one-dimensional finite difference calculations.

The experimental apparatus now exists to perform similar experiments with different media such as granite or tuff and is suitable for any chemical explosive source. In addition to simulating overburden, the apparatus can be used to investigate non-spherical cavities and evacuated cavities thereby allowing a study of varying source frequency. With an evacuated or helium filled cavity it is possible to provide a source with amplitude and frequency characteristics approaching those of a nuclear source.

A very interesting test would be to compare a given source in a large decoupled cavity in an elastic media with the same source in a highly coupled cavity in a yielding compactible media. A response spectra analysis of the velocity history at 6 cavity radii would permit a direct measurement of the low frequency content of the energy spectrum and would help determine which approach might be better for effective decoupling.

A calculational technique has been successfully developed which has the potential of solving problems in the near teleseismic range (several kilometers). This technique utilizes traditional finite difference codes to calculate the explosion and complex response of the media near the cavity and couples this to the purely elastic LEEK code, which extends the calculation to the near teleseismic regime. This method, which was demonstrated in a series of one-dimensional calculations, is also applicable to existing two-dimensional codes, and when used on advanced computer systems can calculate at a reasonable cost problems of current interest such as the near teleseismic data gathered on the Diamond Mine and Diamond Dust experiments.

In the one-dimensional calculations discussed in this report, it is pointed out that the details of the waves propagating in the overburdened, yielding and compacting media near the cavity are critically important in determining the seismic content of the signal. For example in a highly yielding and compacting media there can be a large energy loss in the media but still a net amplification of energy in the low frequency portion of the spectrum which is of great importance in decoupling.

Both the experimental and calculational capabilities reported herein are now developed to the point where they can be used immediately to study problems of specific interest.

REFERENCES

1. A. L. Latter, R. LeLevier, E. A. Martinelli, and W. McMillan, "A Method of Concealing Underground Nuclear Explosions," Rept. R-348, RAND Corp., Santa Monica, California (1959).
2. D. W. Patterson, "Nuclear Decoupling, Full and Partial," Jour. Geophys. Res., V. 71, n. 14, pp. 3427-3436 (1966).
3. R. F. Herbst, G. C. Werth, and D. L. Springer, 1961, "Use of Large Cavities to Reduce Seismic Waves from Underground Explosions," Jour. Geophys. Res., V. 66, n. 3, pp. 959-978.
4. D. Springer, M. Denny, J. Healy, and W. Mickey, "The Sterling Experiment: Decoupling of Seismic Waves by a Shot-Generated Cavity," Jour. Geophys. Res., V. 73, n. 18, pp. 5995-6011 (1968).
5. D. S. Bahjat and C. Kisslinger, "Coupling of Explosive Energy in Three-Dimensional Models," Geophys., V. 35, n. 2, pp. 220-233 (1970).
6. C. Godfrey, D. Maxwell, F. Finlayson, E. T. Moore, V. Davis, H. Moises, R. Kant, G. Steel, and C. Mutoke, "A Theoretical and Experimental Study of Detonations, in Connection with Decoupling," Physics International Rept. No. PIFR-107, DASA 2505 (1969).
7. A. L. Latter, E. A. Martinelli, J. Mathews, and W. G. McMillan, "The Effect of Plasticity on Decoupling of Underground Explosions," Jour. Geophys. Res., V. 66, n. 9, pp. 2929-2936 (1961).
8. A. L. Latter, R. E. LeLevier, E. A. Martinelli, and W. G. McMillan, "A Method for Concealing Underground Nuclear Explosions," Jour. Geophys. Res., V. 66, n. 3, pp. 943, 946 (1961).
9. G. Werth and P. Randolph, "The Salmon Seismic Experiment," Jour. Geophys. Research, V. 71, n. 14, pp. 3405-3413 (1966).

REFERENCES (Cont.)

10. L. E. Fugelso, N. T. Gottenberger, and W. J. Byrne, "Detonable Gas Explosions in Drill Holes as Seismic Signal Generators," DASA 2366, 1968.
11. J. Handin, R. V. Hager, Jr., M. Friedman, and J. N. Feather, "Experimental Deformation of Sedimentary Rocks under Confining Pressure: Pore Pressure Tests," Bull. Am. Assoc. Petrol. Geol. V. 47, n. 5, p. 717-754, 1963.
12. Robert L. Wiegel, Earthquake Engineering, Chapter 4, Prentice-Hall Inc., Englewood Cliffs, New Jersey, 1970.
13. L. E. Fugelso, N. T. Gottenberger, W. J. Byrne, "Detonable Gas Explosions in Drill Holes as Seismic Generators," DASA 2366, September, 1968.
14. Walker J. Davis, "Technical and Operation Plan MIRACLE PLAY," Test Command Defense Atomic Support Agency, Sandia Base, New Mexico, October, 1968.

APPENDIX A

THE LEEK CODE

In a typical problem of cratering of a solid material, violent hydrodynamic motion and plastic flow is confined to a relatively small region around the explosion or impact. The kinetic energy density of outward propagating stress waves quickly decays because of the internal friction of the medium and the geometric divergence of the waves. Beyond a characteristic "elastic radius," R_e , the stress waves, which may still be of kilobar magnitudes, become ordinary acoustic waves and may be treated by the theory of linear elasticity. The elastic radius in a typical cratering problem might be a few crater radii, for example. In a two-dimensional calculation of cratering, a large fraction of the computational time in each time step is devoted to performing thermodynamic and plastic flow computations. It is obvious that a considerable saving in computer time and storage space can be realized if the thermodynamic iterations and plastic flow computations are not performed for those finite-difference zones that lie beyond the elastic radius of the energy source of the problem.

Rather than modify our two-dimensional Lagrange continuum mechanics code to skip over these unnecessary calculations for elastic zones, Physics International has developed an efficient and flexible elastic finite-difference code which couples to our Lagrange code. This code is called LEEK (Linear Elastic Escape Kondition); it computes elastic zones about 40 times faster than our Lagrange code.

Because of its computational efficiency, LEEK greatly broadens the scope of problems which our continuum mechanics codes can economically and accurately compute. As an example, in the time it takes for a crater to form, stress waves may travel on the order of 10 crater radii from the point of impact. To compute the full crater formation, one must have finite-difference zones out to about six crater radii, so that wave reflections from the outer boundary will not return to the region of the crater during the time of its formation (Figure A-1). Such reflections would be unrealistic and, due to their geometric convergence, could ruin the computation. It would be prohibitively expensive to use the Lagrange code to compute all of the zones of this problem. But with the LEEK code to compute all of the elastic zones, it becomes economically feasible to compute the problem.

LEEK is a very sophisticated elastic code and may be used by itself as a powerful tool for studying seismic wave propagation. In developing it we have made novel use of a combination of finite-difference techniques commonly used by seismologists and by physicists. The code is flexible enough to be able to compute problems in which the elastic constants are arbitrary functions of position and in which zones are arbitrary quadrilaterals. In addition, either stresses or displacements may be specified as the boundary conditions, and the code may couple with our Lagrange code along part of its boundary. A brief description follows of how LEEK works.

Consider a linear elastic solid in cylindrical coordinates about the z -axis. Displacements in the r and z directions are denoted by u and w , and because of the (assumed) cylindrical symmetry, are only functions of r and z .

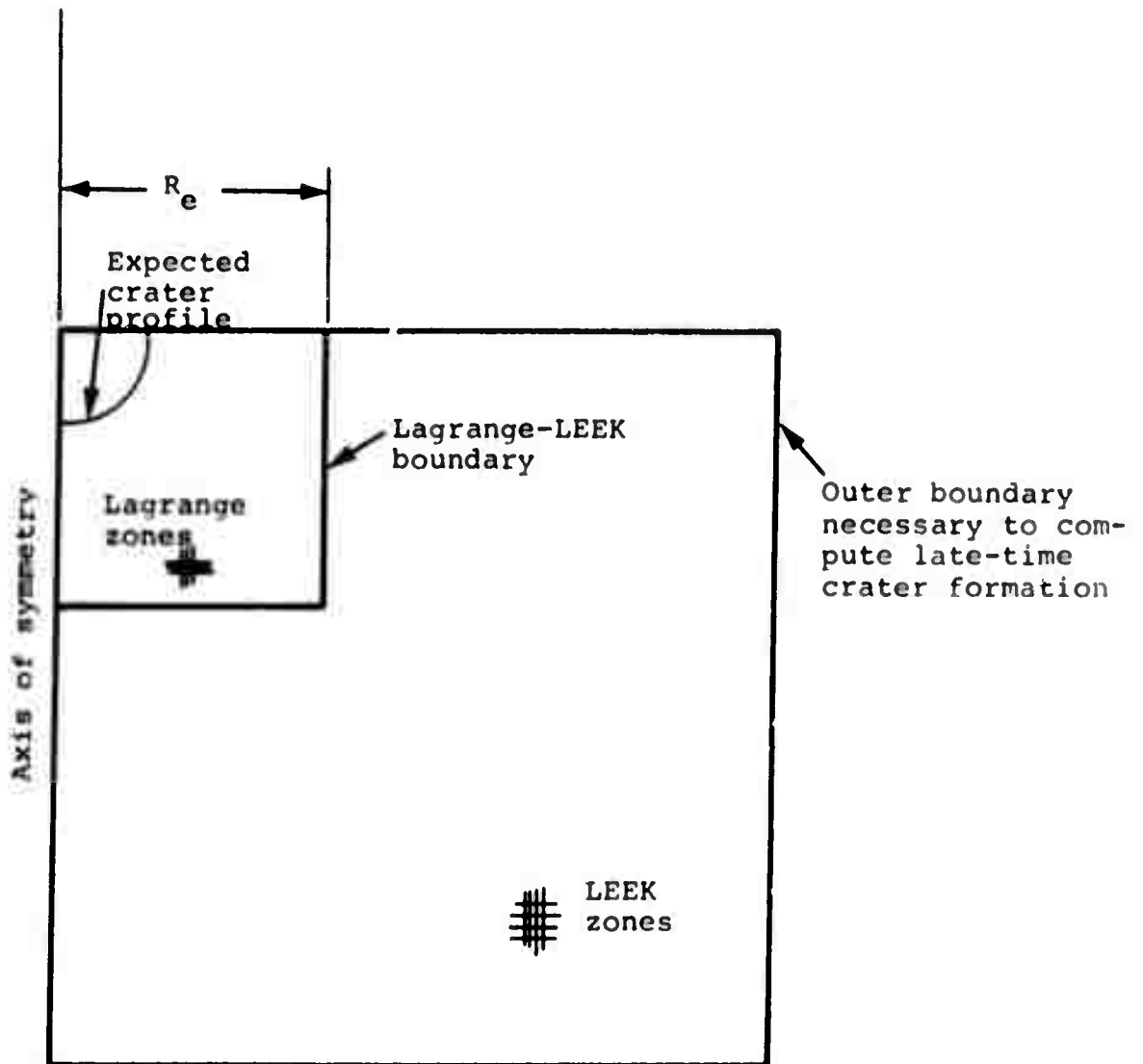


Figure A-1. Zoning for crater formation problem.

The equations of motion are

$$\rho \ddot{u} = \frac{\partial}{\partial z} \Sigma_{rz} + \frac{\partial}{\partial r} \Sigma_{rr} + \frac{\Sigma_{rr} - \Sigma_{\theta\theta}}{r} \quad (1)$$

$$\rho \ddot{w} = \frac{\partial}{\partial z} \Sigma_{zz} + \frac{\partial}{\partial r} \Sigma_{rz} + \frac{\Sigma_{rz}}{r} . \quad (2)$$

Hooke's law relates stresses to strains:

$$\Sigma_{rr} = \lambda \Delta + 2\mu \epsilon_r \quad (3)$$

$$\Sigma_{zz} = \lambda \Delta + 2\mu \epsilon_z \quad (4)$$

$$\Sigma_{\theta\theta} = \lambda \Delta + 2\mu \epsilon_\theta \quad (5)$$

$$\Sigma_{rz} = 2\mu \epsilon_{rz} \quad (6)$$

where the strains are given by

$$\epsilon_r = \frac{\partial u}{\partial r} \quad (7)$$

$$\epsilon_z = \frac{\partial w}{\partial z} \quad (8)$$

$$\epsilon_{rz} = \frac{1}{2} \left(\frac{\partial u}{\partial z} + \frac{\partial w}{\partial r} \right) \quad (9)$$

$$\epsilon_{\theta} = \frac{u}{r} \quad (10)$$

$$\Delta = \epsilon_r + \epsilon_z + \epsilon_{\theta} \quad (11)$$

A finite-difference mesh of quadrilateral zones is defined which covers the body. Wherever possible, the mesh is made of uniform rectangular zones. At each mesh point velocities and displacements are defined. Rectangular "blocks" of mesh points with uniform rectangular zones that all have the same density and elastic constants, λ and μ , are singled out for a fast finite-difference acceleration computation.

Two different methods are used to compute the accelerations of points. Method II is used for the homogeneous blocks and is described below. Method I is used for all other points, including boundary points and interface points between blocks, except for boundary points which lie along the Lagrange-LEEK interface. The accelerations of these points are computed by the Lagrange code from forces supplied to it by the LEEK code.

In Method I, direct finite-difference approximations to Equations (1) through (11) are used to compute accelerations. The finite-difference equations are similar to those described by Wilkins (Reference A-1). In this scheme, strains are first computed in all existing zones surrounding the point to be accelerated. Then stresses are computed from Hooke's law.

Stress gradients are then computed at the grid point and the point is accelerated according to the equations of motion. This method of computing accelerations is quite general, since it allows λ , μ , and ρ to vary from zone to zone, and the zones need not be rectangular.

A much faster scheme, Method II, is used to compute the accelerations of mesh points which lie within homogeneous rectangular blocks. In this case, we may combine Equations (1) through (11) to get the two simpler equations:

$$\ddot{u} = C_L^2 \left[u_{rr} + w_{zr} + \frac{u_r}{r} + \frac{u}{r^2} \right] + C_T^2 \left[u_{zz} - w_{zr} \right] \quad (12)$$

$$\ddot{w} = C_L^2 \left[w_{zz} + u_{rz} + \frac{u_z}{r} \right] + C_T^2 \left[w_{rr} + \frac{w_r}{r} - u_{rz} - \frac{u_z}{r} \right] \quad (13)$$

where

$$C_L^2 = (\lambda + 2\mu)/\rho$$

$$C_T^2 = \mu/\rho.$$

The subscripts denote partial derivatives. Simple finite-difference approximations to these equations can be made (Reference A-2).

Once the accelerations have been computed by either Method I or Method II, they can be integrated over a time step to give new velocities and new displacements. Although we have discussed only cylindrical symmetry, the equations for plane strain are easily derived by letting $r \rightarrow \infty$ in the cylindrical symmetry equations.

REFERENCES

- A-1. Mark L. Wilkins, "Calculation of Elastic-Plastic Flow," UCRL-7322, Rev. 1, January 24, 1969, Lawrence Radiation Laboratory, Livermore, California.
- A-2. Z. Alterman and F. Karal, "Propagation of Elastic Waves in Layered Media by Finite Difference Methods," Bulletin of the Seismological Society of America, 58, 357-398, 1968.

APPENDIX B

DESCRIPTION OF THE VARIOUS MATERIAL MODELS

1. YIELD MODELS

Two types of yield models were used in the calculations--the Mohr-Coulomb and the von Mises models. For both of these models, the material is assumed to behave elastically up to some state of stress at which yielding occurs. The von Mises condition for flow is that the second invariant* of the stress deviator tensor is a certain value (Reference B-1). For an elastic-plastic material, the same result obtains when volumetric compression is considered to be purely elastic, and when there is a limit to the amount of distortional energy that can be stored elastically. The Mohr-Coulomb condition is a generalization of frictional sliding. The shear stress required for simple slip depends on the cohesion, c , and linearly upon the normal pressure. The proper generalization for this condition under any state of stress is that at slip

$$Y = c + bP$$

*The stress deviator tensor is the stress tensor with the average stress (pressure) subtracted from the diagonal elements. The second invariant of a tensor of rank two, t_{ij} , is given by

$$J_2 = -(t_{11}t_{22} + t_{22}t_{33} + t_{33}t_{11}) + t_{12}^2 + t_{23}^2 + t_{31}^2$$

In simple tension, the yield stress $Y = \sqrt{3J_2}$ (Reference B-2).

where P is the hydrostatic component of stress (Reference B-3). A von Mises limit is conventionally placed on the yield stress to represent ductile flow in the crystal structure as an upper limit to the shear strength. For both of these yield criteria, the pressure (and volumetric strain) was not affected by plastic flow.

2. EQUATION OF STATE

Two models of hydrostatic behavior were used in the calculations. The formula

$$P = B\mu$$

represent purely elastic behavior. The variable μ is a compression variable useful for large as well as small strains. It is computed as

$$\mu = \frac{\rho}{\rho_0} - 1,$$

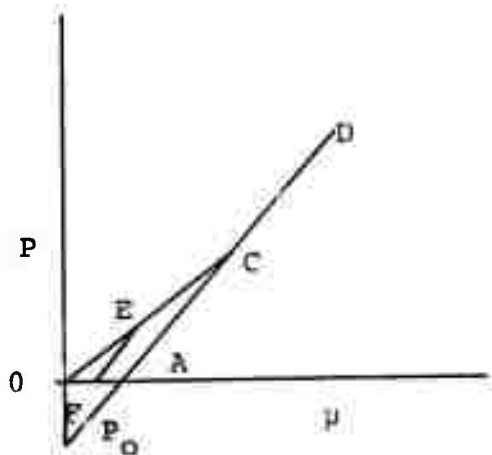
the scaled ratio of current to reference densities. The coefficient B is the (elastic) bulk modulus.

The other equation of state form used has different formulas for loading and unloading

$$P = B_L \mu \quad \text{Loading}$$

$$P = P_0 + B_U \mu \quad \text{Unloading}$$

The loading modulus, B_L , is smaller than the unloading modulus, B_U . The figure below illustrates the calculational procedure.



Loading to high pressure (D on the figure) follows the path OECD, where OEC has the slope B_L , and CD has the slope B_U . Unloading from any pressure higher than C to zero pressure is on the line DCA, with slope B_U . Any further loading and unloading is on the line P_0ACD . If the loading is to a lower pressure than C, the crushing is not complete. One such loading path is OE. Unloading takes place along EF with slope B_U . Reloading to higher pressure from F takes place along FECD.

REFERENCES

- B-1. M. Reiner, Lectures on Theoretical Rheology, North-Holland Publishing Company--Amsterdam, Third Edition (1960).
- B-2. J. C. Jaeger, Elasticity, Fracture and Flow, Methuen & Co. (John Wiley & Sons, Inc., New York) Second Edition (1964).
- B-3. D. C. Drucker and W. Prager, "Soil Mechanics and Plastic Analysis or Limit Design," Quart. Applied Math., Vol. X, No. 2 (1952).